Ultraviolet and visible photonic devices with subwavelength grating

サブ波長回折格子による
紫外・可視フォトニックデバイスの開発に関する研究

March　2017

2017 年 3 月

Yuusuke Takashima

高島 祐介

Abstract

Short wavelength light, such as ultraviolet (UV) and visible (VIS) extremely benefit for human science. However, the range of applications is restricted by physical property of material, such as photon absorption. In this study, the challenge to overcome the restriction by using the eigenmode in subwavelength grating (SWG) was done, and the VIS ~ UV photonic device with SWG was successfully developed.

The wavenumber dispersion relation and the electromagnetic filed distribution in SWG was investigated to reveal the propagation mechanism of the mode in SWG. The dispersion relation indicated that the wavenumber of the eigenmode is broadened by the deceasing life time due to the photon absorption in the SWG. The filed distribution suggested the highly selectivity of polarization can be obtained, while high transmittance was still maintained, regardless of the large photon absorption. This approach provides new insight into the SWG design for the shorter wavelength light control and open the feasibility of development photonic device without the significantly decreasing of the light intensity.

Based on the theoretical analysis, a highly polarized emission from a GaN-based UV-LED with maintaining the emission intensity was experimentally demonstrated using SWG. The polarization ratio reached to 17 at the wavelength of 370 nm, and the EL intensity is 1.2 times larger than that without the structure.

The influence of the deviation of grating shape caused in fabrication on the emission characteristics was theoretically and experimentally estimated. The results shows the phase state of the eigenmode strongly depended on the grating shape, and this design considering the eigenmode state was important to fully demonstrate the

performance of the actual device.

Based on the controlling the phase of the mode, a highly sensitive refractive index detection devices with normal incident geometry was experimentally developed by using SWG, The SWG was designed to be highly sensitive the surrounding refraction index by using the wavenumber dispersion relation, and the dependence of the transmittance on the surrounding refractive index was calculated. The calculation results suggest that the highly sensitive detection for its value with wide range utilizing the SWG. The designed SWG experimentally and successfully demonstrated 4^{th}-order decimal change of surrounding refractive index with normal incident geometry.

Acknowledgement

The author deeply appreciated my supervisor Professor Yoshiki Naoi of Tokushima University for the kindly, continuous guidance, encouragement over this study. He would like to acknowledge Professor Shiro Sakai for the comments and technical advises on the experiment in this study. He would like to represent gratitude to Professor Shuichi Hashimoto and Professor Masanobu Haraguchi for the kindly comment and correction, advice for this thesis.

I would like to thank appreciated Professor Takuro Tomita for helpful discussion and technical advices on measurement results presented in this thesis

This work would not have been done without the funding from Japan Society for the Promotion of Science and Nichia scholarship certificate.

Finally, he deeply thank his parent for continuous care, support over three years.

Contents

Chapter 1: Introduction to a subwavelength grating (SWG)

1.1 Background

A light wave is closely rerated with the humankind science. The applications using the light are classified by the wavelength of the light. For example, a millimeter-wave was employed as radar [1]. A terahertz wave was used as non-destructive inspection in medical and semiconductor industry [2,3]. In communication field, an infrared (IR) wave was used to realize ultra-fast signaling speed [4,5]. The visible (VIS) light, which is a familiar to humankind, has enormous applications ranging from illumination to 3D-display [6,7]. Ultraviolet (UV) light is useful for the sterilization [8]. X-ray is employed as non-destructive inspection of human body and materials [9].

A techniques treating the light wave (transmittance, reflectance, polarization states, and orientation) are essential for the applications mentioned above. In particularly, the polarization control without the significant decreasing of the light intensity in UV and VIS wavelength region can open the door of unique integration applications in chemical, biology, energy saving medical science, and engineering [10-13]. However, the photon absorption becomes larger with the decreasing the wavelength, and this prevents the development of the integration devices in shorter wavelength region, such as UV and VIS wavelength region.

The interference effect is widely and typically used to control light wave. The interference effect is occurred by two or more fraction of the light. In the non-periodic optical structure, the interference effect is canceled between the light fractions. Hence, the optical periodic structure have been typically employed in order to promote

interference between these fractions.

The optical periodic structure, which is called “grating”, have been investigated with a long history as very important element to promote the interference effect. The light technology using grating have been reported since 1889 [14]. Grating is classified by the ratio of the period to the incident wavelength. Most of the grating have the period larger than the incident wavelength. This grating type is called “diffraction grating”. In diffraction grating, the emerging light is diffracted due to the periodicity, and the light is divided into the various order diffracted light by the interference effect of the light from each grating slits. Each diffraction angles except for 0th-order diffraction (the transmitted and reflected light) depend on the wavelength of light. As a result, the wavelength can be separated by diffraction grating, and this grating type have been widely used for various applications in holography, lasers, and spectroscopy [15,16].

On the other hand, a subwavelength grating (SWG) with a period shorter than the incident wavelength is special category of diffraction grating and attracts many interests owing to the unique optical characteristics. Especially, the electromagnetic response of the nano-order size SWG is quite different from that of a diffraction grating as following reason [17,18]. When the light was radiated to the SWG, the electric charge was moved by the electrical filed of the incident light. The electromagnetic response of the SWG is determined by the movement of the electric charge. In addition, the charge is generated on the surface of the grating material owing to the polarization in meterial. The induced polarization depends on the geometry of SWG due to the retardation effect of the electromagnetic interaction between the material and the incident light. As a result, the total electromagnetic filed distribution, which strongly reflects the material geometry, is formed. Then, the grating size approaching to the mean free path of the charged

particles (about nano-meter-order) limits the movement of the particles. Thus, the electromagnetic response of nano-scale SWG is quite different from that of other-scale (for example micrometer-, centimeter-scale) SWG, and light-matter interaction in nano-scale SWG can be artificially modified by the structure geometry. This suggest nano-order SWG structure can open the door of the development of integration devices without the decreasing in the shorter wavelength region, regardless of the physical property of the material.

Many light controlling techniques using SWG have been reported since the beginning of 1980's [19,20]. Owing to the retarding effect of the electromagnetic interaction, the SWG structure is divided into two regions. One is the "deep-subwavelength" regions. In deep-subwavelength region, the grating period is much shorter than the incident wavelength. When the light emerges into the deep-SWG, the deep-SWG feel the uniform electromagnetic field of the incident light wave over the structure. Thus, the electromagnetic response of deep SWG is represented as quasi static electromagnetic interaction, and the mean of refractive index of the deep-SWG can be controlled by the filling factor of the structure. The controlling technique of the mean refractive index using deep SWG have been used as wire-grid polarizer [21-24], wave plate [25,26], and anti-reflect coating [27,28].

Another region of SWG is "near-subwavelength" region [29]. In the near subwavelength region, the period is in order of the wavelength of incident light. Hence, the near SWG no longer feel the uniform electromagnetic field of the light. In 2004, Connie J. Chang-Hasnain *et al*. discovered unexpected extraordinary features in the high contrast near SWG, in which the high refractive grating material is fully surrounded by low refractive index [30]. The period is between the wavelengths in grating material and

that in the surrounding media, such as air. The schematic diagram of the high contrast SWG structure is

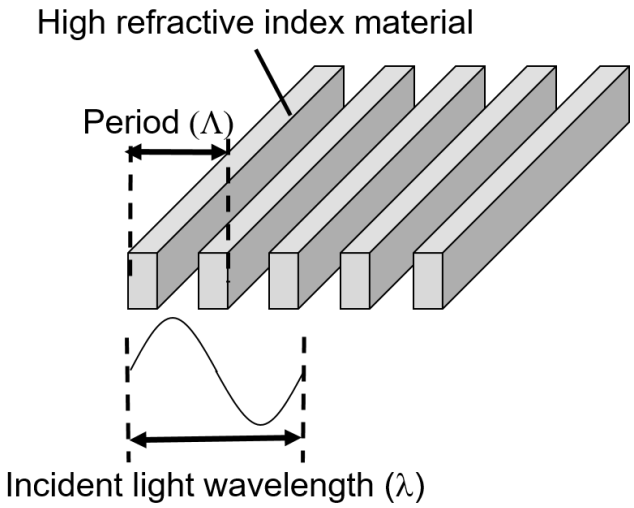

Figure 1.1 Schematic diagram of a high contrast SWG

shown in Fig.1.1. The high refractive index materials were arranged with the period Λ and the grating was fully surrounded by low refractive index material. In this SWG, the extraordinary features can be obtained, such as an ultrabroadband high reflectivity (>99%), very high-quality-factor, highly polarization selectivity with low loss, and the focusing planer lens as shown in Fig.1.2 [29-32]. The high contrast SWG was applied as a high reflectivity mirror in vertical cavity surface-emitting lasers (VCSELs), and VCSELs with the incorporated the SWG have been demonstrated at IR wavelength region [33-

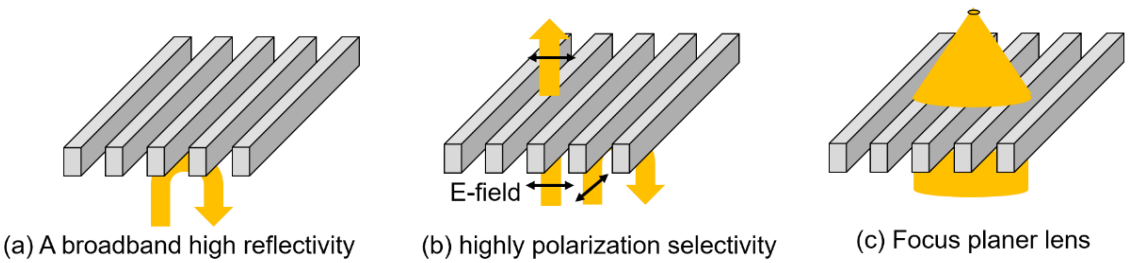

Figure 1.2 Extraordinary properties of high contrast SWG structure

38]. Since the demonstration of VCSELs with high contrast SWG, many researchers lively study the high contrast SWG structure.

Several groups investigated and reported the electromagnetic response of the SWG [38-43]. In the SWG, the eigenmode, which differ from that in free space, is the solution of Maxwell's equations owing to the periodic refractive index distribution. The eigenmode wave interacts with the incident wave at a certain condition, this interaction dominates the optical response of the SWG. In most researches, the response was estimated and analyzed by effective medium theory (EMT) model, in which the eigenmode within the SWG was assumed the plane wave, to explore the electromagnetic response of the SWG [39-42]. In other words, the SWG structure is approximated as a uniform layer with an effective refractive index. The EMT-predicted optical characteristics of the SWG are only accurate when the grating period Λ is significantly shorter than λ, for example wire-grid polarizer [41,43]. As Λ approaches the value of λ, the actual electromagnetic response in the near-SWG deviates from that predicted by the EMT. The advantages of the eigenmode, namely artificially control the light-material, cannot be utilized in this EMT condition, because the optical characteristics of the SWG is determined by the physical property of material.

The light control utilizing the eigenmode within the SWG have been reported in 1995 [44,45]. S. Y. Chou and W. Deng reported that Si-SWG on silica substrate shows very strong polarization selectivity, and they pointed out the origin of the selectivity is the higher order eigenmodes due to the strong modulation of the refractive index distribution of Si-SWG. However, the detail of the eigenmode was not reported and discussed. I. C. Botten *et al.* explained the optical property of dielectric lamellar grating by a rigorous model theory [46]. They described the diffraction anomalies not only in low refractive

index grating but also high refractive index grating. The unexpected extraordinary features of high refractive index contrast SWG cannot explained.

Recently, V. Karagodsky *et al*. have theoretically investigated and estimated the optical characteristics of high-contrast SWG in the infrared (IR) wavelength region considering up to the 2nd-order mode [47-49]. They provided the straightforward insight of the design algorism without heavy mathematical formalisms. However, this analysis was performed for an SWG with a real refractive index only, because the imaginary part of the material refractive index, namely photon absorption can be negligible in the IR wavelength region. In shorter wavelength region (e.g. VIS and UV region), the imaginary part of the SWG in this region is larger than that in the IR region. For example, Si, which typically employed as high contrast SWG, has the large imaginary part of the refractive index [50,51]. Thus, the effect of the imaginary part on the eigenmode state in the SWG is not negligible in the shorter wavelength region, and the optical characteristics in that region deviate from those in the IR region.

In this study, the challenge to control the material-light interaction by eigenmode in SWG was done to overcome the limitation of design by the physical property of the material in the shorter wavelength region. The purpose of this study was to elucidate the light propagation mechanism in SWG to provide a new design concept of the SWG at UV ~ VIS wavelength. In addition, a UV and VIS photonic integration devices were demonstrated appling SWG structure.

1.2 Application of ultraviolet (UV) and visible (VIS) photonic devices with the SWG

In this section, the application, which is applied the SWG, were described. The background of these applications and the merit by applying SWG were presented.

1.2.1 Light-emitting diode (LED) with SWG

GaN-based light emitting-diodes (LEDs) has been developed and used in the various filed, such as illumination system, back light in liquid crystal display system, and sterilizing [52-56]. A further improvement of the characteristics open the new application of the LEDs. One of the feature is polarization characteristics of the LEDs. Highly polarized light-emitting diodes have unique integration applications. For example, irradiation by a linearly polarized UV wave can induce optical anisotropy in photoreactive polymers [11,13]. This prosperity is particularly suitable for achieving the alignment of liquid crystals in the absence of the rubbing and patternable processes. For highly polarized VIS-LEDs, the polarization characteristics is very useful for energy saving in display backlight system of liquid crystal display [57]. These integration applications require the use of highly polarized emission without a significant light decreasing in emission intensity.

A polarizing plate, composed of an iodine-doped polymer, is generally used to control the polarization of the LED emission as shown in Fig 1.3(a). The transmittance through such a filter is very low, especially in the UV region (~ 30% at 360 nm), because most photons are absorbed in the polymer. The area scale of the polarizing plate, which is more than a square centimeter order, is very large for integrated devices. Several

groups have recently fabricated polarized nitride-based LEDs using semi- or non-polar crystals [57-59], photonic crystals [60], and wire grids [42,61,62]. The semi- or non-polar Gan based LED is shown in Fig 1.3 (b). You *et al.* found that the electroluminescence (EL) spectra in the visible region from *m*-plane InGaN/GaN LEDs have a polarization ratio (defined as the intensity ratio of the two orthogonal polarizations) of 7.7 at 505 nm [57]. The polarized photoluminescence (PL) spectra from *m*-plane InGaN/GaN were observed to have a polarization of 3.8 at 440 nm. Matioli *et al.* reported that a polarization ratio of 16.7 and a light-extraction efficiency of 80% were achieved at 465 nm for an m-plane GaN-based LED with photonic crystal structure [58]. Wang et al. obtained highly polarized PL spectra from an InGaN LED with a multilayer wire-grid structure [62]. The polarization ratio attained was 100: 1 at 530 nm.

Highly polarized in-plane UV emission from LEDs has been reported [63-65]. Kolbe *et al.* demonstrated polarized in-plane emission at various UV wavelength from an InGaN/AlInGaN LED grown on a *c*-plane sapphire substrate [63]. They observed the in-plane emissions from the UV-LED to have a polarization ratio of 5 at 380 nm. Durnev and Karpov reported the emission characteristic of a UV-LED with an InGaN/GaN quantum well (QW) and an InGaN/AlGaN QW. The in-plane polarization ratio was 3.7 at 380 nm [64]. Schade *et al.* obtained the polarized emission from a strained InGaN QW grown on a semi-polar GaN substrate by PL measurements [65]. However, a high-quality freestanding GaN substrate, which is very expensive and bulky, is required to reduce the dislocation density in the non- or semi-polar QWs [66].

Highly polarized emission without loss of the emission intensity can be achieved by using a high-contrast SWG above a c-plane GaN-based LED. The schematic diagram of LED with SWG is shown in Fig. 1.3 (c). Because this LED type can be fabricated on a

c-plane sapphire, which was generally used in crystal growth process, the cost of fabrication can be low. The enhancement of the light extraction efficiency also can be expected, because the light escape cone at the interface between LED and the SWG structure was broadened by the coupling between the incident wave and the eigenmode within the SWG. In addition, the very small device size can be achieved due to the nano order SWG structure. Thus, the LEDs with SWG have great advantages for low loss, and the integration, compared with traditionally LED devices, and can help to reduce the fabrication cost.

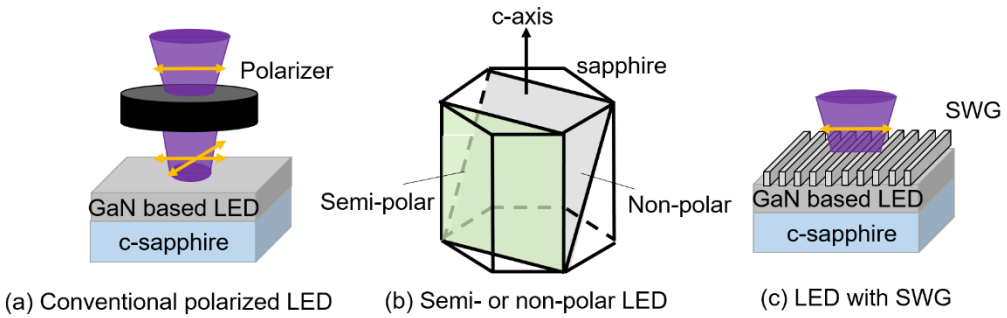

Figure 1.3 various types of GaN-based polarized LED structure

1.2.2 Refractive index detection device with SWG

The detection system of the refractive index is highly required in various application, including bioassays, medical, chemical, and engineering [67-69]. These applications require very high sensitively, integration size, label free detection. The various types of the optical refractive index sensor have been ever reported [67-77].

Coupling of the evanescent wave with surface-plasmon (SP) was widely used to detect the minuscule change of the refractive index [70]. The extremely high sensitively of refractive index detection can be achieved, because the coupling condition of SP with the light is strongly depended on the environment of the surface. The optical

geometries including a prism were generally required to couple the light wave with the SP, and the large system size is not suitable for the integration devices. The Localized-Surface-Plasmon-Resonance (LSPR) in various nanoparticle shapes was utilized for development of the compact refractive index sensor without the prism coupling [67, 69, 71]. The detection type based on LSPR is suitable for the integration device owing to the miniaturized system size. The optimized performance of the devices still require the complex and special experimental setup, for example the oblique incident geometry, and this restricts in the widely use of the detection system. Several groups have reported the highly sensitive detection of the refractive index based on guided-mode resonance (GMR) have been reported [68,72]. The sensing range of the refractive index is limited by grating or guide layer, because the higher refractive index than that of the target is required in order to excite guided-mode. Recently, other type detector based on diffraction phase grating [73], evanescent filed coupling guided mode [74], Bloch surface wave [75,76]. However, the complex design, optical geometry of oblique incident, fabrication, are required for the optimized performance of the devices, and the widely use of these devised is restricted.

High-contrast subwavelength grating based refractive index detection device can overcome these issue. Recently, high-contrast SWG based biosensor, which Si grating surrounded by low refractive index media, have been reported [77]. The high contrast SWG based sensor shows higher sensitive detection of refractive index than that in other structures. The high sensitivity was also obtained with surface normal coupling system. Thus, the SWG based refractive index sensor has many benefits for the integration applications. However, the detection targets is restricted, because the Si-grating is not stable for various target.

In this study, we try to develop Si_3N_4-SWG based refractive index detection devices in order to realize highly sensitive refractive index detection for its value with wide range. The Si_3N_4 is suitable for the wide range detection of refractive index, because Si_3N_4 is very chemically stable material and have almost no dispersion at broad wavelength region.

1.3 Overview of this thesis.

The overview of this dissertation is as follows. In chapter 2, we described the fundamental propagation property of the eiegenmode in the SWG. Maxwell's equation, the analytical models of the SWG, and calculation methods for the electromagnetic filed distribution were explained. In chapter 3, the propagation property of the SWG eiegenmode in the UV wavelength region was described. Then, the electromagnetic filed distribution within the SWG was calculated, and the propagation mechanism of the mode was discussed for the design concept of the integration UV device utilizing the SWG. In chapter 4, a polarized emission from GaN-based UV-LED with the SWG was demonstrated. At first, the fabrication process of the SWG on the surface of UV-LED was explained. Secondly, the EL emission spectra from the UV-LED was discussed. The discussion suggest the suppression of the diffraction phenomena at the interface between the SWG and LED improve the polarization characteristic of the UV emission. In chapter 5, a highly polarized GaN based UV-LED with Si-SWG/SiO_2 under layer structure was experimentally demonstrated suppressing the diffraction phenomena at the interface between SWG and LED. At First, it was showed that the low refractive index under layer was useful to suppress the diffractions at the interface between the SWG

and LED. Secondly, the fabrication of this structure is described, and the emission characteristics from the LED was discussed. In chapter 6, the influence of the grating shape deviation from a ideal rectangle on the optical characteristics of the SWG was discussed for the practical device fabrication. The influence of the grating shape was estimated by the calculated electromagnetic field distribution. Then, the fabrication process of a trapezoid-shaped SWG structure on the GaN-based LED surface was described. The EL spectra from the LED was evaluated to experimentally verify the influence of the shape deviation on the device performance. In chapter 7, a highly sensitive refractive index sensor was experimentally demonstrated using the Si_3N_4-SWG. The electromagnetic field distribution in the SWG was calculated and discussed by FDTD method and wavenumber dispersion relation to design the structure for highly sensitive detection of the surrounding refractive index. The fabrication processes of the designed SWG was described, and the experimental performance of designed SWG for the refractive index detection was evaluated and discussed. In chapter 8, this thesis is summarized.

,

Chapter 2: Fundamental property of the eigenmode in SWG structure

2.1 Introduction

In chapter 2, the ever reported fundamental propagation property of the eigenmode in the SWG was summarized. In section 2.2, the wave equation is derived from Maxwell's equations to explain light-matter interaction and to elucidate the physical behavior of the eigenmode within the SWG. It is shown that the physical behavior of the mode depends on the propagation constant. In section 2.3, the analytical models for SWG to see what kind of the eigenmode exited in what kind of situation was described, and. the surface-plasmon-resonance (SPR) model, which treats the coupling of light with the collective oscillation of electrons, the guided-mode-resonance (GMR) model, which treats the coupling the guided-mode with the light, and Bloch-mode resonance model, which relates to the coupling of light with the eigenmode owing to the periodic refractive index distribution, were explained, because one encounter these eigenmode sets in the SWG structure. In section 2.4, the calculation methods for the electromagnetic field in a SWG, such as effective medium theory (EMT), metal-insulator-metal (MIM), rigorous coupled mode analysis, and finite-difference time- domain (FDTD) method were described to estimate propagation characteristics of the eiegnmode.

2.2 Maxwell's equations in the material

The light-matter interaction is determined by Maxwell's equations. We want to solve Maxwell's equations in periodic permittivity distribution in order to estimate the propagation property of the eiegnmode in the SWG. At first, we drive the wave equation from the Maxwell's equations in the material. When the light wave was radiated into the material, the incident light wave interact with the charged particles (e. g. electrons, ions) and generates the secondly light wave. The four Maxwell's equations are given by [78,79]

$$div\mathbf{E}(z,t) = \frac{\rho}{\varepsilon} \tag{2.1}$$

$$div\mathbf{B}(z,t) = 0 \tag{2.2}$$

$$rot\mathbf{E}(z,t) = -\mu \frac{\partial \mathbf{H}(z,t)}{\partial t} \tag{2.3}$$

$$rot\mathbf{B}(z,t) = \mathbf{J_f} + \frac{\partial \mathbf{D}(z,t)}{\partial t} \tag{2.4}$$

Where the symbols ***D***, ***H***, ***B***, ***E*** are electric displacement vector, magnetic field vector, magnetic flux density vector, and electric filed vector, respectively. The symbols ρ and $\boldsymbol{J}_f$ are total true charge density per unit volume and current density per unit area, respectively. The symbols μ and ε are the permeability and the permittivity in the medium, and these are given by

$$\mu = \mu_r \mu_0 \tag{2.5}$$

$$\varepsilon = \varepsilon_r \varepsilon_0 \tag{2.6}$$

where, μ_r μ_0, ε_r and ε_0 are relative permeability, permeability, relative permittivity, and the permittivity in vacuum. In optical region of frequency, permeability was assumed $\mu \approx \mu_0$, the magnetization cannot follow the optical frequency. The permittivity was defined by the equation of the motion, and the response of the matter for the light is represented as ε. Now, the ρ and $\boldsymbol{J_f}$ are related to the polarization in the material, and these term was rewritten by polarization vector ***P***. The ***P*** vector was defined as the sum of the dipole moment in unit volume, namely the space average of positive and negative charge displacement. The total charge density ρ was sum of the free charge density ρ_f and electric polarization charge density ρ_p, and was given by

$$\rho = \rho_f + \rho_p \tag{2.7}$$

The ρ_p is caused by divergence of ***P*** [79].Now, the ρ_f was zero, because we consider the neutral (a number of positive charge = negative charge). Thus, total charge density *p* was given by

$$\rho = -div\boldsymbol{P} \tag{2.8}$$

Here, the relation between ***E***, ***D*** and ***P*** vector is given by

$$\mathbf{D} = \varepsilon_0 \mathbf{E} + \mathbf{P} = \varepsilon_r \varepsilon_0 \mathbf{E} = \varepsilon \mathbf{E} \tag{2.9}$$

On the other hand, the total current density ***J*** vector was composed of the electric current by free electron $\boldsymbol{J_f}$, polarization current $\boldsymbol{J_P}$ and magnetic current $\boldsymbol{J_m}$. In the optical region of frequency, the $\boldsymbol{J_m}$ can be neglected, and we can assume $\mu \approx \mu_0$. For the optical electric field oscillating with a certain period, $\boldsymbol{J_f}$ is considered as the oscillating current, namely polarization current with eigen frequent = 0 [79].The total current density ***J*** was

$$\boldsymbol{J} = \boldsymbol{J}_f + \frac{\partial \boldsymbol{D}}{\partial t} = \boldsymbol{J}_f + \varepsilon_0 \frac{\partial \boldsymbol{E}}{\partial t} + \frac{\partial \boldsymbol{P}}{\partial t} = \varepsilon \frac{\partial \boldsymbol{E}}{\partial t} \tag{2.10}$$

Equation (2.10) indicates that the response of the material is represented as the permittivity ε. If the electric current exist in the material, the term of ε in eq. (2.10) have the imaginary part, whereas the only real part without electrical current. In general, ε is complex number because the contribution of the electric current was contained.

The wave equation was derived from eq. (2.1) ~ (2.4), and (2.10), and the equation is given by

$$\nabla^2 \boldsymbol{H}(x, y, z, t) = -\omega^2 \varepsilon \mu \boldsymbol{H}(x, y, z, t) \tag{2.11a}$$

$$\nabla^2 \boldsymbol{E}(x, y, z, t) = -\omega^2 \varepsilon \mu \boldsymbol{E}(x, y, z, t) \tag{2.11b}$$

Equation (2.11a) and (2.11b) determine the time and space behaviors of the light wave in the material. The electromagnetic response of the material is represented as ε, so equation (2.11a), (2.11b) contain the light-matter interaction. Hence, the solutions of these equations determines the physical behavior of light in the material. The solution of eq. (2.11a), (2.11b) is called ‘eigenmode’. Here, we assume the solutions of plane wave

propagating along *z*-axis. For simplicity, the magnetic and electric field are only y-component E_y. These filed is independent on the *x*- and *y*-coordinates ($\frac{\partial}{\partial x} = \frac{\partial}{\partial y} = 0$), because we consider the plane wave propagating along *z*-direction. We also the property of the eigenmode strongly depends on the spatial relative permittivity distribution. Here, we consider the plane wave solution of eq. (2.11b) given by

$$E_y = E_0 \exp(\pm ikz) \tag{2.12}$$

, where, symbols E_0 are amplitude of the electrical field, The symbol *k* is wavenumber, namely propagation constant, and the relation between *k*, angular frequency ω and light speed in the material *c* is

$$\omega = ck \tag{2.13}$$

Eq. (2.12) shows that the behavior of the eigenmode strongly depend on the wavenumber *k*. We discussed this difference of the behavior, because this is very important to consider the propagation properties of the eigenmode.

Dependence of the physical behavior of light wave on propagation constant are shown in Fig. 2.1, and the behavior are distinguished into the three types. In the case of the real propagation constant, the light wave propagates energy, and the intensity do not decrease as shown in Fig.2.1 (a). This type of light is called "*propagation wave*". If the propagation constant was pure imaginary number, the light intensity exponentially decays, and the light wave cannot propagate the energy for the *z*-direction. Hence, this light wave become surface bounded mode as shown in Fig. 2.1 (b). This type of light is

called “*evanescent wave*”, and it is often encountered the evanescent wave in total reflection phenomena. Third type of wave is the case of the complex propagation constant as shown in Fig. 2.1 (c). When the propagation constant is the complex number, the mode propagate the light energy with the decreasing the light intensity. The real part and the imaginary part of propagation constant contribute the phase and the decay of light, respectively.

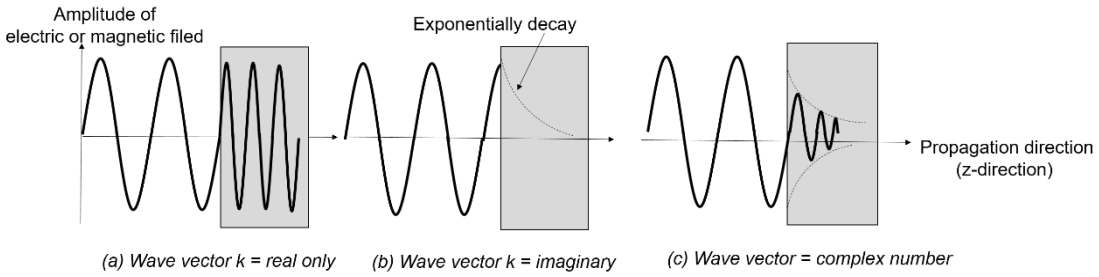

Figure 2.1 Types of light wave:
(a) with a real propagation constant (b) a imaginary (c) a complex

2.3 Analytical models of SWG structure

In this section, the analytical model ever proposed to reveal what kind of eigenmode exited in the SWG was described. The models are as follows. 1: SPR model [80], which treats the light coupled with the collective oscillation of the electron, 2: Guided-mode-resonance (GMR) model, in which the optical characteristics of the SWG was described by light coupling with leaky-guided-mode in waveguide [82-90], 3: Bloch-mode-model, in which the Bloch-mode due to the periodic refractive index distribution determined the optical characteristics of the SWG [47-49,91].

2.3.1 Surface-plasmon-resonance (SPR) model

In SPR model, the coupling of light with collective oscillations of free electrons at the surface determined the optical response of the SWG [80]. Plasmon is a collective oscillations of charged particles, such as free electrons or ion and the elementary excitation in plasma or metal. Surface-plasmon is a compressional wave of the electron and longitudinal wave, in which the electric field is parallel to the propagation direction. Hence, the coupling of the plasmon with light wave cannot be occurred in the bulk materials, because the light wave is lateral wave, in which the direction of the electric or the magnetic field is perpendicular to the propagation direction of light.

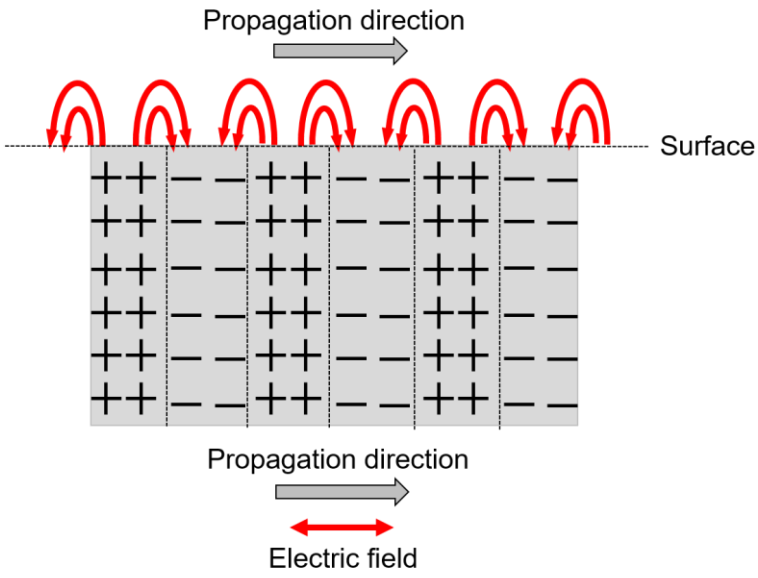

Figure 2.2 Schematic diagram of surface plasmon

If the surface appears, the plasmon can couple with the incident light wave at a certain conditions. The schematic diagram of the plasmon is shown in Fig. 2.2. In the surface, the plasmon penetrates outside the material and has the lateral component of the electric filed. Thus, this plasmon can be excited by the light wave at a certain conditions. This type of the elementary excitation is called “surface plasmon”.

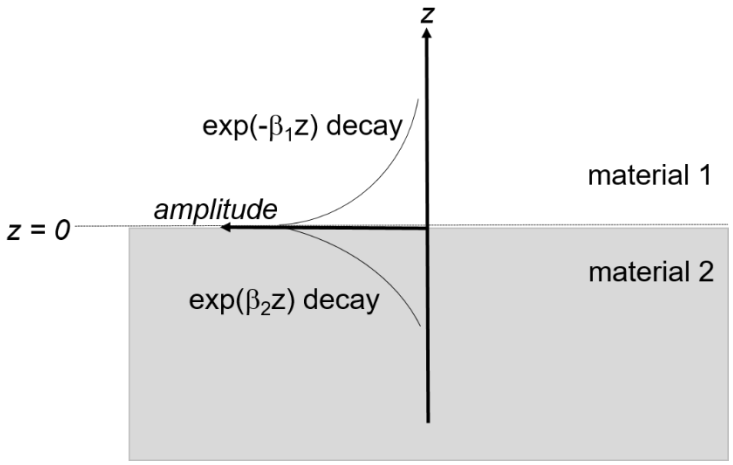

Figure 2.3 Field of the surface boundary mode

To explain the existence condition of the SP, we consider geometry as shown in Fig. 2.3. In Fig.2.3, the two material contact each other at *z = 0*. The relative dielectric constant and the permeability in the material *1* and *2* are ε_1, ε_2, μ_1, and μ_2, respectively. The field of SP along *z*-direction is surface bounded wave and exponentially decay from the interface. The field is given by [80]

$$S_1 = S_0 \exp[i(k_x x - \omega t)] \exp(-\beta_1 z) \qquad z \geq 0 \qquad \text{(2.14 a)}$$

$$S_2 = S_0 \exp[i(k_x x - \omega t)] \exp(\beta_2 z) \qquad z \leq 0 \qquad \text{(2.14 b)}$$

S_1 and S_2 mean the electric field for p-polarization or the magnetic field for s-polarization, respectively. S_0 is the amplitude of the field at $z = 0$. From the boundary condition, the excitation condition of the surface plasmon is obtained as following equations.

$$\frac{\varepsilon_1}{\varepsilon_2} = -\frac{\beta_1}{\beta_2} \qquad \text{for p-polarization} \qquad (2.15\ a)$$

$$\frac{\mu_1}{\mu_2} = -\frac{\beta_1}{\beta_2} \qquad \text{for s-polarization} \qquad (2.15\ b)$$

In optical wavelength or shorter wavelength region, the magnetization cannot follow up the magnetic field of the light, and the relative permeability is nearly 1. Thus, SP polariton is generally formed only for p-polarization.

The law of energy and momentum conservation must be satisfied for the coupling the light wave and SP. In other words, the dispersion relations (energy-momentum relation) of the light wave and the SP must have the intersection to couple each other. However, the lateral wave vector component of the SP is constantly larger than that of the propagation light. This indicate the propagation light cannot excite SP. The evanescent wave is employed for the excitation of SP. The dispersion relation line of the evanescent lies below the light line, and the dispersion curves of SP and evanescent wave have the intersection. Hence, the evanescent wave can couple with the SP. Generally, the evanescent wave is formed by total reflection in the prism. The diagram of this coupling by the prism is shown in Fig.2.4. The evanescent wave

exponentially decays as the distance from the surface increase. If the surface of material exist within the decay length of the evanescent wave, the energy of light can be transported to the SP, and the reflected light vanishes.

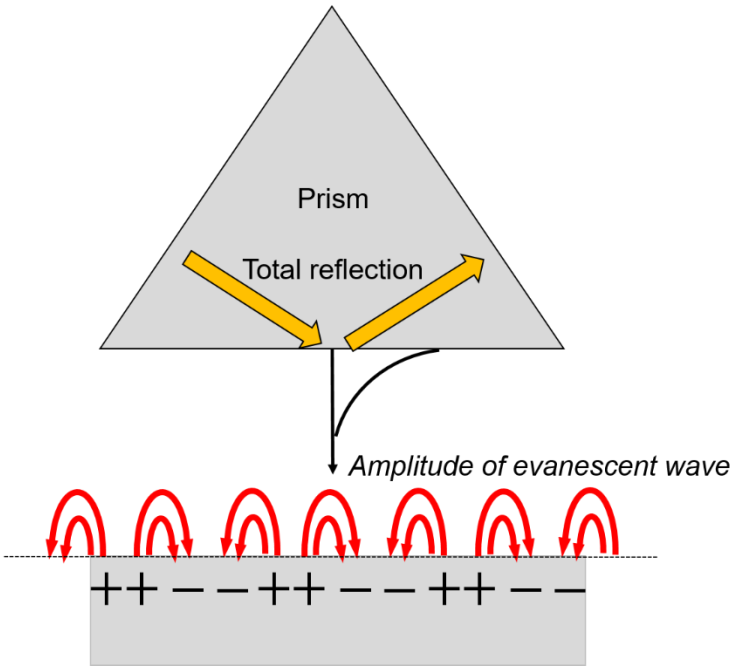

Figure 2.4 Cross section coupling of SP mode with the evanescent wave

To match the lateral wave vector of the light and SP, the grating structure is also used. The geometry of the grating coupling is shown in Fig 2.5. The wave vector along x-direction of the diffracted light k_x by grating is

$$k_x = k_0 \sin\theta + \frac{2\pi n}{\Lambda} \tag{2.16}$$

θ is the incident angle determined as Fig. 2.5. The second term of the right side of eq. (2.16) indicates the lattice vector. The diffracted light with *x*-component k_x larger than k_0

became the evanescent wave for z-direction. When the k_x coincided with the SP wave number k_{sp}, the diffracted light coupled with SP. The SP is widely used for high sensitive sensor, enhancement of electric filed, emission pattern control of LED.

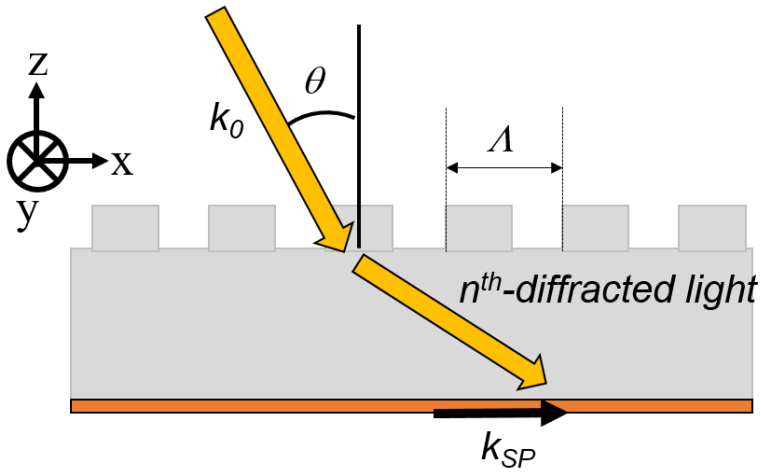

Figure 2.5 Grating Coupler

1-dimensional (1-D) or *2D*-plasmonic structures are proposed to control the plasmon propagation characteristics. The diagram of *1D* or *2D* plasmonic structure is shown in Fig 2.6. The *1D*-plasmonic structure is exactly a metal grating. The band gap, which forbids the propagation of light in plane, occurs in the plasmonic structure. This gap is called “plasmonic band gap”. The plasmonic band gap is caused by Bragg reflection, and the detail is explained in the section 2.3.3.1. The SP model can explain the wood’s anomaly phenomena. However, the anomalies for s-polarized light cannot be explained, because the SP cannot be excited by s-polarized incident light.

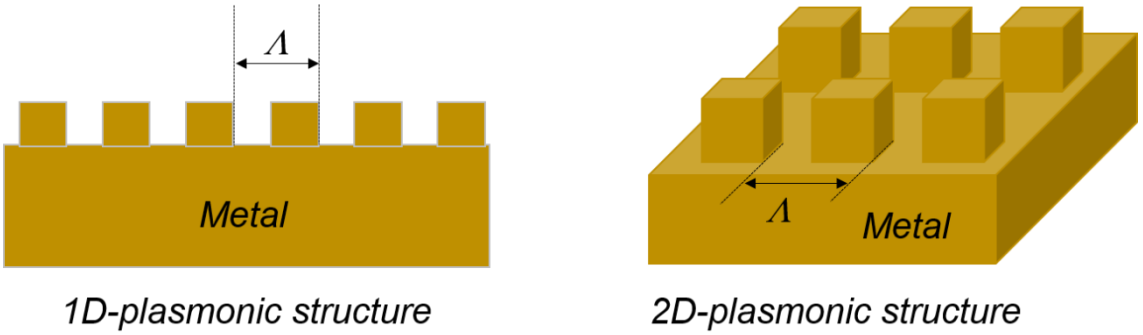

Figure 2.6 Various dimensional plasmonic structure

2.3.2 Guided-mode-resonance (GMR) model

In GMR model, the optical characteristics of the SWG is defined by the coupling of the incident light with the leaky guided mode. In 1985, an extraordinary strong reflection in thin dielectric grating with high refractive index layer at a certain incident conditions have been discovered by L. Mashev and E. Porov [81]. This phenomena is related with the guided-mode in the high refractive index guide-layer is called “Guided-Mode-Resonance”.

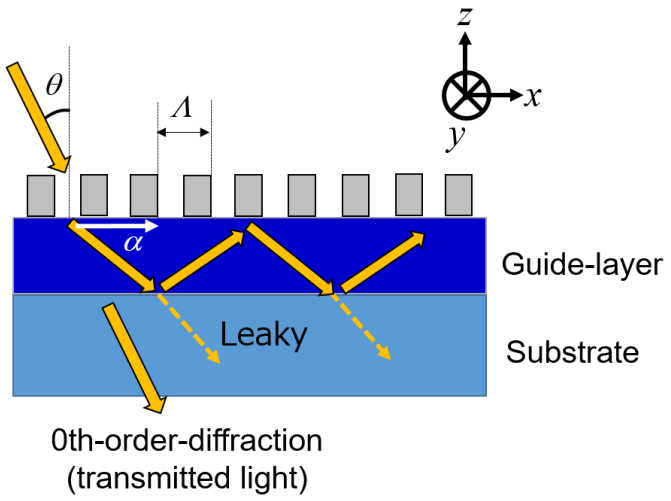

Figure 2.7 Geometry of GMR filter

Figure 2.7 shows diagram of GMR filter. In Fig. 2.7, thin grating is arranged on the guide-layer. Here, the term of “*Thin*” indicate the grating thickness is near the wavelength. The grating period Λ is sub wavelength. The diffraction outside the grating is only 0th-order and the others are the evanescent wave. When the lateral wavenumber component of the incident light matches with that of the guided-modes, the energy of the incident wave transforms into the guided-modes. The phase matching condition between the incident light and the guided-mode is [82]

$$k_0 \sin\theta + \frac{2\pi n}{\Lambda} = \alpha \qquad (n = 1,2,3...) \qquad (2.17)$$

Where the symbol k_0, n, θ, α are a wavenumber of the incident wave, diffraction order, the incident angle, and the wavenumber of the guided-modes for *x*-direction, respectively. If the phase matching condition is satisfied, the diffracted incident light coupled with the guided-mode in the guide-layer, and the diffracted light propagates in the guide-layer with total internal reflections. The guided-modes are reradiated into both incident side and substrate side. The guided-mode is often called "*leaky-mode*", because the energy is leaked into outside the guide-layer via the reradiating due to the several diffractions of the grating [83-85]. The phase of the reradiated light into the substrate is shifted by π from the 0th-order diffraction, and the transmitted light is canceled by the reradiating from the leaky-mode [84]. As a result, the diffraction wave is appeared in only incident side, and a strong diffracted light along the mirror reflection direction is occurred. The light wave, which do not satisfied the phase-matching condition, is not coupled with the guided-mode, and the incident light through the guided-layer as thin film. The narrow band filter can be realized by using GMR [86-90]. The wavelength, which satisfies the phase mating condition, is very narrow, and the reflection spectrum is Lorentz type [82].

When the grating has the high refractive index, the grating layer serves wave guide layer. The guide layer with grooves works as GMR filter. R. Magnusson and M. Shokooh-Saremi explained the physics of the high reflectivity property of SWG, based on leaky-mode propagating along *x*-direction [85]. This approach shows fast conversion and well explains the guided mode resonance properties. However, the approach is

qualitative and agree with only for up to third-order leaky-modes of p-polarization. The approach agreement is only for the low refractive index contrast of the grating [47,85].

2.3.3 Bloch-mode model

In this section, the Bloch-mode model proposed by V. Karagodsky *et al.* for investigation of the SWG optical characteristics was presented [47-49]. In this model, the incident light couples with Bloch-eiegenmode due to the refractive index distribution, and the coupling determined the SWG optical response.

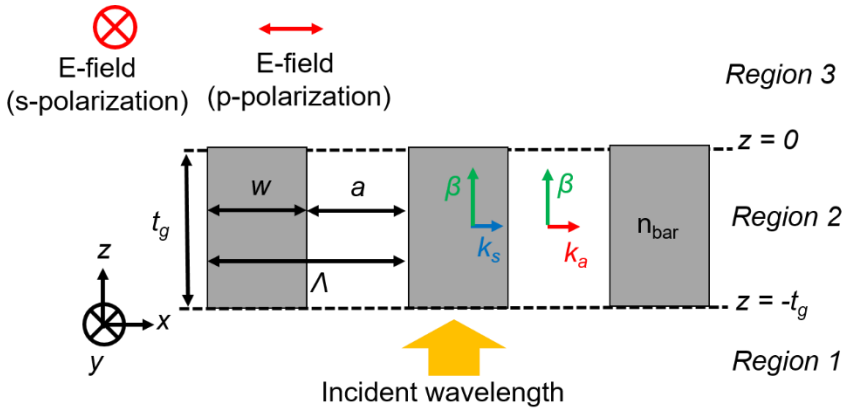

Figure 2.8 Bloch-mode model

The model provided the wavevector dispersion relation of the eigenmode in SWG and explained the extraordinary features of the SWG very well. The analytical model is shown in Fig. 2.8. In this model, the region calculated is divided into three region: *Region 1* indicates "*incident region*", *Region 2* is *"SWG region"*, and *Region 3* indicates *"transmitted region"* The SWG was arranged with the grating period Λ, and the grating is surrounded by air (refractive index of air = 1). The width of the grating stripe and air-gap, defined in Fig. 2.8 are denoted as symbol *w* and *a*, respectively. The symbol of t_g is the grating thickness. Now, p-polarized normal incident light, whose magnetic field

is along y-direction, was assumed for simplicity. The magnetic *H* and electric field *E* distribution in each regions are given by

Region 1 (Outside the SWG)

$$H_x^{\mathrm{I}}(x, z \le -t_g) = \exp[-j(2\pi/\lambda)(z+t_g)] - \sum_{n=0}^{\infty} r_n h_{y,0}^{out}(x)\exp[+j\gamma_n(z+t_g)] = \sum_{n=0}^{\infty}(\delta_{n,0} - r_n)h_{y,n}^{out}(x)\exp[+j\gamma_n(z+t_g)] \quad (2.18\text{ a})$$

$$E_x^{\mathrm{I}}(x, z \le -t_g) = \eta\exp[-j(2\pi/\lambda)(z+t_g)] + \sum_{n=0}^{\infty} r_n e_{x,0}^{out}(x)\exp[+j\gamma_n(z+t_g)] = \sum_{n=0}^{\infty}(\delta_{n,0} + r_n)e_{x,n}^{out}(x)\exp[+j\gamma_n(z+t_g)] \quad (2.18\text{ b})$$

Region 2 (Inside the SWG)

$$H_y^{\mathrm{II}}(x, -t_g \le z \le 0) = \sum_{m=1}^{\infty} h_{y,m}^{in}(x)[a_m\exp(-j\beta_m z) - \rho_m a_m\exp(+j\beta_m z)] \quad (2.19\text{ a})$$

$$E_x^{\mathrm{II}}(x, -t_g \le z \le 0) = \sum_{m=1}^{\infty} e_{x,m}^{in}(x)[a_m\exp(-j\beta_m z) + \rho_m a_m\exp(+j\beta_m z)] \quad (2.19\text{ b})$$

Region 3 (Outside the SWG)

$$H_y^{\mathrm{III}}(x, z \ge 0) = \sum_{n=0}^{\infty} \tau_n h_{y,n}^{out}(x)\exp(-j\gamma_n z) \quad (2.20\text{ a})$$

$$E_x^{\mathrm{III}}(x, z \ge 0) = \sum_{n=0}^{\infty} \tau_n e_{x,n}^{out}(x)\exp(-j\gamma_n z) \quad (2.20\text{ b})$$

, where the symbol η is impedance of vacuum and the value of that is 120π. The symbol $\delta_{n,0}$ indicates Kronecker's delta function, which is 1 at only *n = 0*, and the value is *0* in the other case. Where *n = 0, 1, 2...* and *m = 1, 2…* are the diffraction order outside the SWG and the eigenmode order inside the SWG. The a_m is amplitude of the field of the mode, ρ_m is reflection coefficient of the mode. The symbol τ_n and r_n are the coefficient of

the transmission and reflection of diffraction. β_m are longitudinal (*z*-direction) wave number vector in region 2. h^{out}_y and e^{out}_x are the lateral magnetic and electric field profile in *region 1* and *3*, and given by

$$h^{out}_{y,n}(x) = \cos[2n\pi / \Lambda(x - a/2)] \quad \text{(2.21 a)}$$

$$e^{out}_{x,n}(x) = (\gamma_n / k_0)\eta h^{out}_{y,n} \quad \text{(2.21 b)}$$

The γ_n is longitudinal (*z*-direction) wave number vector outside the SWG (*region 1* and *3*). The relation between λ and γ_n is given as

$$\gamma_n^2 = \left(\frac{2\pi}{\lambda}\right)^2 + \left(\frac{2n\pi}{\Lambda}\right)^2 \quad \text{(2.22)}$$

In the subwavelength structure, Eq. 2.22 indicates the γ_n become the imaginary number except for *n = 0.* This indicates the higher order diffractions except for 0th-order diffraction (*n = 1, 2 …*) become evanescent type, whose amplitude exponentially decays. Hence, the energy of light through the SWG is propagated by only 0th-order diffraction.

The symbol of k_a and k_s shown in Fig. 2.8 are the lateral-direction (*x*-direction) wavenumber vector in air-gap and grating bar, respectively. By the continuity of the electromagnetic field at *x* = 0 and *a* in Fig 2.14, the wavenumber dispersion relation between k_a and k_s for p-polarization can be obtained as [47]

$$n_{bar}^{-2} k_{s,m} \tan(k_{s,m} w/2) = -k_{a,m} \tan(k_{a,m} a/2) \quad (m = 1,2,3\cdots), \quad \text{(2.23)}$$

where the symbol of n_{bar} is refractive index of the grating bar. The wavevector relationship

between k_s or k_a and β_m is also given by

$$\left(\frac{2\pi}{\lambda}\right)^2 - k_{a,m}^2 = \left(\frac{2\pi n_{bar}}{\lambda}\right)^2 - k_{s,m}^2 = \beta_m^2 \quad (m = 1,2,3\cdots) \tag{2.24}$$

For the s-polarization, whose electric field is along y-direction, dispersion relation, the n_{bar} term in Eq. (2.23) is replaced by 1. The solutions of eq. (2.23) and (2.24) indicate that the energy of the incident light wave can move into the eigenmode wave. Further, the solutions in ascending order correspond to eigenmode order *m*. The propagation constant β_m can be obtained by solving eq. (2.23) and (2.24). V. Karagodsky *et al.* found the dispersion relation of high contrast grating with n_{bar} = 3.48, which material was assumed Si. The dispersion relation is shown in Fig. 2.9. The curves and broken lines indicate eq. (2.23) and (2.24), respectively. The intersection of the curve and broken line indicates the coupling condition of the mode with the incident light. The cutoff line in Fig. 2.9 represents $\beta_m = 0$, namely, $k_s = n_{bar}k_a$. The mode, which has the intersection below the cutoff line, is evanescent mode for *z*-direction. On the other hand, the mode having the intersection above the cutoff line is propagating mode. When the wavelength becomes much larger than the grating period ($\lambda >> \Lambda$), the modes except for the first-order mode become evanescent mode. The lateral wave number of the first mode approaches 0. This means the grating profile is vanished, and the grating approached the uniform layer with the effective index value predicted via effective medium theory

mentioned in section 2.4.

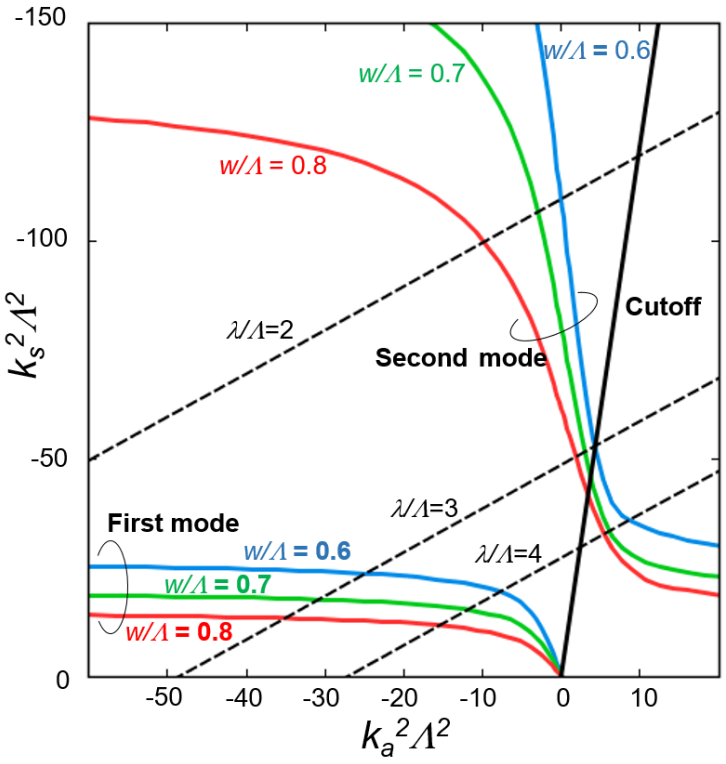

Figure 2.9 Dispersion relation between k_a and k_s in the SWG with n_{bar} = 3.48 for p-polarized incidence. This dispersion relation is calculated by author referring [47]

Here, consider the high reflectivity and high transmission condition and the relation between the grating parameters and the phase of the eigenmode. In the previous section, it is shown that the longitudinal wave number β_m depends on the grating period, and filling factor. The propagation length along *z*-direction is determined by grating thickness t_g. In Fig.2.8, the phase ϕ_m of the eigenmode at the interface between the *region 2* and *3* can be given by

$$\phi_m = \beta_m t_g \qquad \text{(m = 1, 2,3…)} \qquad (2.25)$$

Eq. (2.25) represents the phase accumulation of each modes when they propagate in the SWG. When the mode reached the interface between *region 2* and *3*, the modes return back to the incident plane owing to large index distribution change. Then, the modes couple each other during reflection at the interface between *region 2* and *3* [47-49]. This reason is as follows. The reflection relates with the interaction between the outside wave and the mode in SWG. The outside wave (for example 0th-order diffraction) is not orthogonal to the modes within the SWG. As a result, the each mode coupled each other via the reflection at the interface between *region 2* and *3*. In the SWG, only 0th-order diffraction propagates the energy (other higher-order diffractions are evanescent mode). If the transmitted coefficient of 0th-order diffraction τ_0 become to zero, the incident energy is full reflected back. Hence, the reflectivity of the SWG reaches 100 %. The transmitted coefficient of 0th-order τ_0 is given by

$$\begin{aligned}\tau_0 &= (\eta\gamma_0 / k_0)^{-1}\sum_m (a_m + \rho_m a_m)\Lambda^{-1}\int_0^{\Lambda} e_{x,m}^{in}(x)e_{x,0}^{out}(x)dx \\ &= (\eta\gamma_0 / k_0)^{-1}\sum_m (a_m + \rho_m a_m)\Lambda^{-1}\int_0^{\Lambda} e_{x,m}^{in}(x)dx\end{aligned} \tag{2.26}$$

This equation determines the transmittance and the reflection characteristics of the SWG. Based on eq. (2.26), the high reflectively condition can be obtained when the eiegnmodes were canceled each other.

This model well explains the extraordinary characteristics of the SWG in IR wavelength region and provide a straightforward, intuitive and full analytic solution. This

analysis was performed for an SWG with real n_{bar} only, because the imaginary part of the most materials is negligible in the IR region. However, the imaginary part of the refractive index, namely photon absorption, in UV or VIS region is larger than that in IR region. Thus, the SWG property in the shorter wavelength region is quiet difference from that in IR.

2.3.3.1 Comparison with photonic-crystal (PhC)

The Bloch-mode model was also used for the investigation of the optical characteristics of 1-dimensional-photonic crystal (1D-PhC) [91]. Although the model for the SWG looks no different from that for 1D-PhC, there are the important difference between both models. In this section, we compared the two models and discussed the difference between both models. The schematic diagram of 1D-PhC is shown in Fig. 2.10. This 1D-PhC is often called “distributed Bragg reflector” (DBR). The Bloch eigenmode also exists in the PhC due to the periodic refractive index distribution. In the 1D-PhC, the photonic band gap, in which the transmittance of the light is very low, is obtained. The origin of the photonic band gap is interpreted by the split of the frequency. This can be explained as follows. At first, consider the Bloch eigenmode with x-direction wave number $k_x = \pm\pi/\Lambda$. These modes satisfy Bragg condition. Thus, the mode propagating along + *x*-direction is taken Bragg reflection by grating vector (defined as $2\pi n/\Lambda$: *n* is integer), and the direction is reversed (- *x*-direction). The mode with $k_x = +\pi/\Lambda$ was reflected one after another, and the propagation direction of the mode is reversed. Similarly, the mode with $k_x = -\pi/\Lambda$ is taken Bragg reflection. As a result, the standing wave is formed by the interference between the right- and left-propagating

modes as shown in Fig. 2.11.

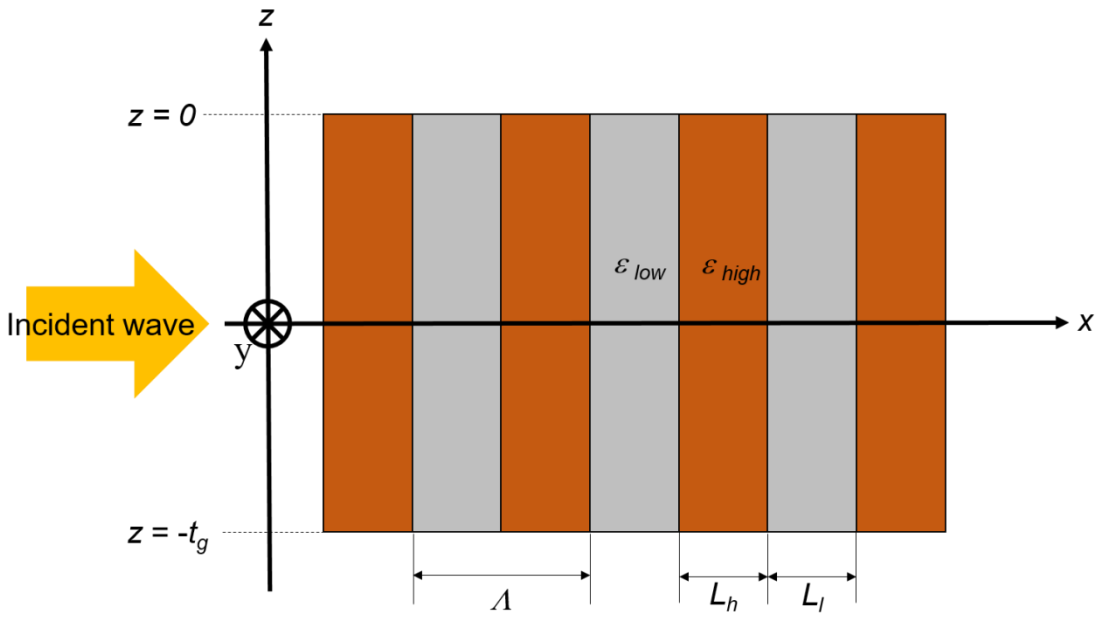

Figure 2.10 schematic diagram of 1D-PhC

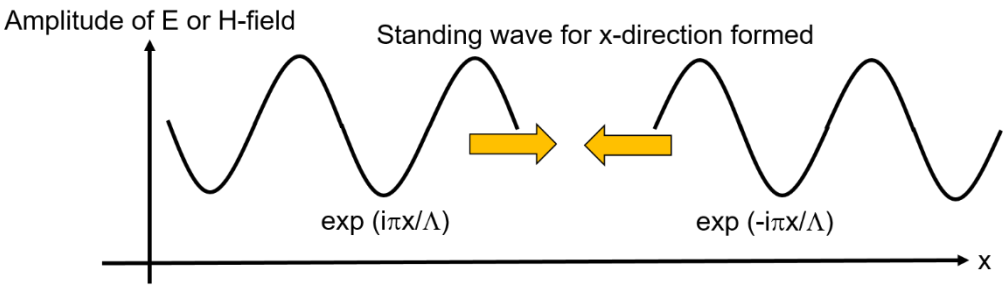

Figure 2.11 Standing wave by Bragg reflection at the edge of Brillouin zone

Then, let's discuss the important difference for distinguishing between the SWG and 1D-PhC. The grating thickness of 1D-PhC are assumed to infinite length for both *y*- and *z*-direction, and the propagation direction of wave is only x-direction. This indicates

that only *x*-direction interferences of the modes define the optical characteristics of 1D-PhC, and the interference of the grating edges at $z = 0$ and $z = -t_g$ as shown in Fig. 2.10 is vanished. Hence, the 1D-PhCs are corresponding to the SWG with infinite grating thickness [31]. On the other hand, the wavefront is distorted inside the grating in the finite grating thickness, and the interference at z = 0 and $z = -t_g$ is obtained. As a result, the optical characteristics of SWG strongly were depended on the grating thickness, and the light of the vertical direction from periodicity can be controlled by using SWG. This is the most difference between 1D-PhC and SWG and very useful for integration devices. The occurrence of the interaction at $z = 0$ and $z = -t_g$ indicate that the mode inside the SWG can coupled with the incident wave (now, plane wave is assumed). Thus, the SWGs operate above the light line in the ω-k diagram, whereas the PhCs operate below the light line [31, 91].

2.4 Calculation methods

In this section, the calculation method for the electromagnetic field distribution in the SWG to estimate the electromagnetic response of SWG structure was described. The method are as follows: 1: Effective-medium-theory (EMT) [39, 40, 82], in which periodic structure is assumed as a uniform birefringent film with effective refractive index, 2: Metal-Insulator-Metal (MIM) theory [92, 93], in which the SWG structure is assumed as the ideal the waveguide, 3: Rigorous-coupled-wave-analysis (RCWA) method [80, 94-97], in which the light in the periodic structure is expressed as the summation of the eigenmode, 4: Finite-difference-time-domain (FDTD) method [98, 99], which solve Maxwell's equations utilizing the time and space discretization. The advantages and

disadvantages of each method were discussed.

2.4.1 Effective-medium-theory (EMT) method

Effective-medium-theory (EMT) model is widely used to estimate the optical characteristics of the SWG [39, 40, 82]. In this model, SWG structure is approximated to an optically anisotropic film with effective index value n_{eff}. Figure 2.12 shows the EMT model. The incident light propagates along z-direction.

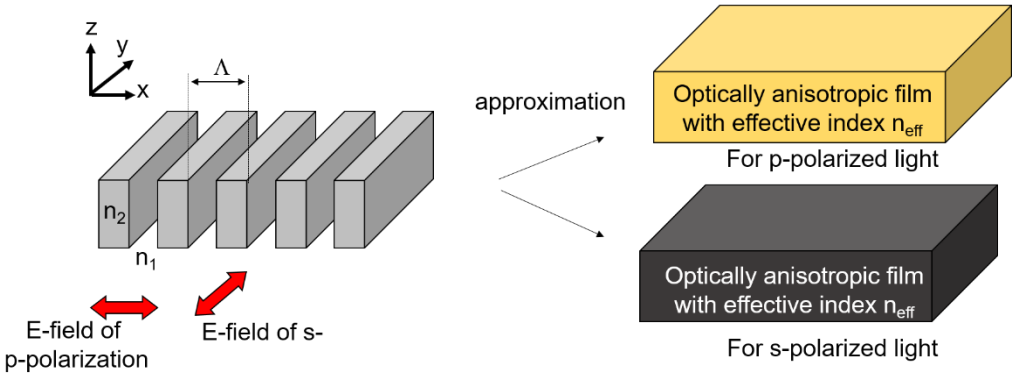

Figure 2.12 Schematic diagram of the EMT model

In Fig.2.12, n_1 and n_2 are the air-gap and the grating refractive index, respectively. F is filling factor, which is defined by the ratio the grating width to the grating period. The electromagnetic response of the structure is estimated as the optical thin film. In short, the eigenmode was approximated as plane wave. The effective refractive index of the SWG is

$$\frac{1}{n_{eff}^2} = \frac{1-F}{n_1^2} + \frac{F}{n_2^2} \quad \text{(for p-polarization)} \quad (2.27\ a)$$

$$n_{eff}^2 = (1-F)n_1^2 + Fn_2^2 \quad \text{(for s-polarization).} \quad (2.27\ b)$$

Equation (2.27 a) and (2.27 b) were employed to design various optical elements, such as wire-grid polarizer, achromatic wave-plate, anti-reflective-surface, and birefringent wave-plate [40].

The advantages of EMT model is its excess simplicity for the estimation of the electromagnetic response of the SWG. Thus, the EMT model is powerful tool for the roughly design of SWG. However, EMT is only accurate when only one propagation mode exists in the SWG and when the grating height is enough to the amplitude of all other evanescent mode is decayed [82]. This conditions are corresponds to the case that the grating period is significantly shorter than λ. As the period approaches the incident wavelength, the actual electromagnetic response in the SWG deviates from that predicted EMT [41, 43].

2.4.2 Metal-insulator-metal (MIM) method

In this section, Metal-Insulator-Metal (MIM) method was described. Some groups assumed that one period of the grating is ideal waveguide and estimated the optical characteristics of the SWG. The schematic diagram of the MIM model is shown in Fig. 2.13. The grating length along *y*-direction is infinite, because the grating length along *y*-direction is much larger than the incident wavelength.

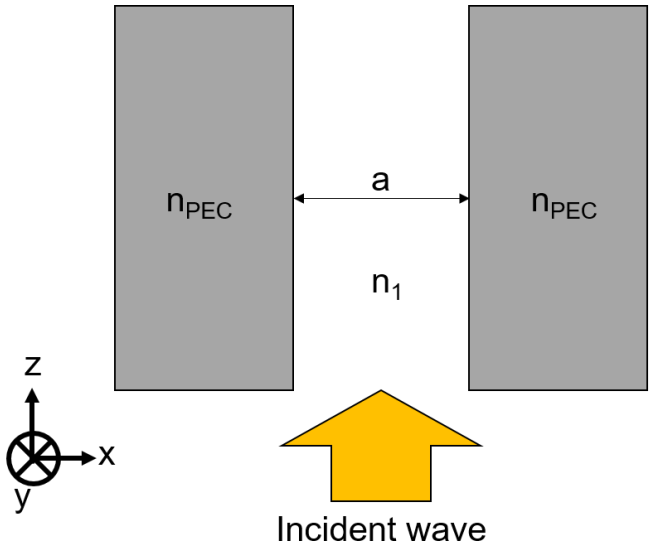

Figure 2.13 Schematic diagram of MIM method

The grating is fully surround by homogeneous material with refractive index of n_1. The air-gap width is *a*. In the region $|x| \geq a/2$, assumed a perfect electric conductor (PEC) (or ideal metal) with refractive index n_{PECl}. The electric filed cannot penetrate into PEC not at all. The total filed in the air-gap is represented as a linear superposition of the waveguide modes. The propagation constant along *z*-direction β is following equations [92,93].

$$\beta_1 = k_1 n_1,$$

$$\beta_m = \sqrt{k_1^2 n_1^2 - \frac{(m-1)^2 \pi^2}{a^2}} \quad (m = 1,2,3\ldots) \quad \text{for p-polarization} \tag{2.28 a}$$

$$\beta_m = \sqrt{k_1^2 n_1^2 - \frac{m^2 \pi^2}{a^2}} \quad (m = 1,2,3\ldots) \quad \text{for p-polarization} \tag{2.28 b}$$

where, k_1 is wavenumber in the material *1*. Equation (2.28a) indicates that the propagation constant of p-polarization, in which the direction of electrical field is perpendicular to the grating, lowest-order ($m = 1$) waveguide mode is always real, no matter how short *a* is. On the other hand, the propagation constant of s-polarized mode, in which the electrical field is in the grating direction, is imaginary value when *a* is shorter than $\lambda_1/2n_1$ (the λ_1 is the wavelength in the medium with n_1). Thus, the transmittance of p-polarization is high while that of s-polarization is very low at the *a* shorter than $\lambda_1/2n_1$.This analytical method well explains the optical characteristics of the wire grid polarizer.

However, some of the SWG extraordinary properties, such as high reflectivity of p-polarization, cannot be predicted via this model. The origin of disagreement is attributed to the interaction between the waveguide mode in air-gap and that in the neighboring waveguide mode. The schematic diagram of the interaction is shown in Fig. 2.14. If the grating is finite conductivity material or dielectric material, the field of the mode in air gap penetrates into the grating region, and the field is overlapped each other. As a result, the mode profile no longer is that of the isolated waveguide mode. Thus, MIM model cannot apply when the grating width is not enough to decay the field.

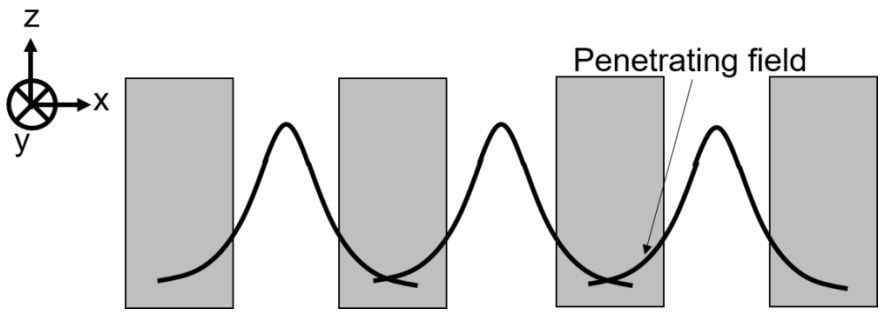

Figure 2.14 Penetration of the field of neighboring mode

2.4.3 Rigorous-coupled-wave-analysis (RCWA) method

RCWA is calculation method for the estimation of the electromagnetic field. RCWA was developed by Moharam and Gaylord [94-97]. Here, we consider the case of the incident light into grating to explain the RCWA method [80]. The RCWA model of this case is shown in Fig. 2.15. In this method, optional structure is divided into multilayers. The dielectric constant in each layers depend on only for *x*-direction and not for *z*- and *y*-directions. Inside each layer, the field of the light wave is given by the summation of the infinite sets of the eigenmode with space harmonic components. The s-polarized fields are given by

$$E_y^{(l)} = \sum_m S_{y,m}^l(z)\exp(ik_{x,m}x). \tag{2.29a}$$

$$H_x^{(l)} = i\left(\frac{\varepsilon_0}{\mu_0}\right)^{\frac{1}{2}} \sum_m U_{x,m}^{(l)}(z)\exp(ik_{x,m}x). \tag{2.29a}$$

$$k_{x,j} = k_0 n^{(L)} \sin\theta + \frac{2\pi m}{\Lambda}. \tag{2.30}$$

where $U_{y,m}^{(l)}$ and $S_{y,m}^{(l)}$ are the field amplitude of m^{th} wave, θ is the incident angle. The wave in the layer propagates along + *z* and – *z*-directions. The symbols of $d^{(L)}$ and $u^{(L)}$ in Fig. 2.15 are the weight coefficient of the modes propagating along +z- and –z-direction in L^{th} layer. These coefficient are determined to match the boundary conditions at the interfaces at each layers.

For s-polarized wave, the fields are given by

$$H_y^{(l)} = \sum_m U_{y,m}^l(z)\exp(ik_{x,m}x)\,. \tag{2.30a}$$

$$E_x^{(l)} = \frac{1}{i\omega\varepsilon_0\varepsilon(x)}\frac{\partial H_y^{(l)}}{\partial z}\,. \tag{2.30b}$$

$$E_z^{(l)} = -\frac{1}{i\omega\varepsilon_0\varepsilon(x)}\frac{\partial H_y^{(l)}}{\partial z}\,. \tag{2.30c}$$

RCWA provide the steady-state solutions in the frequency region, and very powerful tool for estimation of the SWG optical characteristics. The weight of each order mode is also obtained. However, intermediate state of the filed in the SWG is not provided, and not suitable for our purpose. Thus, FDTD method is used in this research, which is described in the next section.

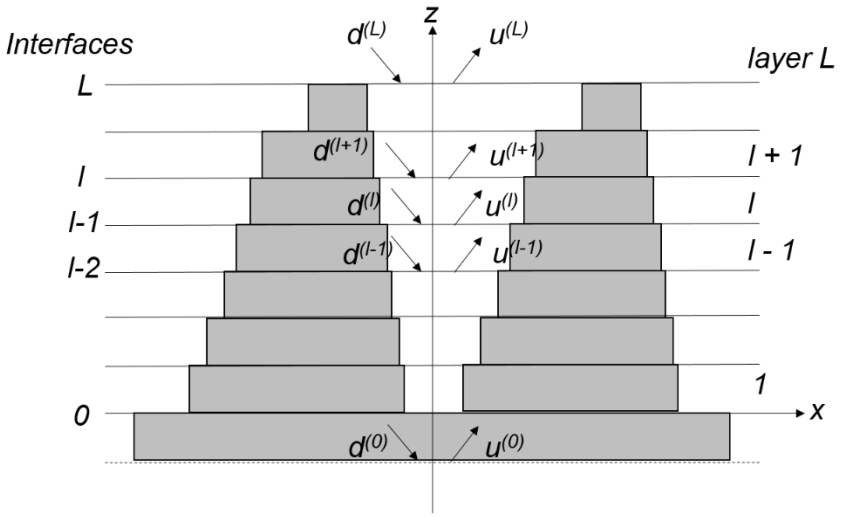

Figure 2.15 Optional shape structure model in RCWA simulation

2.4.4 Finite-difference-time-domain (FDTD) method

In this section, FDTD method is explained [98,99]. The FDTD method is used for solving Maxwell's equation using a finite-difference time and special grids. The flow chart of the FDTD calculation is shown in Fig.2.16.

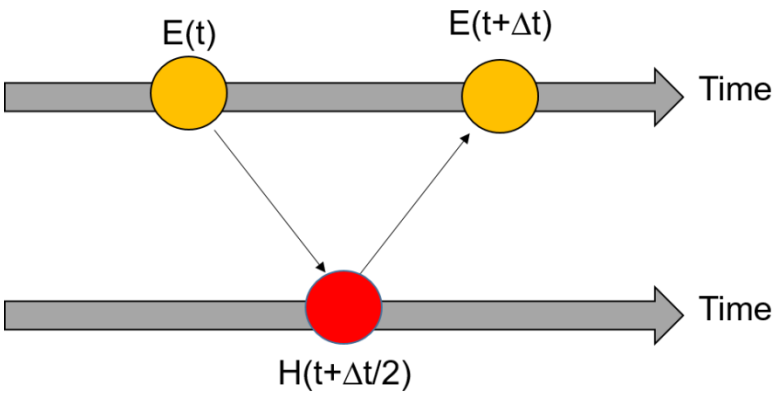

Figure 2.16 Flow chart of FDTD method

The simulation region is divided into rectangular cells and time is broken up into incremental time steps Δt. Now, the electric and magnetic field of light are a function of time and space. At first, the electric field component E at a specific time t is calculated in the divided rectangular cell. Next, the magnetic field component H at $t + \Delta t / 2$ is calculated using the electric field component at t. Finally, the electricfield component at $t + \Delta t$ is also calculated using the magnetic field component at $t + \Delta t / 2$. Repeating this calculation cycle in each rectangular cell, we can obtain the electromagnetic response of the structure in the simulation region. The advantage of FDTD method is providing the intermediate states of the filed in the SWG, and the transition of the filed for time can be observed. This advantages is very suitable and useful for investigation of the detail of the eigenmode physical behavior. Thus, FDTD method was used in this study.

2.4.4.1 Perfect matched layer (PML) boundary condition

A perfect matched layer (PML) was employed as boundary condition at edge of calculation region of FDTD simulation. The diagram of PML is shown in Fig. 2.17 [100].

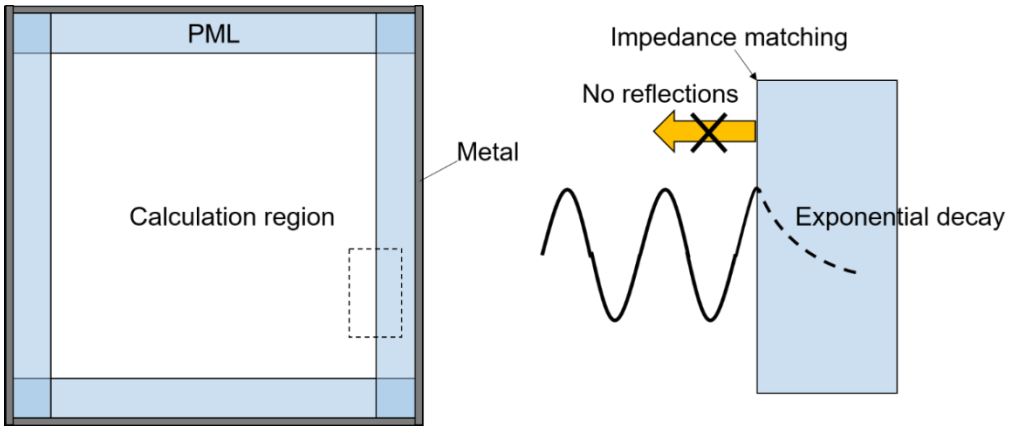

Fig. 2.17 Behavior of light wave in the PML

The impedance of PML was matched at the interface between the calculation region and PML, and the reflected light was not occurred at this interface. The emerging light into PML of the filed amplitude was exponentially decreased and reflected at the metal placed at the back of PML. The reflected light returned to the calculation region. The intensity of the retuned light is very small, so the retuned light has no effect on the filed in the calculation region. Generally, PML is composed by some layers so that the impedance is matched.

2.4.4.2 Convergence of FDTD method

The rigor and convergence of solution using FDTD method depend on the special grid size (Δx, Δy, Δz) and the interval time (Δt). To guarantee the rigor and the convergence, the special grid and interval time are taken small, in which the electromagnetic filed is nearly unchanged with the change of the space and time. The rigor of the solution required one tenth or more of the minimum wavelength. This condition is

$$\Delta x, \Delta y, \Delta z \le \lambda_{\min} / 10 \sim . \tag{2.31}$$

In addition, smaller grid size is required in calculation containing high refractive index or lossy materials.

On the other hand, Courant condition must be satisfied to guarantee the convergence of the solution. Courant condition is given by [99]

$$\Delta t = \frac{1}{c\sqrt{\frac{1}{\Delta x^2} + \frac{1}{\Delta y^2} + \frac{1}{\Delta z^2}}} \tag{2.32}$$

where c is the light speed at vacuum. The grid size and the interval time of FDTD calculations in the thesis satisfy Eq. (2.31) and (2.32). This condition is satisfied in all FDTD calculations in this work.

2.5 Conclusion

In this chapter, the fundamental propagation characteristics of the eigenmode within the SWG was described. In section 2.2, wave equation was derived from Maxwell's equations to see the physical behavior of the eigenmode, and explained that the behavior strongly depend on the propagation constant. In section 2.3, the model for treating the eigenmode in the SWG was described to found the eigenmode exited inside the SWG in the various situation. At first, SPR model, which explains the coupling of the light with the collective oscillation of electrons, was represented. Secondly, we described GMR model treating the guided leaky mode was described. And then, Bloch mode model, in which the mode due to the refractive index distribution was considered, was shown. In section 2.4, the calculation method for the electromagnetic filed distribution, such as EMT, MIM, RCWA, and FDTD method were described, and the advantage and disadvantages of each method were also discussed.

Chapter 3: Theoretical analysis of SWG for various applications in UV and VIS region

3.1 Introduction

To develop the UV~VIS photonic devices based on the interaction between a light wave and Bloch eigenmode wave in the SWG, mentioned in the chapter 1, the propagation property of the eigenmode inside the SWG was determined at UV~VIS region. Bloch-mode model was performed to estimate the propagation property of eiegenmode in IR wavelength region, described in section 2.3.3. However, the photon absorption in shorter wavelength, especially UV wavelength region, becomes larger than that in IR region, and the large absorption affect the eigenmode state, as described in section 3.2. Thus, the determination of the eigenmode propagation property considering of the effect of the photon absorption is essential for the design of SWG UV ~ VIS region. In chapter 3, the electromagnetic response of a SWG in UV wavelength region were examined. In section 3.2, the wavenumber dispersion relation was derived to reveal the propagation property of the eigenmode in the UV wavelength region. The electromagnetic fleld distribution is investigated by FDTD method, and the light propagation mechanism in the SWG was discussed to provide the design concept of SWG for the UV integration devices.

3.2 Discussion for propagation property of the SWG in UV region

The interaction between the eigenmode and the incident light dominates the electromagnetic response of the SWG structure. The Bloch-mode model was employed for investigation of the propagation mechanism in the SWG, because the SPR or GMR can be excited in the case of the SWG described in this chapter [80,82,101] . However, the Bloch-mode model mentioned in the chapter 2 is only for SWG, which has no photon absorption, namely only real part of the refractive index of the grating material. On the other hand, in shorter wavelength region, the imaginary part is larger than that in IR region, the effect of the imaginary part on the eigenmode state cannot be negligible. Note that some of the eigenmode energy disappears upon light propagation in the SWG, provided the SWG material has a light absorption capability. In this case, the eigenmode possesses complex wavenumber. The wavenumber of the eigemode k_a, k_s, and β_m (these were shown in Fig. 2.8) were expanded to the complex wavenumbers in order to reveal the propagation property of the eigemode in UV wavelength region. In the model, normal incident light was assumed, with a monochromatic plane wave having $\lambda = 365$ nm, which was s- or p-polarized. The direction of the electric field vector in the case of s- and p-polarization is parallel and perpendicular to that of the grating shape, respectively. The grating period Λ and the filling factor (defined as the ratio of *s* to Λ) were set to $\Lambda = \lambda/3.6 \text{ and } w/\Lambda = 0.5,$ which were typically used in the wire-grid, respectively. The grating was assumed to have an infinite length in the *y*-direction, because the actual grating length in the *y*-direction is significantly larger than λ. Specifically, the y-direction length of the fabricated SWG mentioned in later chapters is 300 μm, which is 5th-order

larger than the wavelength of UV light, so this assumption is reasonable.

To examine the effects of the real and imaginary parts of each material n_{bar} on the SWG optical characteristics, four grating materials were assumed: Si, Ge, Pt, and Cr, which have various n_{bar} values. The n_{bar} values at $\lambda =$ 365 nm for Si (6.5271 + 2.6672i), Ge (4.0716 + 2.576i), Cr (1.8636 + 2.6793i), and Pt (1.64 + 2.64i) are obtained from previous studies [51, 102, 103]. These four material are used in this analysis for the following reason. The contrast of the real part of refractive index between the grating and the surrounding closely rerated with the excitation of the eigennmode [29-32]. In point of view of the excitation of mode, extreme low refractive index contrast causes the difficulty of the light control by using the eigenmode. Hence, the four materials were employed in this analysis not Al, which is typically used for wire-grid polarizer. In this model, the relation of dispersion between complex k_a and k_s is obtained by considering the boundary continuity of the electromagnetic field in the SWG. The relation of dispersion for the p-polarization is

$$n_{bar}^{-2}(k_{s,m}^{'}+ik_{s,m}^{''})\tan\{(k_{s,m}^{'}+ik_{s,m}^{''})s/2\} = -(k_{a,m}^{'}+ik_{a,m}^{''})\tan\{(k_{s,m}^{'}+ik_{s,m}^{''})a/2\} \quad (3.1)$$

The relationship between k_s or k_a and β_m is

$$\left(\frac{2\pi}{\lambda}\right)^2-(k_{a,m}^{'}+ik_{a,m}^{''})^2=\left(\frac{2\pi n_{bar}}{\lambda}\right)^2-(k_{a,m}^{'}+ik_{a,m}^{''})^2=(\beta_m^{'}-i\beta_m^{''}) \quad (3.2)$$

where the superscription ’ and ” indicate the real and the imaginary part of wavenumber of eigenmode. A sign of the imaginary part of these wavenumber is chosen to converge and given correct physical behavior. For the dispersion relation of *s*-polarization, the n_{bar} term in Eq. (3.2) is replaced with 1 [47]. The solutions of Eq. (3.1) and (3.2) indicate that the energy of the incident light wave can be transferred to the eigenmode wave. Further, the solutions in ascending order correspond to *m*. For example, the first solution of Eq. (3.1) corresponds to the 1st-order eigenmode (*m* = 1).

Figure 3.1 shows the real and the imaginary values of β_m obtained by solving Eq. (3.1) and (3.2), for the various examined materials. When β_m is a complex number, the eigenmode propagates along the *z*-direction with the decay of the light intensity, and we cannot precisely distinguish the propagation and evanescent mode, and considered up to 2nd-order eigenmode (*m* = 2), because the amplitude of the higher-order eigenmodes than 2nd-order rapidly decrease and typically became very low and have no contribution for energy propagation in the SWG [47].

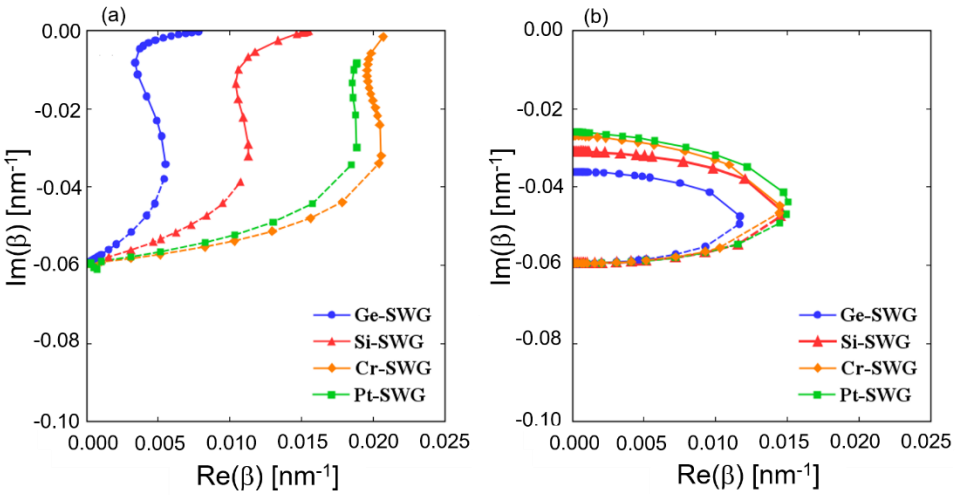

Figure 3.1 Real and imaginary parts of propagation constant for (a) p- and (b) s-polarized eigenmodes.

The solid and dashed curves correspond to the first- and second-order eigenmodes, respectively. When only the real or the imaginary part of Eq. (3.1) and (3.2) was satisfied, we consider that the eigenmode can possess the wavenumber vector according to the following rationale. The real and imaginary parts of Eq. (3.1) and (3.2) indicate the phase matching and the decreasing of the amplitude matching condition, respectively. When the grating has a light absorption capability, the part of the energy of the incident light dissipates into the grating material as joule loss. This decreases the eigenmode lifetime, and the amplitude and the phase of the mode cannot be determined simultaneously. The uncertainty between the amplitude and the phase broadens the eigenmode states, which leads to the relaxation of the resonance condition. Thus, the mode can possess the complex wave number, which satisfies only the real or the imaginary part of Eq. (3.1) and (3.2).

For p-polarization, the dispersion relation means that the absolute values of the imaginary parts of the 1st- and 2nd-mode propagation constants, namely, the propagation loss, are lower for a high-refractive-index SWG (with Si or Ge, labeled Si- or Ge-SWG, respectively) than that for a low-refractive-index SWG (the Pt- or Cr-SWG), as shown in Fig. 3.1(a). In general, the imaginary part of the material n_{bar} is directly related to the light absorption in the material. This causes energy loss of the incident wave, and this loss generally increases as the absolute value of the imaginary part of the n_{bar} is increased. As a result, the propagation loss and the value of the n_{bar} imaginary component are mutually related. In contrast, the result shown in Fig. 3.1(a) indicates that the absorption coefficient is not directly related to the propagation loss, and the propagation loss in the high-refractive-index SWGs can become lower than that in the low-refractive-index SWGs in spite of the large absorption coefficient. The reason for this

behavior is explained as follows. The eigenmode is defined as a solution of Maxwell's equations for the periodic n_{bar} distribution, and the eigenmode must satisfy the electromagnetic boundary condition inside the SWG structure. The eigenmode state and the excitation conditions are strongly dependent on the geometric shape. Therefore, the propagation loss in the SWG is not only determined by the material properties, but also by the geometry. According to the dispersion analysis, the eigenmodes within the Ge- and Si-SWGs are tuned to yield high p-polarization transmittance by controlling the SWG geometry, despite the large absorption coefficient. These types of SWGs are, therefore, suitable for maintaining high transmittance throughout the structure.

The solutions to Eq. (3.1) for an s-polarized eigenmode also are shown in Fig. 3.1(b). This figure shows that the s-polarization propagation loss is significantly larger than that of the p-polarization case for all examined gratings. The s-polarization transmittance through the Si- and Ge-SWGs is lower than that through the Pt- and Cr-SWGs, because the absolute value of the imaginary part of the 1st-order mode propagation constant in the Si- and Ge-SWG is larger than that for the other gratings. The difference in the eigenmode characteristics between the p- and s-polarization are attributed to the difference in the electric field direction between the two orthogonal polarization states, because the eigenmode state is strongly dependent on the boundary condition and the structure geometry for the electric field of the light. As a result, the dispersion relation suggests that a high-refractive-index material is suitable for achieving high polarization selectivity and high transmittance in the UV wavelength region.

To evaluate the precise optical characteristics of the SWG, the electromagnetic field distribution was calculated using the FDTD method. The FDTD calculation model is shown in Fig 3.2. The square region surrounded by broken lines is determined as the

calculation region. PML was used as the boundary for z-directions. The number of PMLs was 20 layers. The periodic boundary condition was employed for x-direction, the periodicity of the SWG was assumed infinite length. The vertical and lateral sizes of the calculation region were 715 nm and 405 nm, respectively. The calculation region was divided into a 2 nm × 2 nm rectangular cell. The calculation time step was 3.3×10^{-18} s. These discretizing satisfy the Courant condition as show in Eq. (2.32). In this model, an SWG structure was arranged in air. The p- or s-polarized incident plane wave with the wavelength λ of 365 nm was propagated through the SWG, and the transmittance through the SWG was calculated at the observation plane.

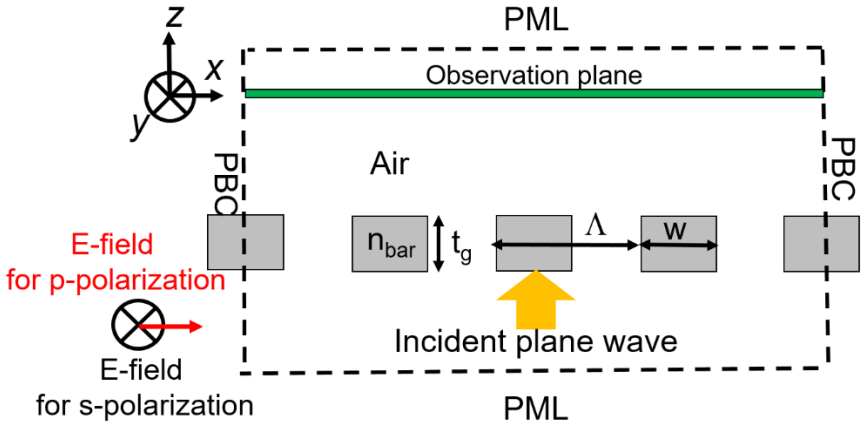

Figure 3.2 Cross-section of the FDTD calculation model.

The transmittance calculated through the SWG structure as a function of t_g was shown in Fig. 3.3. Note that the transmittance converges to 100% at $t_g = 0$. The reason of the convergence is explained as follows. In the case of $t_g = 0$, the light propagates in free space. The eigenmode due to the SWG starts propagating energy with increasing

t_g. Therefore, the transmittance varies rapidly around t_g = 0. The transmittance of p-polarization was significantly larger than that of the s-polarization for all SWG cases and oscillated with increased t_g. In the region up to t_g = 30 nm, the transmittance through the Si- and Ge-SWGs was higher than that through the low-refractive-index SWGs. In the region of t_g = 50–100 nm, the transmittance through the high-refractive-index SWGs was lower than that through the low-refractive-index SWGs. On the other hand, the electromagnetic response for the s-polarization varied significantly from that for the p-polarization case. That is, the s-polarization transmittance significantly and monotonically decreased with increased t_g, and became significantly smaller than that obtained for the p-polarization case. Overall, the polarization ratio (defined as the transmittance ratio of the p- to s-polarization) increases with increasing t_g, and the Si-SWG polarization ratio is the highest of all the examined gratings, at more than 9×10^4 for t_g = 100 nm, while maintaining ~40% transmittance.

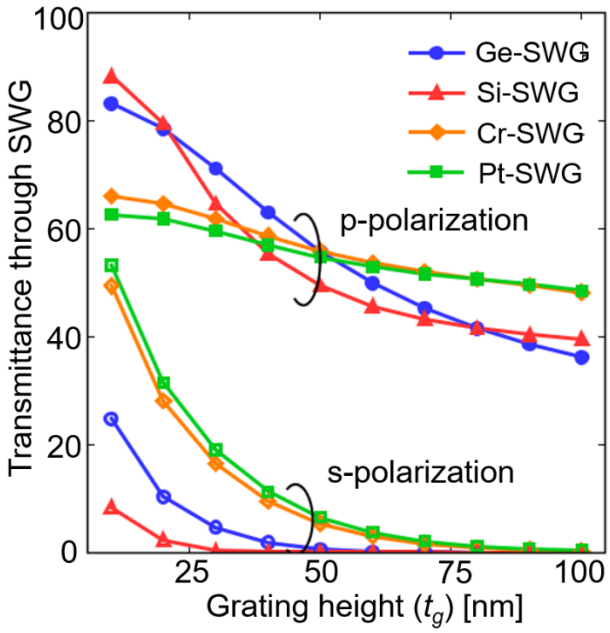

Fig. 3.3 Calculation of transmittance through SWG as a function of grating height (t_g)

using the FDTD method. The filled and open symbols indicate the transmittance of the p- and s-polarization, respectively

These results suggest that both high selectivity for polarization and high transmittance can be achieved simultaneously in the UV wavelength region using a Si-SWG. The tendency of the optical characteristics determined via the FDTD method agrees with that obtained by considering the dispersion relation.

In order to interpret and discuss the physical characteristics of the eigenmode, the FDTD calculation results were compared with those yielded by the dispersion relation. For p-polarization, the FDTD calculation results indicate good agreement with the prediction of dispersion relation in the region up to t_g = 30 nm. For t_g = 50–100 nm, however, the transmittance through the Pt- and Cr-SWGs is higher than that through the Si- and Ge-SWGs, which is contrary to the prediction of dispersion relation. Considering the s-polarization, the transmittance through the Ge-SWG is higher than that for the Si-SWG. Moreover, this result disagrees with the prediction of dispersion relation. These discrepancies occur only for the high-refractive-index, such Si- and Ge-SWGs.

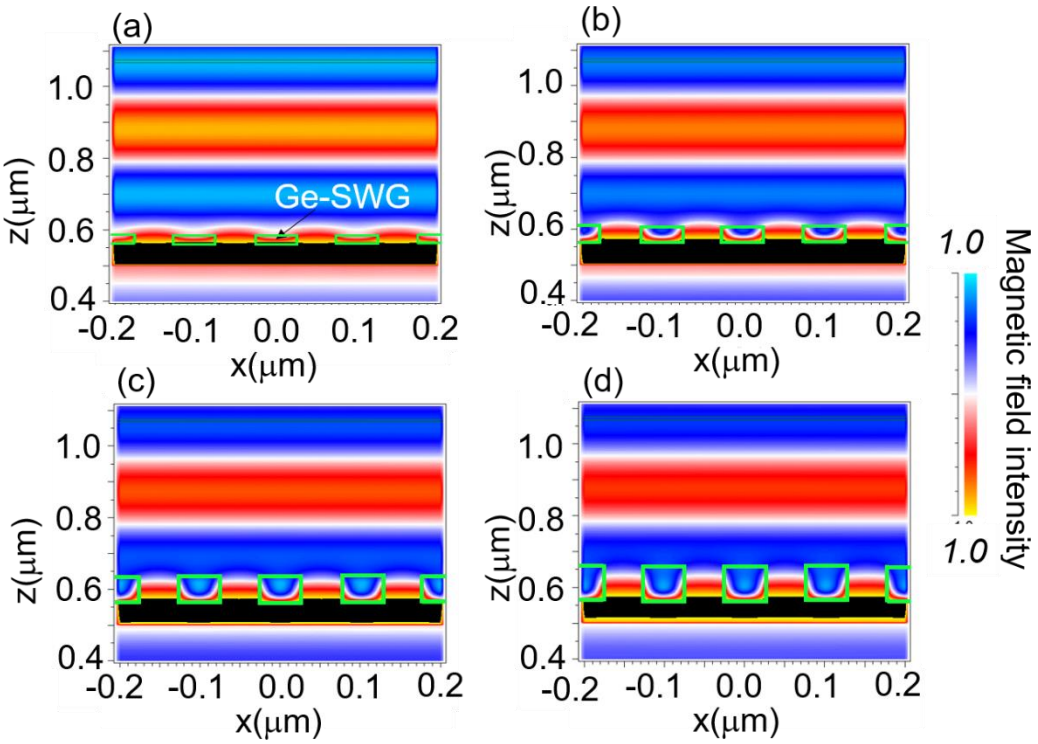

Fig. 3.4 Dependence of p-polarized eigenmode magnetic field distribution within Ge-SWG on t_g, for t_g = (a) 25, (b) 50, (c) 75, and (d) 100 nm

In order to elucidate the origin of this disagreement, the dependence of the p-polarized eigenmode magnetic field distribution in the Ge-SWG on t_g was determined, as shown in Fig. 3.4. The magnetic field for p-polarized light prefer to electrical field for this analysis, because the magnetic field for p-polarization is the continuous at the interface between the grating and the air-gap. This Ge-SWG was selected because it exhibits significant variation in the transmittance of p-polarization with increasing t_g. The green-squares in Fig. 3.4 indicate the highly refractive region of the grating. In Fig.3.4, the field intensity of the blue region in the green-squares increased with increasing t_g, whereas the red region remained almost unchanged. This indicates that the field distribution of the eigenmode varied with increasing t_g. Therefore, one of the origins of

the above discrepancies is attributed to the transformation of the incident light energy into the higher-order eigenmode, because the energy transformation into the higher-order mode in a high-refractive-index SWG can become larger than that in the low-refractive-index SWG [47]. We consider up to the second higher order mode, because the higher order mode than the second significantly decreases with propagation. To confirm the effect of the higher-order mode on the SWG optical characteristics, we examined the transmittance through the Ge-SWG for various weightings of the 1st- and 2nd-order eigenmodes. The transmittance was evaluated by the electric field of the 1st- and 2nd-order eigenmodes and the ratio of the incident light intensity to the transmitted intensity was determined. To examine the dependence of the transmittance decay on the ratio of each mode weight, we considered only the imaginary part of β_m. Moreover, the difference of the real part of β_m causes the phase difference between the eigenmodes when the modes pass through the SWG. The difference of the phase influences on the transmittance through the SWG. This effect of the real part of β_m on the mode phase was considered for calculating the mode weight.

The 1st- and 2nd-order modes with the imaginary components $\beta_1\Lambda = -0.4709$ and $\beta_2\Lambda = -6.014$ were used for the investigation, with the above values being obtained from the relation of dispersion. The envelope of the total electromagnetic field within the SWG was expressed in terms of the superposition of the excited modes, i.e., $A_1\exp(-0.4709t_g/\Lambda) + A_2\exp(-6.014t_g/\Lambda)$, where A_1 and A_2 are the first- and second-order mode weights, respectively.

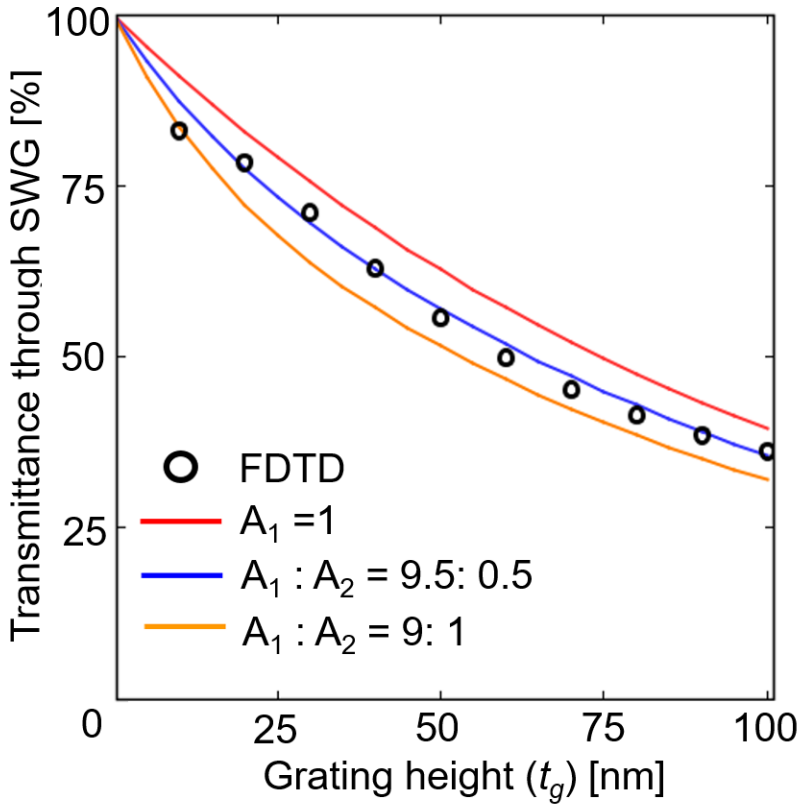

Figure 3.5 Dependence of p-polarization transmittance through Ge-SWG as a function of t_g for various 1st- and 2nd-order mode weights

Figure 3.5 shows the dependence of the transmittance through the Ge-SWG as a function of t_g for various first- and second-order mode weights. This figure demonstrates that the optical characteristics agree with those yielded by the FDTD calculation when the weights of the first- and second-order eigenmodes are adjusted with increasing t_g. This agreement is explained by considering the modulation of n_{bar} with increasing t_g. As Si- and Ge-SWGs have higher n_{bar} values than the other examined substances, the degree of the n_{bar} modulation for these materials increases with increased t_g. The oscillator strength of each mode is modified by the variety of the n_{bar} modulation, and the transformation of the light energy into the higher-order mode is changed. Thus, the weight of each eigenmode varies with increasing t_g. The propagation

loss for the higher-order modes is larger than that for the lower-order mode as shown in Fig 3.1. As a result, the transmittance through the SWG is influenced by the changes in the transformation of photon energy into higher-order eigenmode. By referring previous studies, we verified the estimated weight of each mode. The weight was calculated by

$$A_{n,m} = \frac{\int_0^{\Lambda} \left| h_{y,m}^{in}(x) \right|^2 dx}{\left| \int_0^{\Lambda} \frac{1}{r^2(x)} h_{y,n}^{out}(x) h_{y,m}^{in}(x) dx \right|} \tag{3.3}$$

The symbol *r(x)* denotes the refractive index and 1 in air-gap of the SWG. In the grating bar, the *r(x)* is n_{bar}, where n = 0, 1, 2… denote the diffraction order outside the SWG. In the SWG, only the 0th diffraction (n = 0) propagates the energy of the light. The symbols $h_{y,n}^{out}(x)$ and $h_{y,n}^{in}(x)$ are lateral magnetic fields of the profile inside and outside the SWG and are obtained from previous studies [46]. The calculated mode weights of 1st and 2nd were about 9.55 and 0.45, respectively. These calculated mode weights is agree with our estimated mode weights.

In device design in UV wavelength region, the photon absorption of the material be traditionally avoided to decrease the loss. This restricts the range of the design of the SWG and of the application. The founded the propagation characteristics suggest that the transmittance can be maintained, regardless of the large photon absorption. This approach provides new insight into the SWG design for UV light control and broadens the feasibility of development UV photonic device without the significantly decreasing of the light intensity. In addition, the design concept is also applied to the other wavelength

region, in which the light are aborted in the material.

3.3 Conclusions

In this Chapter 3, the physical behavior of the eigenmode in UV wavelength region, in which the SWG material has the photon absorption, has been theoretically investigated by using Bloch-mode model. The dispersion relation of the wavenumber was derived to investigate the propagation property of eigenmode in UV region. This dispersion relation shows that the eigenmode state broaden due to decreasing the lifetime by the imaginary component and the propagation property of the eigenmode is significantly difference from that without the imaginary part of n_{bar}. The electromagnetic filed distribution in the structure is calculated by FDTD method to discussed and reveal the propagation mechanism inside the SWG, and the new design concept of the SWG can be successfully provided for the integration devices in the shorter wavelength region.

Chapter 4: A polarized GaN-based UV-LED with AlGaN-SWG

4.1 Introduction

In the previous chapter 4, high transmittance and high polarization selectivity were achieved in UV wavelength region by utilizing the egenmode in the SWG. In chapter 4, the polarized GaN-based UV-LED was developed applying the SWG, and the emission characteristics of the UV-LED with AlGaN-SWG was discussed. AlGaN was employed as the SWG material due to the high refractive index value. At first, the fabrication of the SWG on the surface of the LED was described in section 4.2. In the section 4.3, the electroluminescence emission spectra (EL) was discussed by the theoretical consideration of the eigenmodes resulting from the spatial periodicity of the refractive index in the SWG region.

4.2 Fabrication of the SWG on the UV-LED surface

The GaN based UV-LED samples on a *c*-plane sapphire substrate by a metal organic chemical vapor deposition technique were used in this study. The UV-LED structure has a 100-nm-thick p-type GaN, p-type AlGaN layer, AlInGaN/AlGaN multiquantum wells, and n-type AlGaN and n-type GaN layers on an undoped GaN layer. The emission spectral peak was observed around the wavelength of 365nm. The LED was annealed at 800 C° to activate the p-type GaN. The SWG structure was fabricated on the UV-LED by electron beam (EB) lithography and inductive coupled plasma (ICP) etching technique.

This fabrication process is as follows and is shown in Fig. 4.1. To clean the

surface of the LED, the sample was washed by pure water, acetone and methanol to clean the surface. The ultrasonic cleaning with 100 kHz is done by pure water, acetone, and methanol. Each cleaning time is 3 min, and repeated this process 5 times.

After the cleaning of the sample surface, EB-resist (ZEP-520A: Zeon) diluted with anisole to 1 : 1 was spin-coated onto the surface of the LED at 300 rpm and 3000 rpm for 3 s and 90 s. The grating pattern, which has a 200 nm pitch and a grating bar width of 140 nm, was drawn on top of the UV-LED using electron beams lithography equipment (ELS7500 : Elionix) with an acceleration voltage of 50 keV. The beam current and dose time of electron were 100 pA and 0.38 μs, respectively. The base pressure of EB equipment was 1.8×10^{-5} Pa by rotary pump (RP) and turbo molecular pump (TMP). The patterned resist was developed (ZED-50N: Zeon) at 20 C° for 15 s. After that, a 50-nm Ni-film used as the mask for ICP etching was evaporated by EB. The vacuum pressure in the EB evaporation chamber is 2.67×10^{-4} Pa. The evaporation rate was about 0.05 nm/s. The resist film was removed by dimethyl sulfoxide at 70 C° for 2 min. Next, the patterned sample was etched by using inductive coupled plasma (ICP). In the ICP etching process, $SiCl_4$, Cl_2 gases were used. The ICP etching conditions is summarized in table 4.1. The Ni-film was removed by using HF aqua after the ICP etching process. Finally, an Au/Ni p-contact film with a thickness of 20 nm was evaporated as an electrode, and the sample was annealed to activate the accepter in the p-type GaN layer. The Au-film and the Ni-film were fabricated by resistance heating and EB evaporation, respectively. The deposition speed of both films were about 0.05 nm/s.

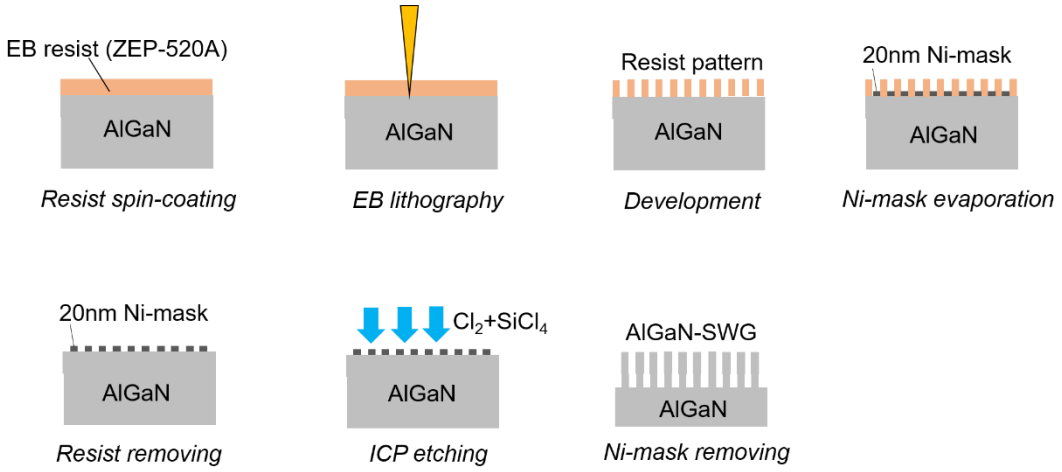

Figure 4.1 Fabrication processes of the SWG on the UV-LED

Table 4.1 ICP etching condition for fabrication

Gas	ICP power [W]	Bias [W]	Flow rate [SCCM]	Pressure [Pa]	Etching time [s]
$SiCl_4$	100	50	4	0.3	10
Cl_2	50	50	4	0.3	180

The grating area size was 0.9 x 0.9 mm^2. The 45° tilted bird view of the scanning electron beam microscope (SEM) images of the SWG and shown in Fig. 4.2(a) and (b). The fabricated grating pitch and thickness were 200 and 150nm, respectively. In addition, the fabricated SWG has uniform period and the grating thickness as shown in Fig. 4.2(b).

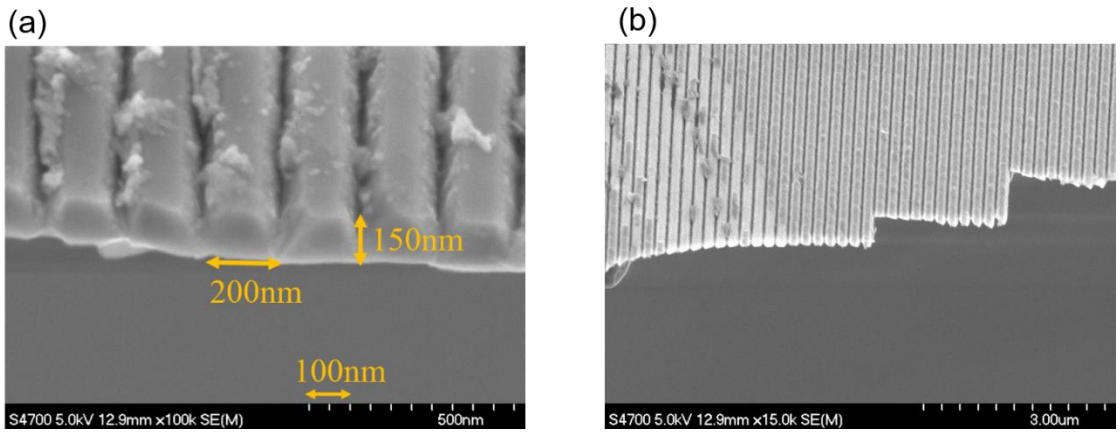

Figure 4.2 Cross-sectional view of the SWG fabricated on the top of conventional c-plane GaN-based UV-LED (a) 100000-, (b) 15000- magnification

4.3 Experimental emission characteristics of UV-LED with SWG

After the fabrication processes of the SWG, the EL spectra of the emission from the UV-LED with the SWG was measured at a forward current of 20 mA (current density 20 mA/mm^2). The measurement system is shown in Fig. 4.3. A dichromatic polarizing

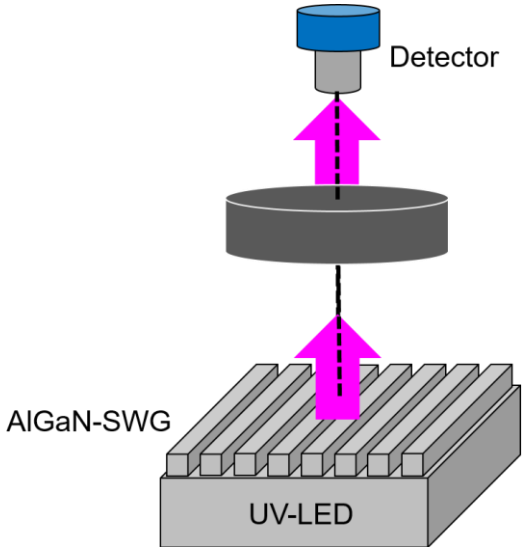

Figure 4.3 Experimental setup of EL emission measurement

plate was placed at the front of the LED sample. The emission intensity from the UV-LED

was detected for p- and s-polarization by rotating the polarizing plate.

The EL emission spectra from the conventional *c*-plane UV-LED without the SWG and that with the SWG were shown in Fig. 4.4 (a) and (b), respectively. The open circles and the filled circles indicate the intensity of s-polarization emission and that of p-polarization, respectively. For the EL spectra from the UV-LED without the SWG shown in Fig. 4.4 (a), a nearly unpolarized emission is observed in the wavelength region from 360 to 400 nm. On the other hand, the spectra from the UV-LED with the SWG show a polarized emission. In particular, the polarization ratio is about 4 at the around 360 nm wavelength region.

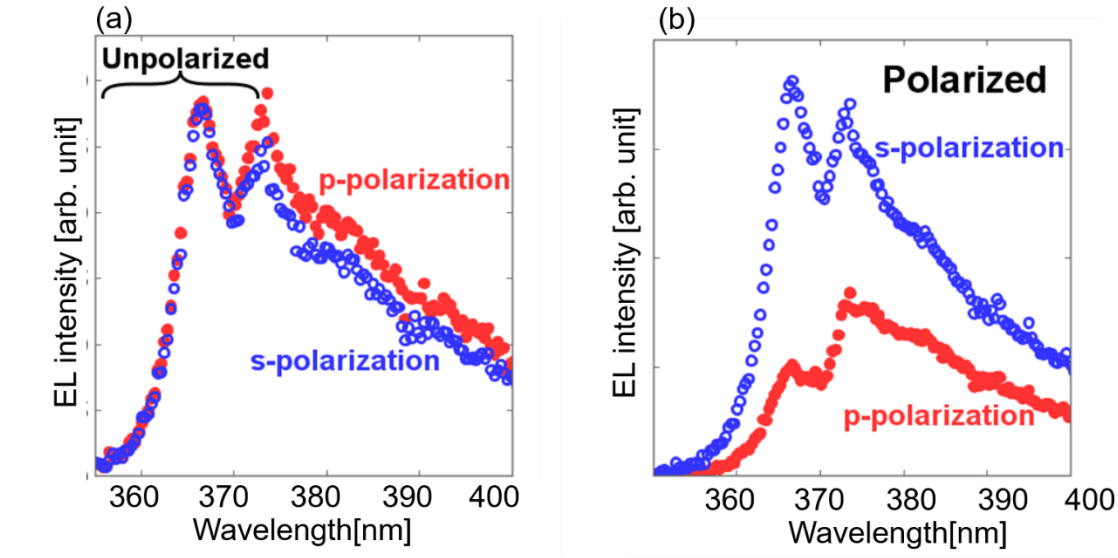

Figure 4.4 Emission spectra from UV-LED: (a) without (b) with the SWG structure at a forward current 20mA

4.4 Discussion of the EL emission spectra

In this section, the EL spectra were discussed by using wavenumber dispersion relation to interpret the physical light behavior of the eigenmode in the SWG. The Bloch-mode model described in the section 2.3.3 was used for the dispersion analysis model. The grating material is assumed to AlGaN, The incident light with the wavelength of 360 nm was normally emerged to the SWG. This model was called the symmetric model in this chapter. The refractive indices of AlGaN (n_{AlGaN}) and air (n_{air}) used in this simulation were 2.47 + 0i and 1 + 0i for the 360 nm wavelength, respectively [104]. In the model, the AlGaN-SWG has a grating thickness t_g = 150 nm and a filling factor of 0.7. The wavenumber dispersion relation between k_a and k_s is shown in Fig. 4.5. In the dispersion relation of the p-polarization, three propagating modes, which are 1st-, 2nd-, and 3rd-orders, were found in the region from the incident wavelength/grating pitch ratio λ/Λ = 1 to 1.07. In the region from λ/Λ = 1.07 to 2, two propagating modes, which are of the 1st- and 2nd-orders, were obtained. The only 1st-order propagating mode existed when the grating pitch became shorter than half of the incident wavelength. For s-polarization, the 3rd-order mode cannot be exited in any grating period. The 2nd- and 1st-order modes were founded in the region from λ/Λ = 1 to 2, and the only 1st-order mode was excited in the shorter period than half of the wavelength.

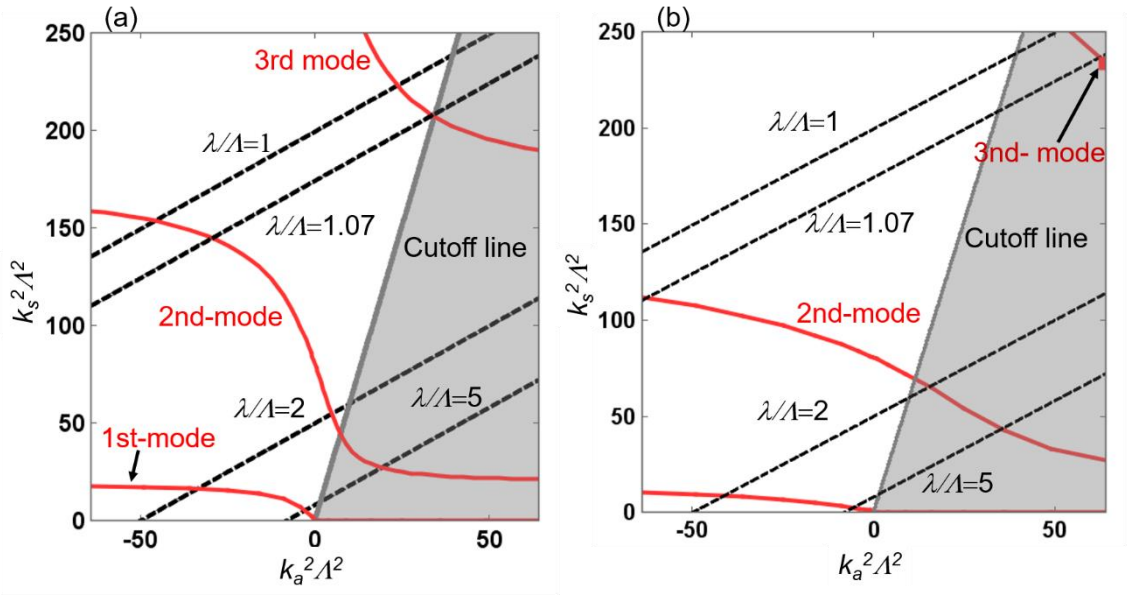

Figure 4.5 Dispersion relation between k_a and k_s in AlGaN-SWG

(a) for p-, (b) for s-polarization.

As described in section 2.3.3, the transmitted light was expressed as the superposition of each propagation eigenmode excited in the SWG. Based on eq. (2.26) in the chapter 2, the cancelation condition cannot be obtained when the only first eigenmode exists in the SWG, and the SWG behavior like uniform film. On the other hand, More than two modes exist, it is very difficult to obtain the cancelation condition. Thus, the transmittance through the SWG became smaller in the region from λ/Λ = 1 to 2, if the 1st- and 2nd-order propagating modes were antiphase and the transmitted light was cancelled. The prediction from the dispersion relation agreed with the experimental results, indicating the polarized emission in the region of λ/Λ = 1.825 to 2.

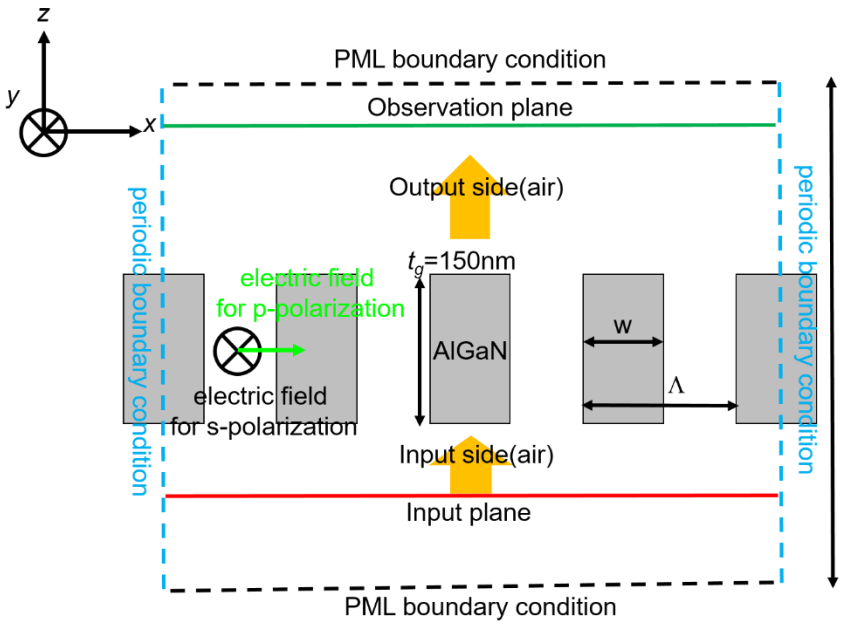

Figure 4.6 Schematic of the symmetric model in field simulation using FDTD method

The electromagnetic field distribution within AlGaN-SWG have been investigated using a FDTD method to clarify the propagation characteristics of the eigenmodes. Figure 4.6 shows the cross-sectional view of the symmetric model for the calculation. The other conditions for calculation was same as that of Fig. 3.2 in chapter 3. The transmitted light intensity was evaluated in the observation plane using the Poynting vector along the *z*-direction through the SWG. Figure 4.7 shows the transmittance through the SWG as a function of λ/Λ.

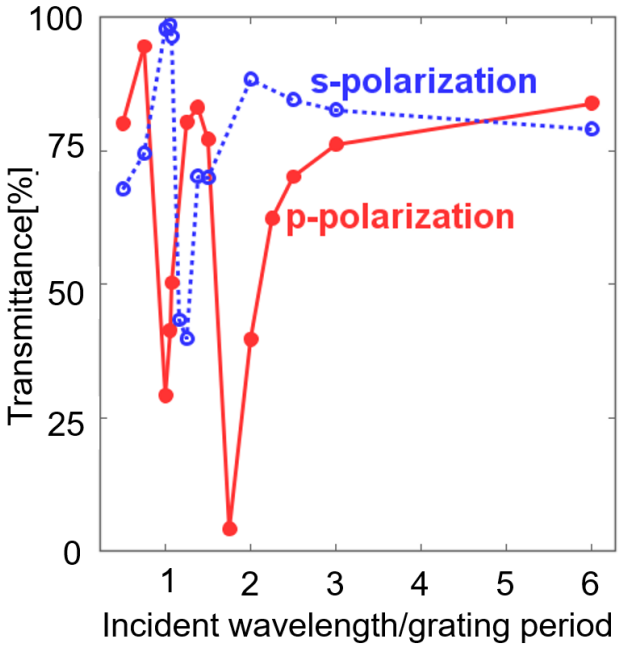

Figure 4.7 Dependence of the transmittance through the SWG on the grating period and polarization

Two dips at λ/Λ = 1 and 1.75 for the transmittance spectrum were found for the p-polarization incident wave. The latter indicates the lowest transmittance (4 %). The transmittance increases in the region from λ/Λ = 2 to 6 and saturates to a constant value (about 80 %). For the s-polarized incident light, the dip in transmittance, which shows the lowest value (about 40 %), is obtained at λ/Λ = 1.4. The highest transmittance for the s-polarization wave is found at λ/Λ = 1 (about 97 %). The magnetic field distribution in the symmetric model at λ/Λ = 1.75 of the p-polarization wave, namely the very low transmittance condition, was shown in Fig. 4.8, in order to understand the propagation property of the eigenmode.

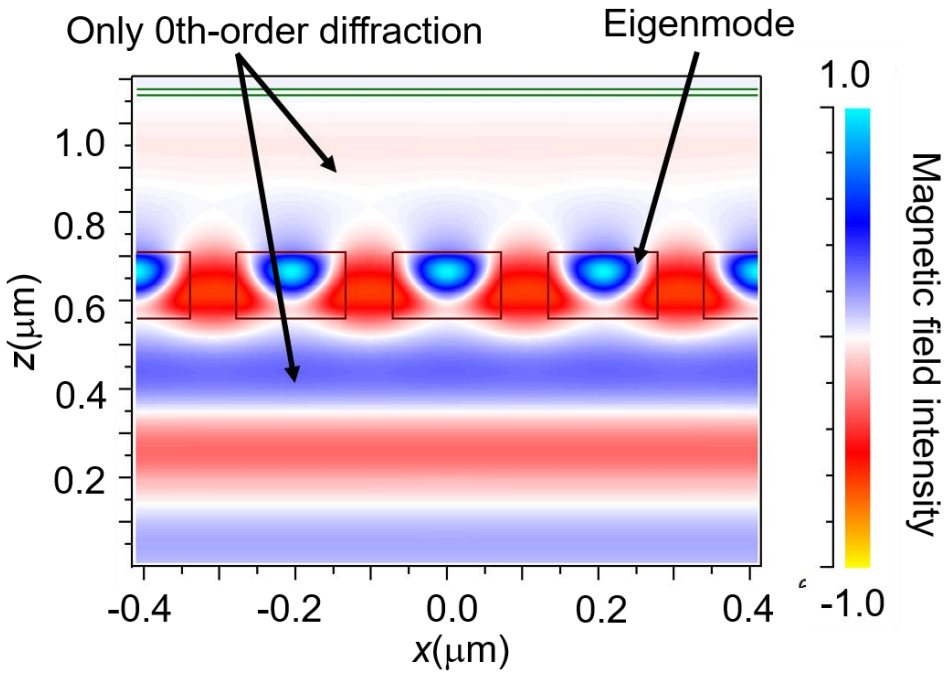

Figure 4.8 Magnetic field distribution within the SWG

for p-polarized eigenmode in FDTD symmetric model at λ/Λ = 1.75.

An eigenmode wave is found in the SWG region, and only the 0th-order diffraction light exists on both the input and out sides due to the subwavelength period. The first- and second-order modes were previously observed to be antiphase at the SWG output plane and were canceled each. As a result, the magnetic field intensity of the transmitted light was very low. The FDTD simulation found that the light behavior differed between the p- and s-polarization waves in the λ/Λ = 1 to 2 region. In particular, the ratio of the transmittance of s-polarization to that of p-polarization was 20 at λ/Λ = 1.7. Although the fabricated grating period was in the region of the large transmittance difference, the experimental polarization ratio did not agree with that in simulation results.

In the actual SWG on top of the LED, the bottom side of the SWG touches the

LED substrate. To apply the SWG structure to polarization control of LED emission, the effect of the substrate on the eigenmode propagation property should be considered, because most of semiconductors have very high refractive index, which decreases the refractive index contrast between SWG and LED. The effect of the high refractive index substrate, such as AlGaN substrate, was evaluated and discussed.

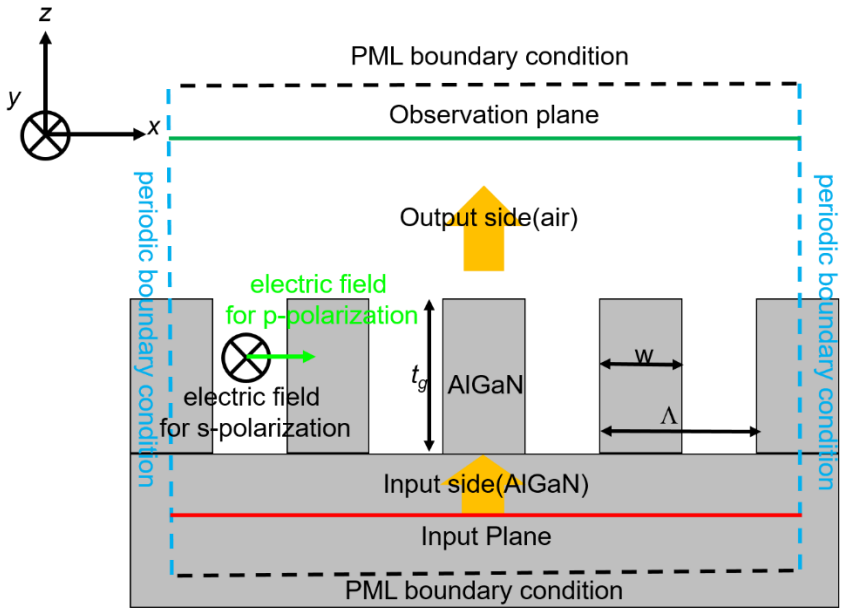

Figure 4.9 Schematic of asymmetric model in FDTD field calculation

The asymmetric FDTD calculation model was shown in Fig. 4.9 in order to investigate the mode behavior in the actual fabricated SWG. The SWG was placed on AlGaN in the input region, and the other conditions for simulation were the same as those of the symmetric model in Fig. 4.6. The transmittance through the SWG in the asymmetric model is shown in Fig. 4.10 as a function of λ/Λ. For the p-polarized light, the dip of transmittance is found, and the lowest transmittance of 20% is obtained at λ/Λ = 1.25. As the grating period becomes shorter in the region from λ/Λ = 2 to 3, the

transmittance increases. In particular, the rapid increasing is obtained at λ/Λ = 2. For the s-polarized light, the dip of transmittance is obtained at λ/Λ = 1.25. The softly increase of the transmittance was observed in the region from λ/Λ = 1.25 to 1.5, and the rapid increase is also found at λ/Λ = 1.55. The difference between the transmittance of the s-polarization wave and that of the p-polarization wave is large in the region of λ/Λ = 1 to 2. The transmitted light intensity ratio (s-polarization/p-polarization) is around 2. These results in the asymmetric model is quite different from that in the symmetric model. The shape dips of the transmittance can be found in the symmetric model, whereas the dips were broadened in the asymmetric model.

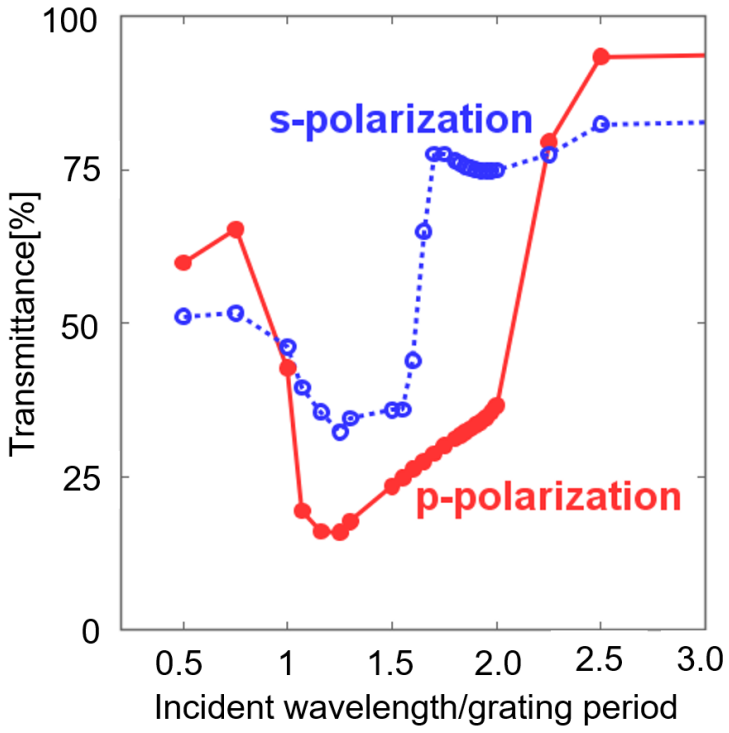

Figure 4.10 Dependence of the SWG transmittance on the grating period and polarization states

In order to investigate this phenomenon and interpret the physical mechanism, the magnetic field distribution in the asymmetric model at λ/Λ = 1.75 is also shown in Fig.4.11. It were found that the modes exist within the SWG. In addition, the magnetic field profile, which differ from that in symmetric model was obtained. Although only the 0th-order diffraction exists on the output side of the SWG, the field pattern showed that the higher-order diffractions (traditional diffractions) occurred at the interface between the SWG bottom and the surface of the LED.

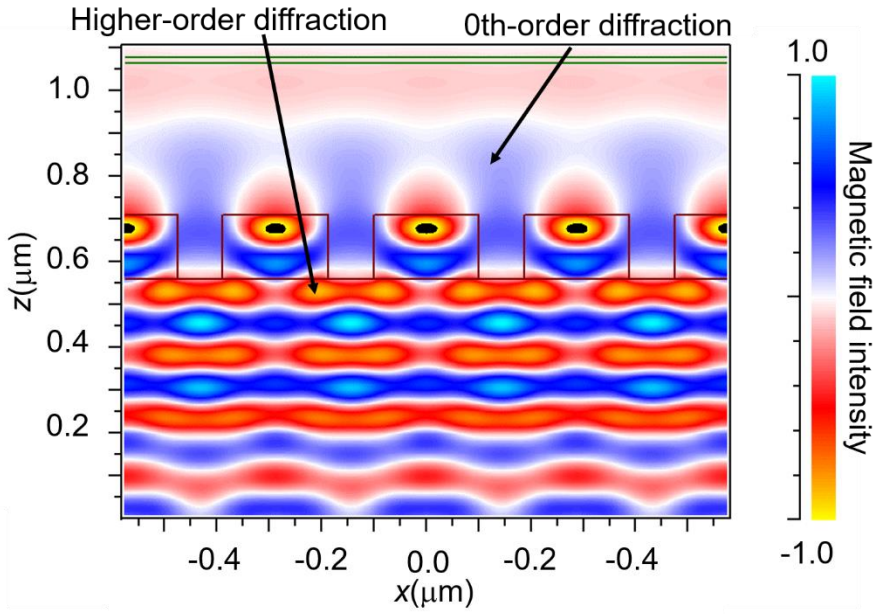

Figure 4.11 Magnetic field distribution of the SWG in the FDTD asymmetric model λ/Λ = 1.75

The fraction of the incident light energy cannot radiate to the outside of the LED and lost by the higher-diffractions, and this lead to a decreasing the polarization ratio and the transmitted light intensity, because the higher-diffractions affect the cancelation of each modes within the SWG. The origin of higher-order diffractions is considered to be the

destruction of the subwavelength condition in the LED substrate. In the substrate, which have refractive index n_{AlGaN}, the wavelength of light become λ / n_{AlGaN} due to the retardation of the phase. The subwavelength condition was districted in the substrate, whereas the condition was kept in the air. The calculation results expect the low refractive index layer inserted into the interface between the LED and the SWG, and the layer improves the polarization characteristic, as described in the chapter 5. Although the effect of the higher-order diffractions at the interface between the LED and the SWG on the polarization characteristics was considered, the experimental polarization ratio is higher than that calculated that in asymmetric model.

The origin of the higher experimental polarization ratio is considered to be the photon absorption due to the poor crystal quality of p-type GaN, because the photon absorption affects the eigenmode propagation property as mentioned in chapter 3. To investigate the effect on the emission characteristics of the UV-LED with the SWG, 100-nm p-type GaN from the top of the SWG was assumed in the asymmetric model as shown in Fig 4.12.

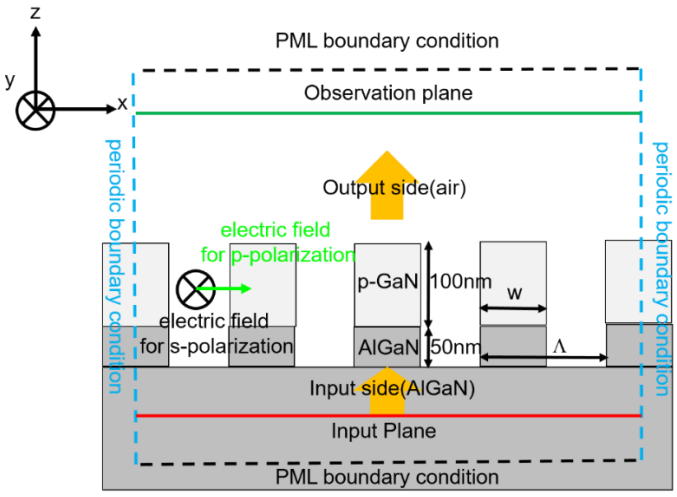

Figure 4.12 FDTD asymmetric model with 100 nm p-type GaN

The refractive index of the p-type GaN ($n_{p\text{-}GaN}$) was used. For example, $n_{p\text{-}GaN}$ = 2.76 + 0.2435i for 360 nm, 2.46+0.065i for 370 nm, 2.45 + 0.0571i for 380 nm, and 2.404 + 0.0166i for 400 nm were used [105]. The transmittance in the asymmetric model with light absorption was about half of that without light absorption, and the tendency of transmittance at λ/Λ was same as that without light absorption. The dependence of the SWG polarization characteristics on the wavelength of the incident light was shown in Fig. 4.13.

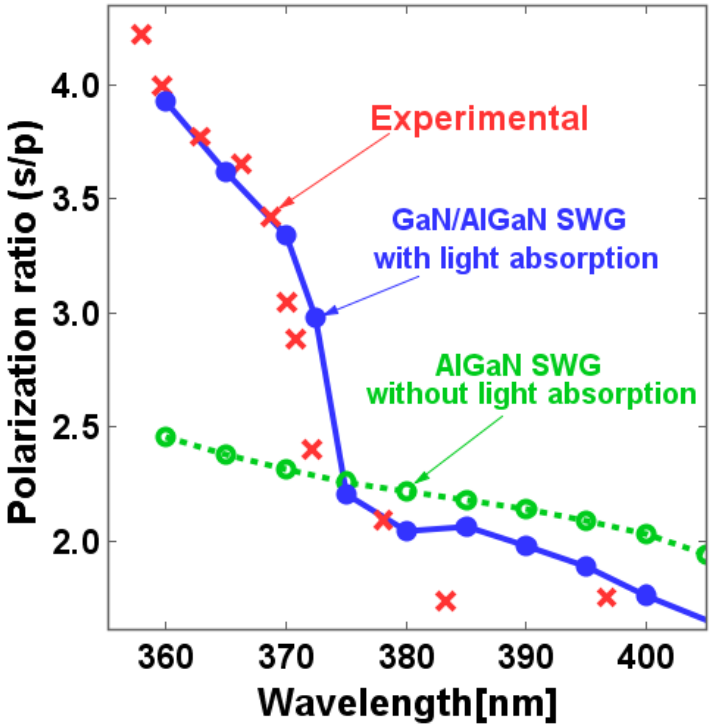

Figure 4.13 Dependence of the SWG polarization characteristics on the incident wavelength

The cross symbols indicate the experimental value of the polarization ratio. The open and filled circle symbols indicate the calculated value of the polarization ratio without and with light absorption, respectively. The experimental results indicate high polarization

ratios of 3 to 4 in the incident light wavelength range from 360 to 370 nm. In the wavelength ranges from 370 to 380 nm and from 380 to 400 nm, the polarization ratio ranges from 2 to 3 and from 1.7 to 2, respectively. The FDTD calculation result without light absorption in *p*-type GaN shows that the polarization is 2.5 at 360 nm and linearly decreases in the incident wavelength region from 360 to 400 nm. On the other hand, the polarization ratio is around 4 in the calculation result with photon absorption in *p*-type GaN for a 365 nm wavelength of the light. With photon absorption, the polarization ratio rapidly decreases in the wavelength region from 360 to 370nm. For light wavelengths longer than 370 nm, the polarization ratio is around 2.

Compared to the results of calculation with and without light absorption, there was a small difference in the region from 375 nm to 400 nm. For light wavelength shorter than 370 nm, the large difference in polarization characteristic between the results of simulations with and without photon absorption was obtained. In the wavelength range from 370 to 400 nm, the simulation result without light absorption agreed with the experimental result, while the large difference in polarization characteristic occurred for wavelengths shorter than 370 nm. The agreement between the result of the simulation with photon absorption and that of the experiment can be explained by considering the effect of complex refractive index p-type GaN on the resonance condition. The low transmission condition, namely the cancelation of each modes, was formed for p-polarization, whereas s-polarization not. Thus, only the p-polarization transmittance through the SWG was affected by the complex refractive index of the grating, because the cancelation condition is differed from that in the case without light absorption.

4.5 Conclusion

In chapter 4, a polarized emission from GaN-based UV-LED was experimentally demonstrated by using the AlGaN-SWG. In section 4.2, the fabrication processes of the SWG on the GaN-based UV-LED was explained. In the section 4.3, the EL spectra of the emission from the LED was shown. The polarization ratio, reached as 4:1 at the UV wavelength of 360 nm. Then, the EL spectra was discussed by the wavenumber dispersion relation and the electromagnetic field distribution, and the discussion suggested the inserting low refractive index layer between SWG and LED substrate significantly improve the polarization characteristic of the emission.

Chapter 5: A highly polarized GaN-based UV-LED using a Si-SWG on a SiO_2 underlayer

5.1 Introduction

In previous chapter 5, the decreasing the polarization ratio caused by the diffraction phenomena due to the destruction of subwavelength condition was found. In chapter 5, the low refractive index underlayer (SiO_2) was inserted between the SWG and the LED in order to suppress the diffractions and to achieve a highly polarized UV-LED with SWG/ SiO_2. In section 5.2, the improvement by inserting the low refractive index layer was estimated by FDTD calculation. In section 5.3, the fabrication processes of SWG/SiO_2 on the GaN-based UV-LED by electron beam lithography. In section 5.4, EL spectra of the emission from the LED was shown and discussed.

5.2 Theoretical investigation of the effect of low refractive index layer inserted between SWG and LED

In this section, the improvement effect of the low refractive index layer between the SWG and the LED on the polarization characteristic of the SWG was theoretically estimated. Si was employed as the high refractive index material of the SWG because Si-SWG can achieve both high polarization selectivity and high transmittance as described in chapter 3.

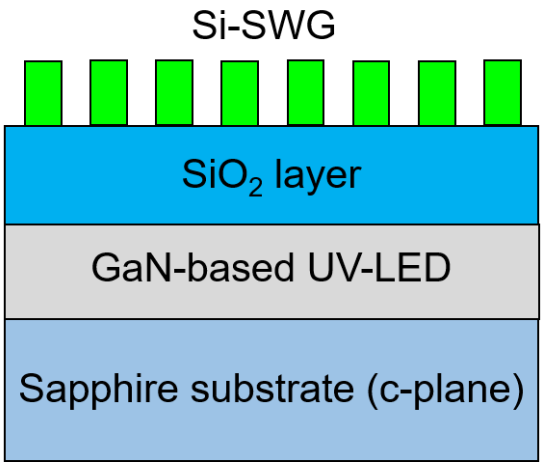

Figure 5.1 Schematic diagram of a UV-LED with a Si-SWG/SiO_2 underlayer structure

A SiO_2 underlayer was inserted between the Si-SWG and the top of the LED to satisfy the subwavelength condition at the interface between GaN substrate and Si-SWG. The schematic diagram of a UV-LED with a Si-SWG/SiO_2 underlayer structure is shown in Fig. 5.1. The electromagnetic field distribution in a Si-SWG/SiO_2 underlayer structure was calculated using the FDTD method to design the SWG for the polarization control of UV-LED.

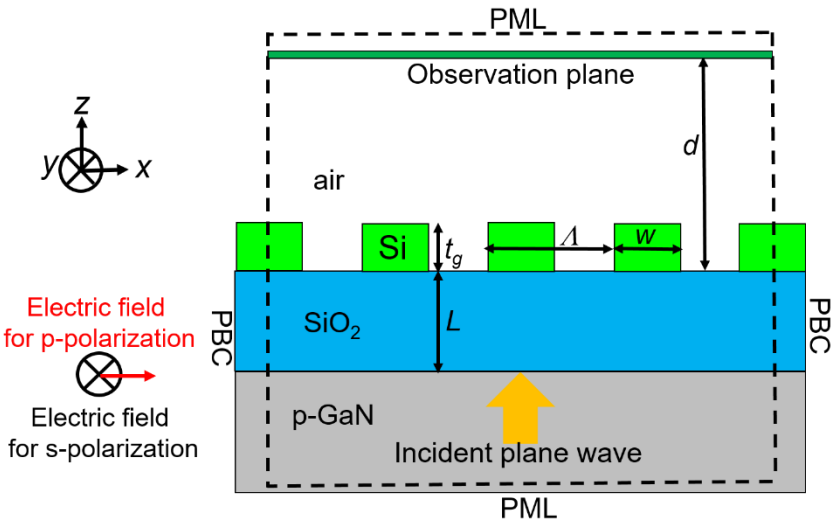

Figure 5.2 Numerical model of UV-LED with a SWG/SiO_2 underlayer

Figure.5.2 shows the numerical model for the calculation of the electromagnetic field distribution using the FDTD method. In this model, SiO_2 underlayer was deposited on the p-type GaN of the surface of the LED. Subsequently, a Si-SWG is arranged on the SiO_2 underlayer. For the model without the SiO_2 underlayer, the Si-SWG is directly arranged on the p-type GaN. The refractive index values at 370 nm for SiO_2 (n_{SiO2} = 1.487 + 0i), p-type GaN (n_{GaN} = 2.46 + 0.065i), and Si (n_{Si} = 3.963 +2.595i) were used [50,105,106]. The refractive index value of Si was assumed the amorphous-Si, because the Si-SWG is fabricated by electron beam evaporation. The thickness of the SiO_2 layer *L* was set to 200 nm. The incident plane wave with a wavelength of 370 nm was either p- or s-polarized. The incident plane wave propagates from *p*-type GaN on the UV-LED surface to air. The transmittance from *p*-type GaN to air was calculated at the observation plane in Fig. 5.2. The distance *d* between the observation plane and SiO_2 layer was 540 nm. The grating thickness was varied, while keeping the grating period and width of the Si-SWG fixed at Λ = 205 nm and *w* = 100 nm.

Figure 5.3 shows that when the grating thickness t_g increases, the transmittance for the p-polarized wave oscillates in both cases, i.e., with and without the SiO_2 underlayer. For t_g = 10-80 nm, the transmittance without the SiO_2 underlayer is higher than that with SiO_2, but when t_g is greater than 80 nm, the transmittance with SiO_2 is higher than that without SiO_2. However, the transmittance for the s-polarized wave simply decreases with the increase of t_g. The transmittance for s-polarization is considerably smaller than that for p-polarization. Also, the transmittance through the SWG with SiO_2 underlayer is lower than that without the layer, which results in high polarization selectivity. The calculation indicates that both a high polarization ratio and high transmittance can be achieved at t_g = 90 nm. A high polarization ratio of 57: 1 (the ratio of the transmittance

for p-polarization to that for s-polarization) is expected, with the transmittance for p-polarization through the structure being maintained at 43 %. The high polarization selectivity and high transmittance in the case of the p-polarized wave cannot be explained by the excitation of surface plasmon, because the surface plasmon excitation condition is not satisfied in our structure [80,101,107].

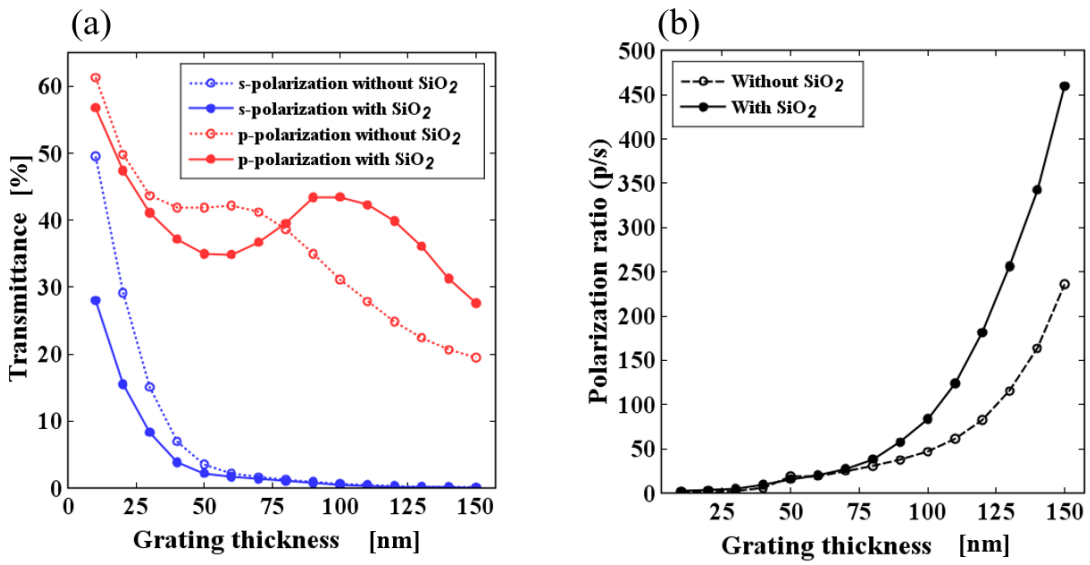

Figure 5.3 (a) Transmittance and (b) polarization ratio for the Si-SWG with and without the SiO_2 underlayer

To clarify the origin of the high polarization selectivity and the drastic increase of the transmittance for p-polarized wave, the magnetic-field distributions at t_g = 90 nm are shown in Fig. 5.4. The magnetic-field distribution for the s-polarized wave in Fig. 5.4 (a) and (c) indicate that the eigenmodes cancel each other at the interface between the Si-SWG and air, and the transmitted field intensities are very low. In contrast, reinforcement of Bloch eigenmodes for p-polarization each other at the interface was obtained, and the intensity of the transmitted field is larger than that of s-polarized filed as shown in Fig. 5.4 (b) and (d). The p- and s-polarized magnetic fields for the UV-LED

without the SiO_2 underlayer also indicate that the wavefront is not planar at the interface between the LED surface and the Si-SWG; a part of the incident wave reflects back to generate a diffraction pattern in the GaN, as displayed in Fig. 5.4 (a) and (b). The coupling between the diffracted plane wave and the incident plane wave affects the energy flow in the SWG, thus leading to deviations in the optical response of the SWG. For the UV-LED with SiO_2 underlayer shown in Fig. 5.4 (c) and (d), the coupling is suppressed because the subwavelength condition is satisfied (namely, the wavelength of light in the SiO_2 > the grating period) owing to the low refractive index value of the SiO_2 layer. The transmitted filed intensity in the UV-LED with SiO_2 underlayer is greater than that without the SiO_2 underlayer, and the SiO_2 underlayer is found to be useful for realizing both high transmittance and a high polarization ratio.

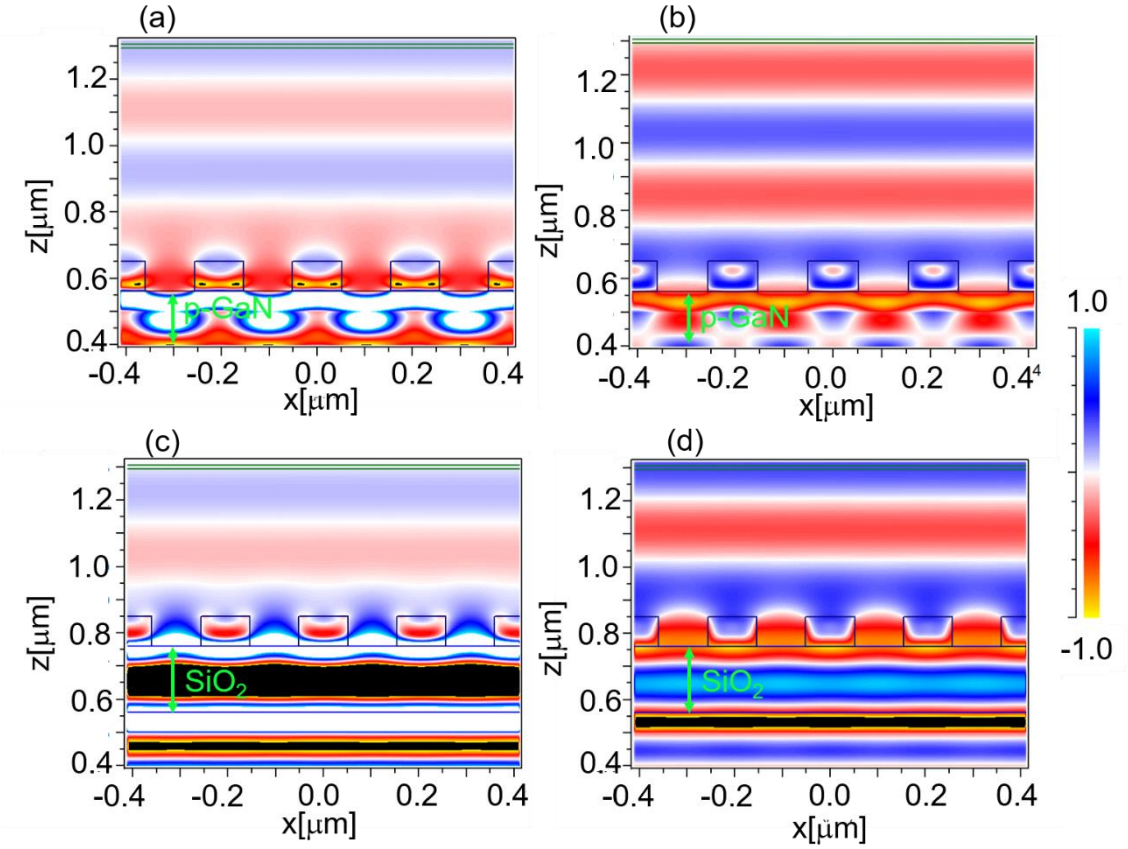

Figure 5.4 Distribution of magnetic field intensity at a given time:

(a) s-polarization without the SiO_2 underlayer

(b) p-polarization without the SiO_2 underlayer

(c) s-polarization with the SiO_2 underlayer (d) p-polarization with SiO_2 underlayer

5.3 Fabrication of Si-SWG/SiO_2 underlayer

The FDTD field calculation revealed that the low refractive index suppress the higher-order diffraction and improve the polarization characteristics of the SWG. In this section, the fabrication processes of Si-SWG/SiO_2-underlayer structure, which achieves both high transmittance and high polarization ratio at 370 nm wavelength, was described. The designed Si-SWG/SiO_2 structure with Λ = 205 nm, t_g = 90 nm, and w = 100 nm was fabricated on a GaN-based UV-LED grown on a *c-plane* sapphire substrate by metalorganic chemical vaper deposition method. The fabrication processes are shown in Fig. 5.5. The LED consisted of undoped GaN, an *n*-type GaN layer, *n*-type AlGaN, and AlGaN/GaN quantum well, *p*-type AlGaN, *p*-type GaN layer, and a *p*-type-contact (Au/Ni : 10/10 nm). The Au and Ni film is deposited by resistance heating and EB evaporation. The base pressure of the chamber was 9×10^{-4} Pa. The contact area was 1 mm ×1 mm. After the Au/Ni evaporation, a 200-nm-thick SiO_2 film was deposited onto the UV-LED surface by EB evaporation at 2.67×10^{-4} Pa of vacuum pressure. The evaporation speed of SiO_2 film was about 0.05 nm/s. After SiO_2-film evaporation, the EB resist, which was diluted with anisole (resist: anisole 1: 3), was spin-coated. The first and second spin coat rotation number was 300 for 3 s and 3000 rpm for 90 s. The sample was baked at 120 C° for 30 min to fix the EB resist on the sample surface. After that, the conductive film (espeiser: Zeon) was also spin-coated with 2000 rpm for 30 s, in order to prevent charge up phenomenon. The grating resist pattern was then fabricated on the SiO_2 layer by EB lithography with acceleration voltage of 50 kV and beam current of 100 pA. The chamber pressure was 1.8×10^{-5} Pa. A 90-nm-thick Si film was evaporated using an EB onto the patterned resist, after which the resist was removed.

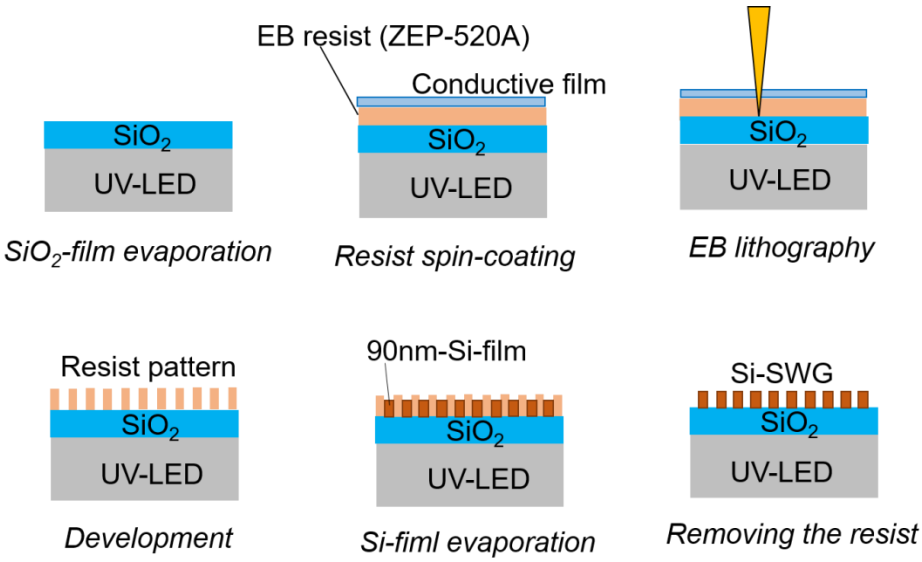

Fig. 5.5 Fabrication process of Si-SWG/SiO_2 underlayer

The top of SEM image of the fabricated Si-SWG was shown in Fig. 5.6. The grating period and Si grating width were 205 nm and 100nm, respectively. The fabricated SWG has uniform the period and grating width over the 1 mm x 1mm area.

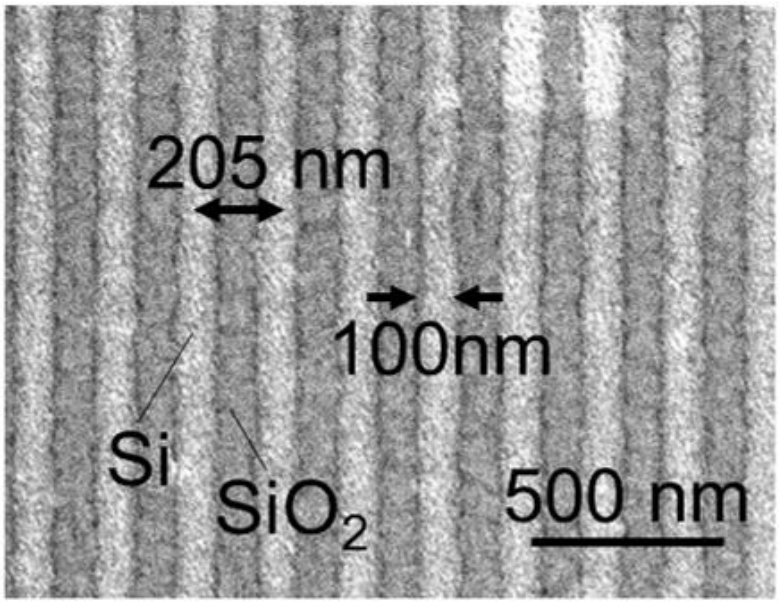

Figure 5.6 Top of view of the fabricated Si-SWG/SiO_2 underlayer

5.4 Demonstration and discussion of a highly polarized emission from the UV-LED with Si-SWG/SiO_2 underlayer

After the SWG fabrication process, EL emission spectra from the UV-LED with Si-SWG/SiO_2 underlayer was measured. The measurement system is the same as that described in chapter 4. The p- and s-polarization light intensity were measured by rotating the polarizer placed at the front of the LED. Also, the current and voltage characteristics was measured. In addition, the angular dependence of the emission was estimated. The measurement system is shown in Fig. 5.7. The rotation center of the system is designed to be at surface of the sample. The distance between the sample and the detector is 2 cm. This distance is enough long to consider the 1 mm x 1 mm SWG area.

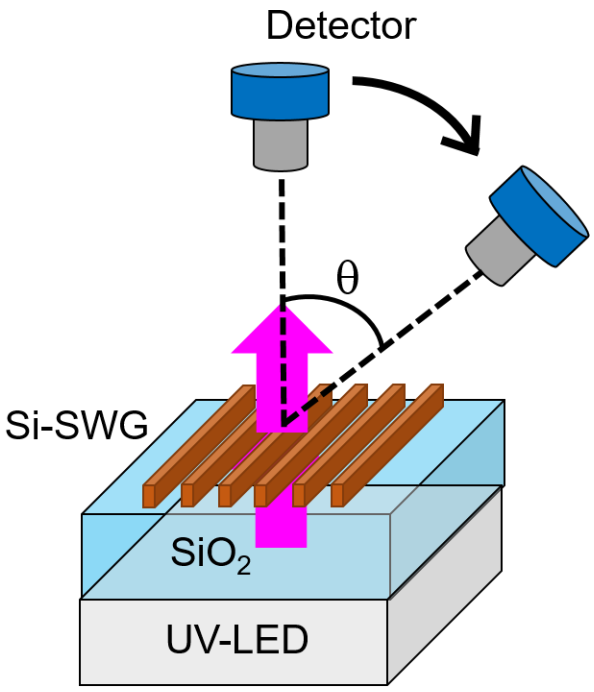

Fig. 5.7 Measurement system of the angular dependence of the emission.

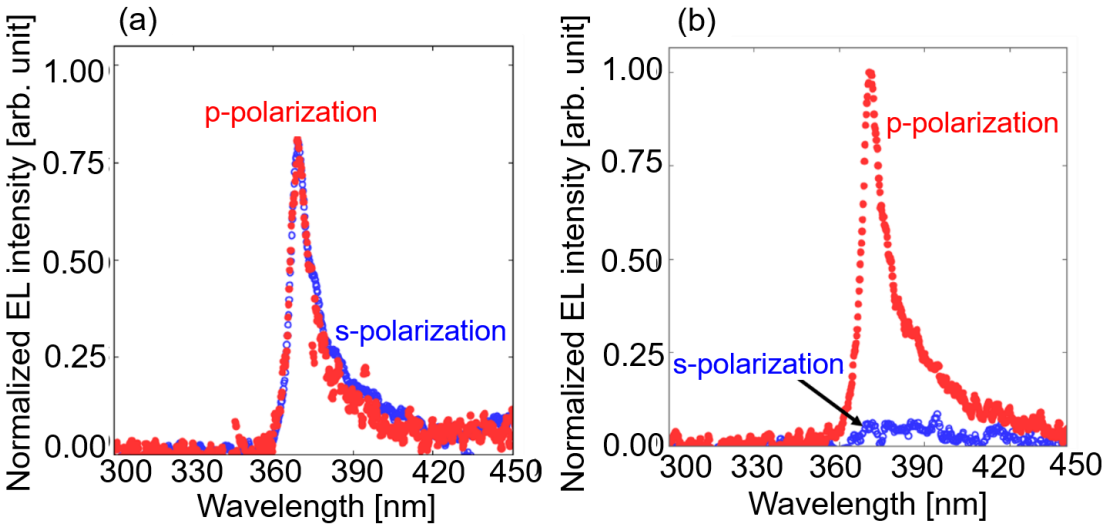

Figure 5.8 Normalized EL spectra for a forward current of 20 mA from the UV-LED, (a) without (b) with the Si-SWG/SiO_2 underlayer structure

Figure 5.8 (a) and (b) show the EL spectra from the UV-LED without and with the Si-SWG/SiO_2 structure for a forward current of 20 mA (namely, the current density 20 mA/mm^2). The emission peak appears around 370 nm. The polarization ratio of the emission from the UV-LED without the SWG structure is nearly 1:1, as shown in Fig. 5.8 (a), and the emission is unpolarized. Unpolarized emission along the *c*-axis is caused by the growth of the GaN active layer on the *c-plane* sapphire substrate. In contrast, the spectra from the UV-LED with a Si-SWG/SiO_2 underlayer structure shows highly polarized emission, as demonstrated in Fig. 5.8 (b), with polarization ratio as high as ~16:1 around 370 nm. To the best my knowledge, this is the highest value obtained for the polarized UV-LEDs and is 4 times the value obtained in our pervious investigation in chapter 4. The origin of this high polarization ratio can be attributed to the suppression of the higher order diffractions at the interface between the LED surface and the SWG, because the subwavelength condition is satisfied by SiO_2 underlayer. The polarization ratio calculated by using the FDTD method is greater than the measured ratio. The

experimental polarization ratio is determined not only by the ratio of the transmittance of p- and s- polarization through the SWG structure, but also by many other factors including light absorption in the bulk of LED chip and in the metal contact electrodes, as well as the chip geometry. We ignored these factors, because the emission from the LED without the SWG is nearly unpolarized as shown in Fig. 5.8 (a). We speculated that one source of this discrepancy was the natural surface oxidation of the Si grating. If one considers the 6-nm-thick oxidation layer formed on the Si-SWG surface as shown in Fig 5.9, the calculated polarization ratio is ~17:1, which is in good agreement with the experimental value of the ratio.

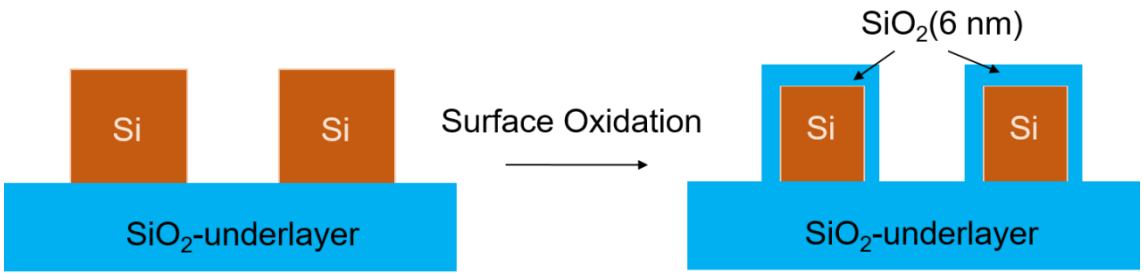

Figure 5.9 Surface oxidation model of the Si-SWG

Moreover, the p-polarized luminescence intensity from the present UV-LED is approximately 1.2 times greater than that of the UV-LED without the SWG structure. One important reason for this increased luminescence is that the escape angle of the photons at GaN/SiO_2 interface is larger than that GaN/air interface as shown in Fig. 5.10. In our LED, the escape cone is broader than that of a conventional planar LED because of the presence of the SiO_2 underlayer; in order words, the contrast in the refractive index at the SiO_2/GaN interface (the critical angle = 42°) is less than that at the GaN/Air interface (the critical angle = 24.6°). This allow more energy of the incident wave to reach the

SWG region. The Bloch eigenmode wave inside the SWG interacts with the incident wave, and the energy of the wave is emitted into the air. The Bloch eigenmode wave can also interact with the incident wave when the incident angle is greater than the critical angle. Thus, in this case, the additional photons can interact with the Bloch eigenmode within the SWG.

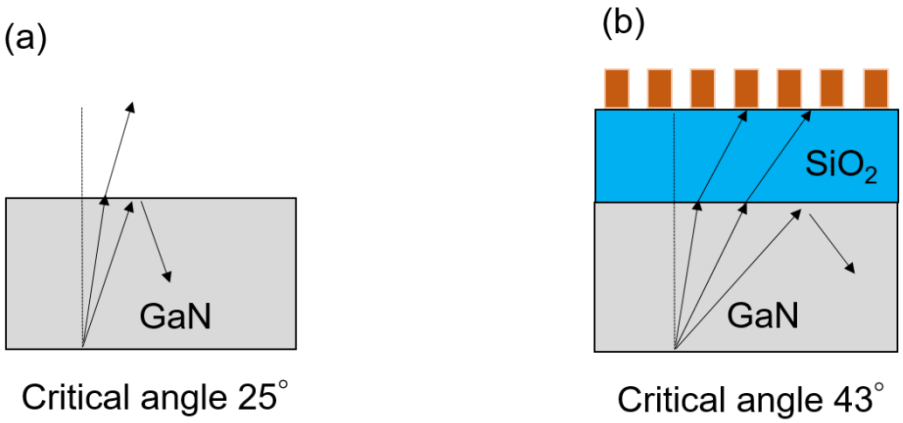

Figure 5. 10 Critical angle at (a) at GaN/air, (b) SiO_2/GaN interface

The angular dependence EL intensity is shown in Fig 5.11. Generally, the emission pattern from a planer LED has Lambert pattern, which has full width at half maximum of 60° angle. On the other hand, the emission from the UV-LED with Si-SWG/SiO_2 underlayer is highly concentrated into normal direction to the LED surface, and this lead to the increasing light intensity for the normal direction. The full width at half maximum is 7°. This emission pattern is explained by the grating equations. Figure 5.12 shows the cross section of Si-SWG/SiO_2. The grating equation is given by [73]

$$n_{air} \sin \theta_n = n_{sub} \sin \theta_{inc} + n \frac{\lambda}{\Lambda} \qquad (5.1)$$

Here, the n_{air} and n_{sub} is the refractive index of substrate (SiO_2) and the transmitting medium (air). In sub wavelength region, only 0^{th}-diffraction ($n=0$) propagate the energy, and the higher orders is evanescent for the normal incident case. On the other hand, the higher, which satisfies eq. (5.1), is propagation mode for the oblique incidence. For example, -1^{st}-order diffraction with diffraction angle θ_n = - 53° satisfied eq. (5.1) for θ_{inc} 45° oblique incidence. As a result, the emission is concentrated to normal direction.

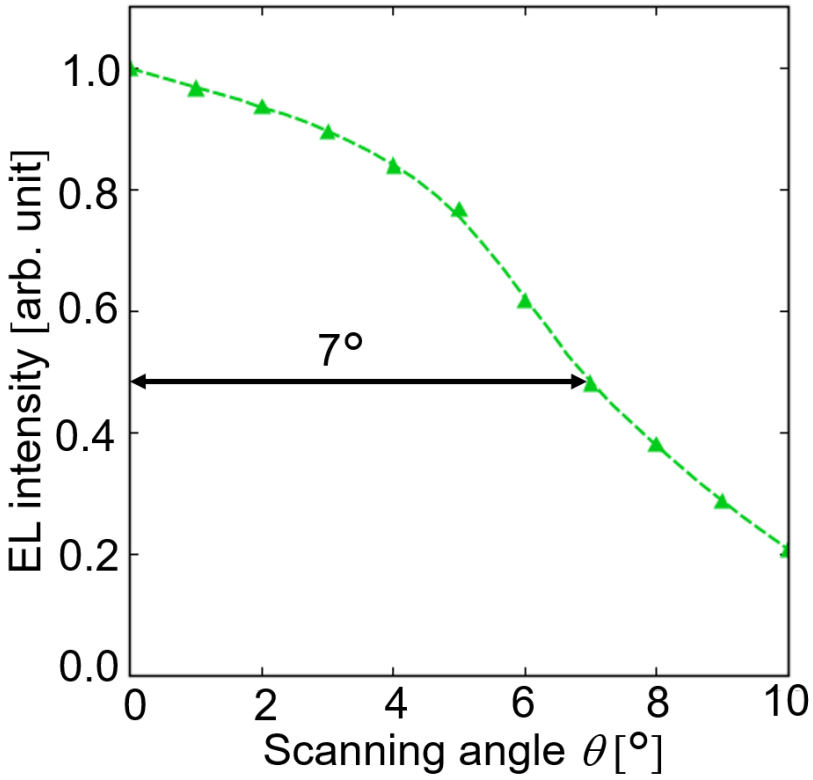

Figure 5.11 Angular dependence of EL emission pattern

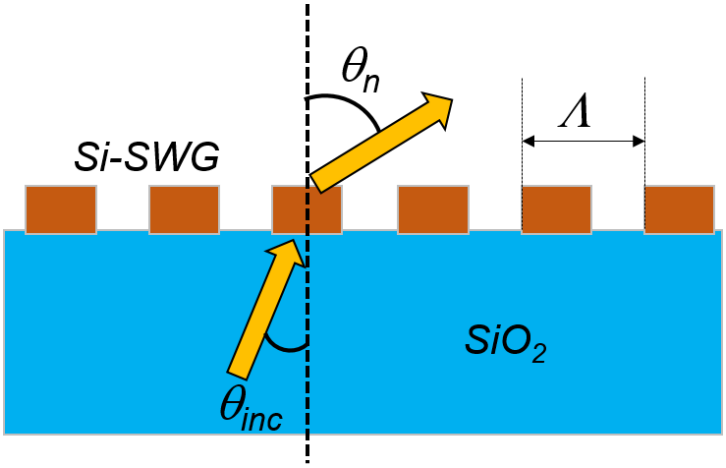

Figure 5.12 Cross section of Si-SWG/SiO_2

We also investigated the influence of the SWG structure on the on the current voltage and EL intensity-current characteristics of the UV-LED. Figure 5.13. The threshold voltage (Vth) for the passage of 20 mA current was 4.98 V, and the almost the same as in the absence of the SWG structure. The magnitude of EL spectra increased substantially and linearly as the current increased to 50 mA. These results indicate that the Si-SWG/SiO_2 underlayer structure control the polarization of the emission without the degradation of the LED performance. In addition, the polarization ratio of the emission was almost constant over I_F = 10 ~50 mA. This results indicates the heat resulting at the LED have no effect on the SWG characteristics, because the SWG and LED region is separated by SiO_2 insulator underlayer.

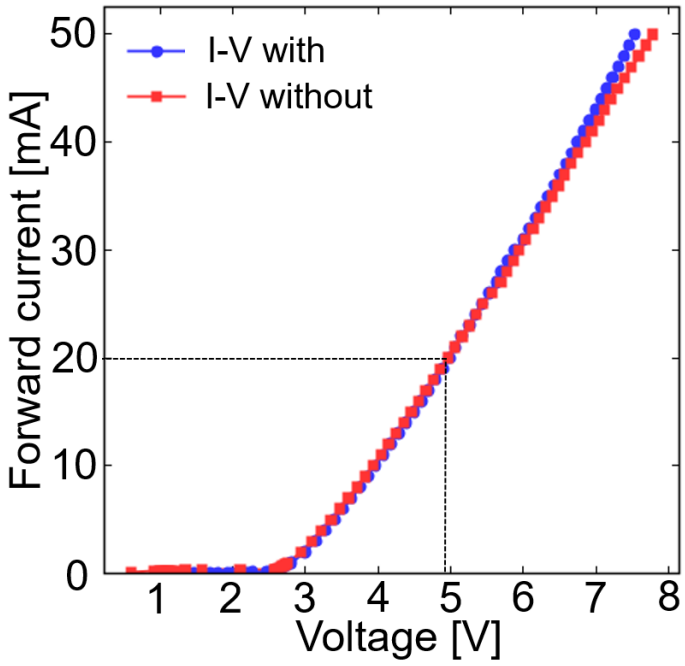

Figure 5.13 I-V characteristics of the GaN-based UV-LED without and with the Si-SWG/SiO_2 structure

5.5 Conclusion

In chapter 5, a highly polarized emission from a GaN-based UV-LED without decreasing the EL emission intensity was experimentally demonstrated suppressing the higher-order diffraction by inserting SiO_2 underlayer between the UV-LED and Si-SWG. In section 5.2, the electromagnetic field distribution within the Si-SWG/SiO_2 underlayer was calculated by FDTD method to investigate the effect of the SiO_2 underlayer on the SWG optical characteristics and optimize the SWG structure for achieving both high transmittance and high polarization ratio. The calculation results shows that the SiO_2 underlayer suppresses the diffracted plane wave at LED surface and is very useful for avoiding a decrease in transmittance. In section 5.3, the fabrication processes of the Si-

SWG/SiO_2 underlayer on the conventional UV-LED was described. In section 5.4, the EL spectra of emission from the LED was estimated and discussed. These results suggest that the UV-LED with the SWG/SiO_2 underlayer can play an important role in the development of various integrated photonic devices.

Chapter 6: Effect of the grating shape on emission characteristics of LED with SWG

6.1 Introduction

In previous chapters, the SWG were analyzed and designed using a typical rectangular grating shape, and a highly polarized GaN-based UV-LED was experimentally demonstrated applying the SWG. The grating side slope, which requires a very fine pitch, is sensitive to the fabrication conditions, including lithographic, crystal growth, evaporation, and etching conditions; the resultant grating shape is not always rectangular [108]. Hence, the considering the influence of this deviation from the rectangular shape on the SWG optical characteristics is important to fully demonstrate the device performance. In chapter 6, the influence of SWG shape on the emission characteristics from a GaN-based LED with a SWG was theoretically and experimentally estimated. A SiO_2, which has the low refractive contrast, was used as the SWG material as the following reason. The eiegnmode state depends on the contrast of the refractive index between the grating and the surroundings, described in chapter 2. When the grating shape is varied from the ideal rectangle, the effective refractive index contrast is decreased. Especially, in low contrast SWG case, the influence of the deviation significantly affects and modifies the optical characteristics of the SWG, because the change of the relative refractive index caused by the deviation is larger than that in high contrast SWG. Thus, low contrast SWG is suitable for the estimation of the shape effect on the optical characteristics. In section 6.2, the electromagnetic field distribution within the SiO_2-SWG was calculated by FDTD method in order to theoretically estimate the influence of the grating shape on the optical characteristics of the LED emission with the

SWG. In section 6.3, a trapezoid-shaped SiO_2-SWG structure was fabricated on the surface of a GaN-based blue LED using electron-beam lithography. In section 6.4, the EL spectra from the LED with the trapezoid-shaped SiO_2-SWG were shown, and the effect of the deviation of the grating shape on the device performance was discussed.

6.2 Theoretical investigation for a shape effect

In this section, the effect of the deviation of the SWG shape from the ideal rectangle was theoretical estimated and discussed for the effective design of the device.

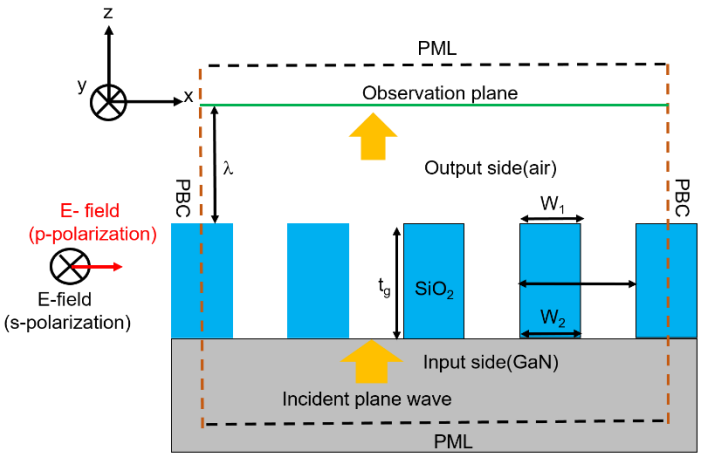

Figure 6.1 Numerical model for investigating electromagnetic field distribution.

Figure 6.1 shows the cross-section of the numerical model used to investigate the electromagnetic field distribution for the shape effect. In this model, SiO_2-SWG was arranged on the p-type GaN of the LED surface. The grating period, height and bottom side length, defined in Fig. 6.1, were set to Λ = 430 nm, t_g = 200 nm, and W_2 = 215 nm, respectively. The width of the top side of the grating stripe was assigned W_1. The refractive indices of SiO_2 (n_{SiO2}) and *p*-type GaN (n_{GaN}) employed are taken from the

previous reported literature [105,106]. For example, n_{SiO2} = 1.484 +0i, n_{GaN} = 2.366 + 0.0116i for 400 nm, n_{SiO2} = 1.482 +0i, n_{GaN} = 2.324 + 0.0059i for 420 nm, n_{SiO2} = 1.481 +0i, n_{GaN} = 2.313 + 0i for 460 nm, n_{SiO2} = 1.479 +0i, n_{GaN} = 2.313 + 0.0116i for 480 nm were used. The transmitted light intensity through the SiO_2-SWG was calculated in the observation plane which was placed at the air side for the s- and p-polarization. The width of the top side of the grating stripe of W_1 = 0, 10, 100, and 215 nm were used in order to clarify the dependence of the SWG optical characteristics on the grating shape. The bottom width of the grating stripe was kept constant, while the top width was varied.

The dependence of the SWG optical characteristics on the grating shape as a function of the incident wavelength is shown in Fig. 6.2 and summarized in Table 6.1. The polarization selectivity has a peak around 440 nm for each grating shape, reaching a polarization ratio approaching 5 at W_1 =100 nm. As W_1 decreases from 100 to 0 nm, the peak value dramatically decreases. The peak for W_1 = 0 nm is lower than half the height of that for W_1 = 100 nm. The magnetic field distribution at a certain time for s-polarized incidence is shown in Fig. 6.3. The light in the case of the grating with W_1 = 215 nm is confined to the high refractive index region in the grating structure. The confinement of the light becomes weaker with decreasing W_1, and the light eventually penetrates into the air gap region. The transmittance of the s-polarized light also varies with variations of the grating shape. This can be explained by the shift of the low transmittance resonance condition due to the different eigenstate.

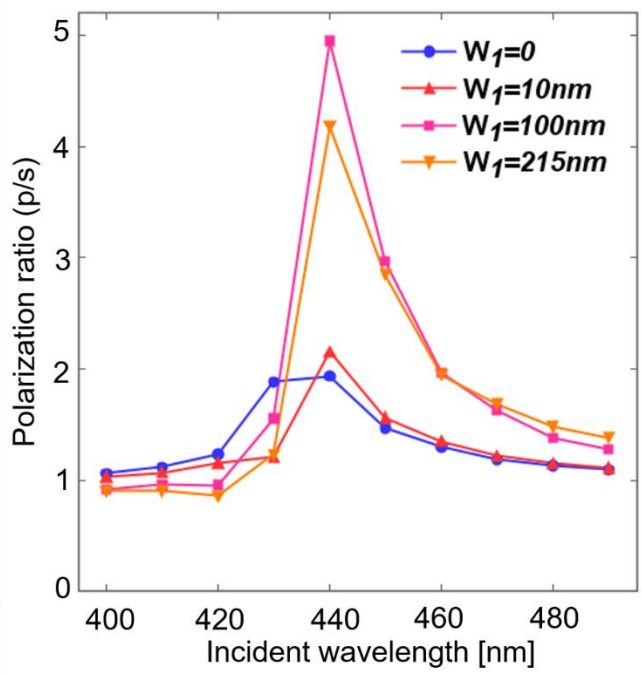

Figure 6.2 The SiO_2-SWG polarization ratio as a function of the incident light wavelength with W_1 = 0, 10, 100, and 215 nm.

Table 6.1 Summarized polarization ratio of the SiO_2-SWG at the incident wavelength 440 nm.

W_1 [nm]	Polarization ratio
0	1.93
10	2.16
100	4.95
215	4.18

If the modes are antiphase and cancel each other's amplitude, a low-transmittance resonance condition is created. In this case, the low-transmittance condition is formed with s-polarized light. Deviation from the rectangular grating shapes modifies the mode's eigenstate, and the result is the varying degree of confinement of light, where the resonance conditions with W_1 = 0, 10, and 100 nm differ from that in the ideal rectangle

grating (where W_1 = 215 nm). As a result, the transmittance of s-polarized light, for which the low-transmittance resonance condition is formed, varied with decreasing W_1. The calculation results suggests that the ideal rectangle grating is not always the optimal structure, and the design for the SWG consider the shape effect open up the feasibility for the high performance of the device with the SWG.

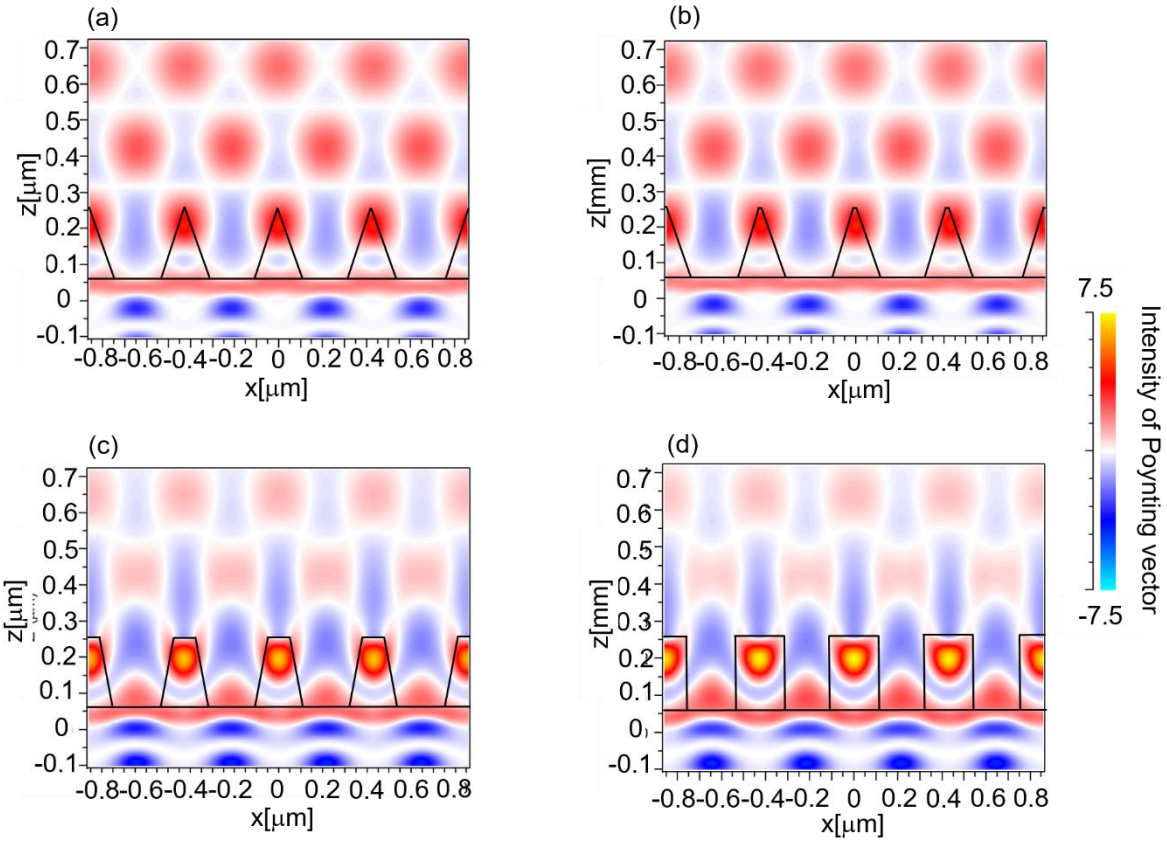

Figure 6.3 Poynting vector distribution at a certain time for s-polarization (a) W_1 = 0, (b) W_1 = 10, W_1 = 100, W_1 =200 nm

6.3 Fabrication of a trapezoid shape SiO_2-SWG

The fabrication processes of the trapezoid shape SiO_2-SWG on a InGaN-based LED was described. The LED grown on a c-plane sapphire substrate by a metalorganic chemical vapor deposition method was used. The structure comprises layers of *p*-type GaN, p-type AlGaN, InGaN/ GaN multiquantum well, n-type AlGaN, n-type GaN, and undoped GaN on the sapphire substrate. The emission peak is around 430 to 440 nm. The SiO_2-SWG was fabricated using electron-beam lithography and evaporation, as described in Fig.6.4.

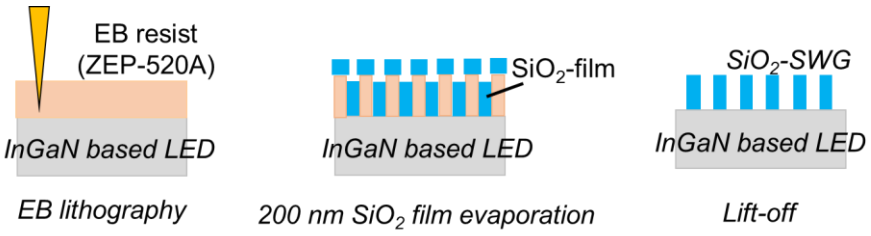

Figure 6.4 Fabrication processes of SiO_2-SWG

At first, the electron-beam resist (ZEP-520A) was diluted with methoxybenzene (anisole) to a 1∶1 solution and the resist film was spin-coated onto the LED surface at 2000 rpm for 90 s to a thickness of ~200 nm. The resist-coated LED was heated on a hotplate at 180 °C for 3 min. Secondly, the grating pattern, with a 430 nm pitch and 200 nm grating bar width, was drawn on the LED's top surface using an electron beam at 50 kV and 100 pA. The grating pattern was developed by n-amylacetate (ZED-50N) at 20°C for 15 s. After developing, a 200-nm SiO_2 film was evaporated onto the grating pattern using an electron beam at a base pressure of 2.7×10^{-3} Pa, and the resist film was removed by dimethyl sulfoxide. Finally, a 20-nm thick Au/Ni p-contact film was evaporated as the

electrode.

A cross-sectional scanning electron microscope view of the SiO_2-SWG on the surface of the GaN-based blue LED is shown in Fig. 6.5. The resultant grating pitch, bottom width and height are 430, 215, and 200 nm, respectively. The top side width of the grating is ~10 nm, providing a trapezoidal resultant grating shape. The trapezoid shape is typical of the fabricated SiO_2 stripe [108].

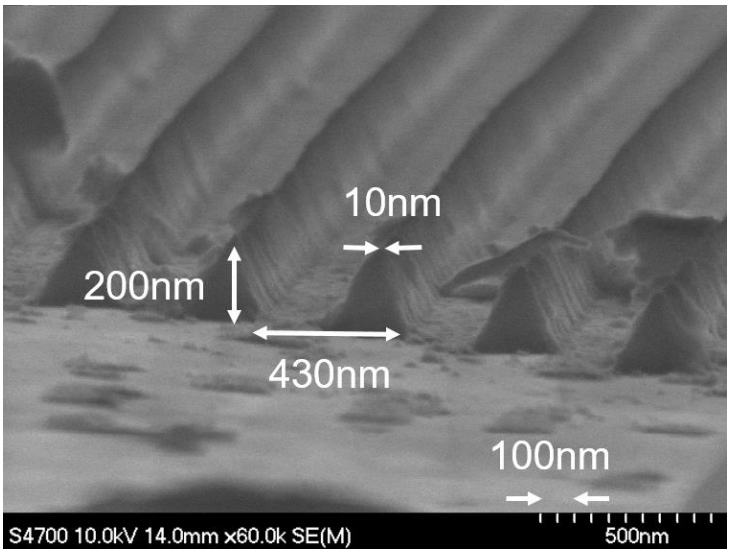

Figure 6.5 Cross-sectional scanning electron microscope view of the SiO_2-SWG fabricated on an InGaN-based LED.

6.4 Experimental shape effect and discussion

The EL spectra at a forward current I_F of 10 mA from the blue LED with SiO_2-SWG are shown in Fig. 6.6. The open and filled circles indicate the intensities of p- and s-polarized emission, respectively. The p- and s-polarized spectra were measured by rotating the polarizer placed in front of the blue LED. The spectra show a polarized emission from the LED with SiO_2-SWG in the wavelength region from 420 to 450 nm.

The peak polarization ratio reaches ~3.2 at the wavelength of 440 nm. The experimental polarization ratio exceeds that numerically predicted by the FDTD method.

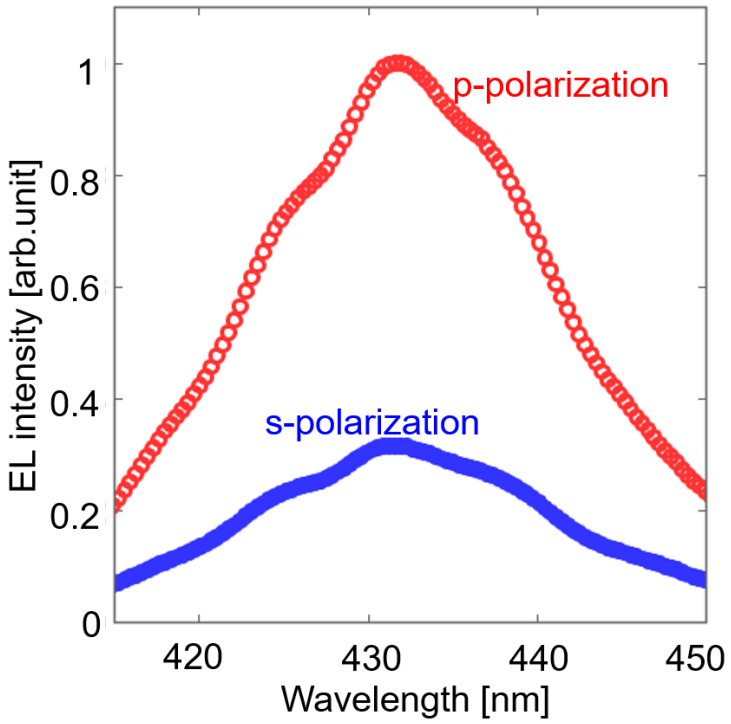

Figure 6.6 EL spectra of the emission from the LED with a trapezoid SiO_2-SWG

In the resultant SWG, the refractive index of the grating depends on the fabrication process. The dependence of the SWG polarization characteristics on the actual refractive index of the grating should be considered for accurate analysis of the experimental results. The actual n_{SiO2} of SiO_2 evaporated by the e-beam depends on the evaporation conditions, and n_{SiO2} ranges from 1.46 to 1.56 at the 440 nm wavelength [109]. The origin of the higher polarization ratio than that numerically predicted might be consider to the change of n_{SiO2}. To verify this consideration, the dependence of the polarization characteristics of the LED's emission on n_{SiO2} was investigated using the

FDTD method with the model shown in Fig. 6.1. For the calculation, the W_1 was set to 10 nm. The calculated polarization characteristics of the emission are shown as a function of n_{SiO2} in Fig. 6.7. The open and filled circles show the transmittance through the SiO_2-SWG for the case of perfectly p- or s-polarized incident light. Crosses indicate the polarization ratio at different refractive indices. The transmittance of p-polarized light is almost insensitive to variations in n_{SiO2}.

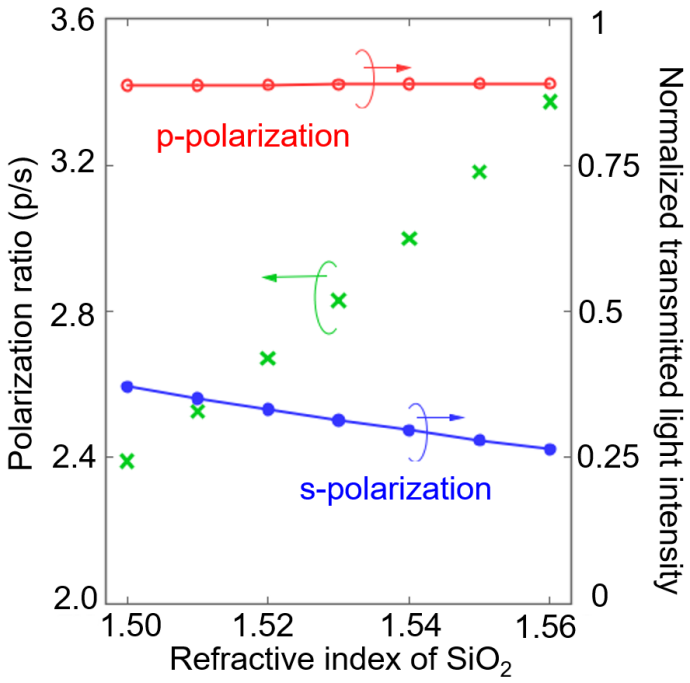

Figure 6.7 Dependence of the polarization characteristics of the emission on n_{SiO2} at wavelength of 440 nm

However, the transmittance of s-polarized light linearly decreases with increasing n_{SiO2}. The polarization ratio also linearly increases from 2.4 to 3.4 with increasing n_{SiO2}. When n_{SiO2} is set to 1.55, the calculated polarization ratio coincide to the experimental value. The agreement between the calculated polarization characteristics with the actual n_{SiO2} and the experimental characteristics can be explained as follows. The light velocity in the

high refractive index region is slower than that in the low refractive index material. Thus, the electromagnetic field distribution, eigenstates, and low-transmittance resonance conditions all vary with increasing n_{SiO2}. This design considering the shape effect on the optical property of the SWG improve and exhibit for the optimal performance of device using the SWG, and this approach transformed the difficulty for the shape control in the fabrication process of the very fine structure to the advantage for optimizing device performance.

6.5 Conclusion

In this chapter 6, the influence of SWG shape on the emission characteristics from a GaN-based LED with a SWG was theoretically and experimentally estimated. In section 6.2, the electromagnetic field distributions within the various shape of SiO_2-SWG on the LED surface were calculated by FDTD method to investigate the effect of deviation of the grating shape from the rectangle on the LED emission characteristics. In section 6.3, the fabrication processes of the trapezoid SiO2-SWG on the LED surface was described, such as electron beam lithography, evaporation of SiO_2, and lift-off process. In section 6.4, the emission from the LED with trapezoid SiO_2-SWG was discussed to experimentally estimate the influence of SWG shape on the device performance, and the design considering the grating shape was useful to fully demonstrate the performance of device with SWG.

Chapter 7: A highly sensitive refractive index detection device utilizing SWG

7.1 Introduction

In previous chapter, the deviation of the grating shape from the ideal rectangular modified the electromagnetic filed distribution in the SWG, because the refractive index contrast between the grating and surrounding material is changed by the deviation. This suggest that the refractive index of surrounding material can be detected with highly sensitive.

In this chapter, ultra-highly sensitive refractive index detection device with normal incident geometry was developed by using the SWG. In section 7.2, the SWG was theoretically designed for highly sensitive detection of the refractive index using the wavenumber dispersion relation of the eigemode. To understand the detection phenomena of the SWG, the electromagnetic filed distribution was calculated by FDTD method. In section 7.3, we described the fabrication process of the designed SWG structure mentioned in section 7.2. In section 7.4, the highly sensitive detection of the refractive index was experimentally demonstrated, and the origin of the highly sensitively was discussed.

7.2 Design of the Si_3N_4-SWG for refractive index detection device

The eigenmode state within the SWG strongly depends on the refractive index contrast between the grating and the surrounding material. This property is very useful for the refractive index of the surrounding material. In this section, the SWG structure was designed for the refractive index detection using the wavenumber dispersion relation of the eigenmoide. First of all, the operation nature of the detection using SWG was described. The SWG model for refractive index detection is shown in Fig. 7.1. A Si_3N_4 was employed as the SWG material due to the high refractive index value, low dispersion, and chemical stability in the broad wavelength region [110]. As described in the previous chapters, the eigenmode waves due to the periodic refractive index distribution interact with the incident light wave. If these eigenmodes formed the destructive interface, in which the modes canceled each other at exiting plane, the transmitted light become very low owing to the strong mismatch to existing plane wave. The phase of the eigenmode strongly depends on the contrast of refractive index between the grating and the surrounding material. When the surrounding refractive index (n_s) was varied, the transmittance of the SWG was changed. Thus, the change of the surrounding refractive index can be detected.

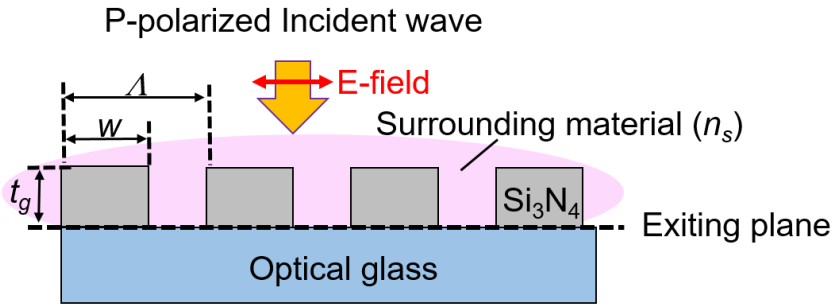

Figure 7.1 Si_3N_4-SWG model for refractive index detection

Based on this operation nature, the SWG structure was designed by the wavenumber dispersion relation. The dispersion relation of Si_3N_4-SWG, which is surrounded by the material with n_s was derided, and the dispersion relation is obtained by

$$(\frac{n_{bar}}{n_s})^{-2} k_{s,m} \tan(k_{s,m} w/2) = -k_{a,m} \tan(k_{a,m} a/2) \quad (m = 1,2,3\cdots) \tag{7.1}$$

$$\left(\frac{2\pi n_s}{\lambda}\right)^2 - k_{a,m}^2 = \left(\frac{2\pi n_{bar}}{\lambda}\right)^2 - k_{s,m}^2 = \beta_m^2 \quad (m = 1,2,3\cdots) \tag{7.2}$$

The value of nbar is refractive index of Si_3N_4, and the grating material was assumed Si_3N_4 value of n_{bar} was taken in the literature [110]. The p-polarized light with the wavelength of 360~400 nm normally emerged to the SWG. The reason why these wavelengths were used is as follows. The applications of the refractive index detection are typically used in water (for example, the bio-sensing). Hence, the wavelengths of 360~400 nm were used for avoid the decay of the light intensity in the water, because

the absorption coefficient in water was small in these wavelengths [111]. The p-polarization dispersion relation in the Si_3N_4 at 365nm was shown in Fig. 7.2.

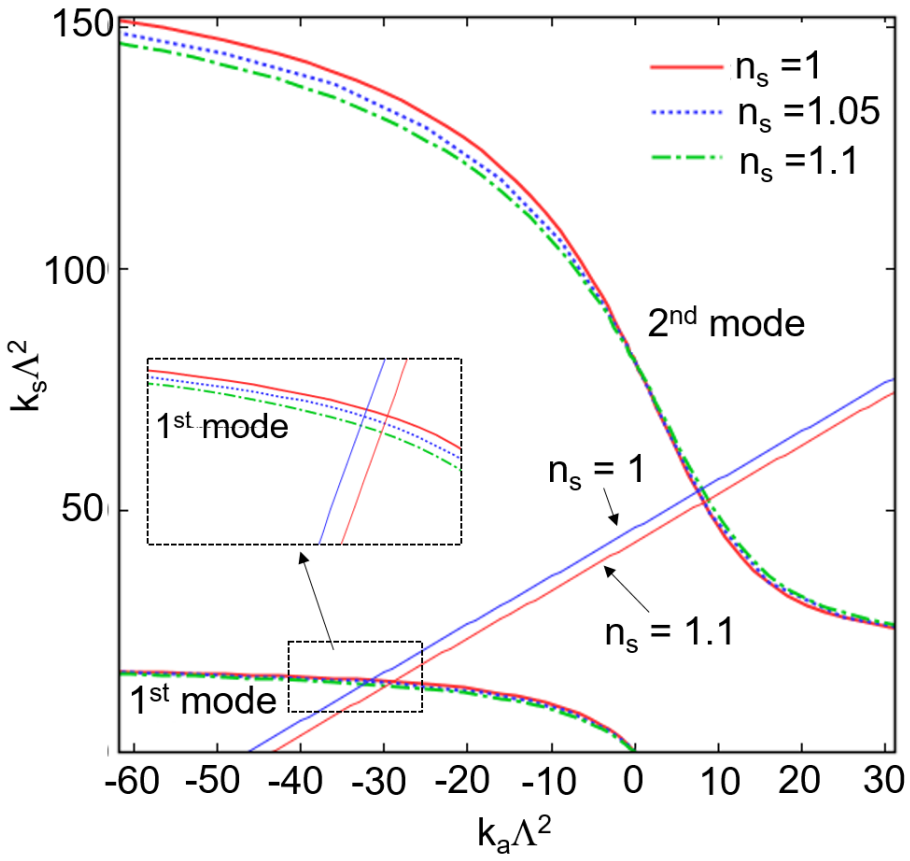

Figure 7.2 Wavenumber dispersion relation in Si_3N_4-SWG surrounded with n_s

The solid curves and the lines represent eq. (7.1) and (7.2), respectively. When the surrounding material was changed, the intersection between the solid curve and the dashed line was moved. Hence, the phase of the eigenmode was varied due to the change of n_s, and the transmittance was also modified. Hence, the change of n_s can be detected as the transmitted intensity through the SWG. Based on the dispersion relation, the grating period, the height, and the width were Λ = 215 nm, t_g = 150 nm, and w = 150nm, respectively to form the cancelation of the eigenmode in the various surrounding

refractive index detection. To estimate the dependence of the transmittance on n_s, the electromagnetic field distribution in the SWG was calculated by FDTD method.

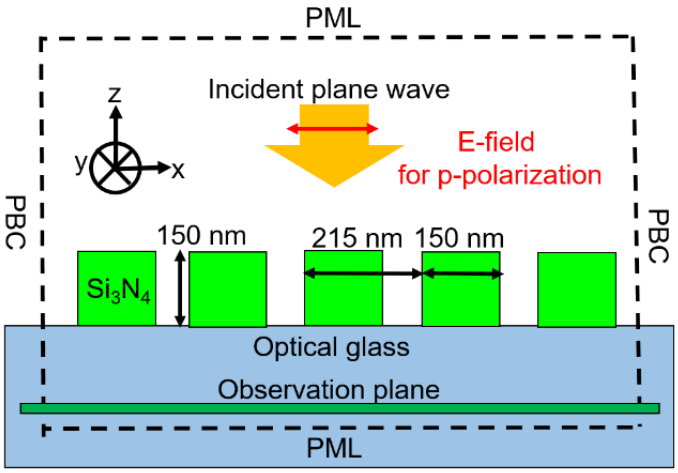

Figure 7.3 FDTD calculation model for the refractive index detection using Si_3N_4-SWG

The calculation model is shown in Fig. 7.3. The Si_3N_4-SWG is arranged on the optical glass. The grating period, the width of the grating stripe and grating height are 230 nm, 160 nm, and 150 nm, respectively. The incident light emerges from outside to the substrate. The transmitted light intensity was calculated at the observation plane when the surrounding refractive index n_s was varied. Dependence of the transmittance of the Si_3N_4-SWG on n_s is shown in Fig. 7.4. In Fig. 7.4, the dips of the transmittance for n_s was found for the various incident wavelength. With the increasing the incident wavelength, the dips were also obtained at different value of n_s, and these dips were shifted to large value of n_s. At each dips, the transmittance rapidly modified around each dips with the change of n_s value and indicates the minuscule of the change of n_s can be detected as the transmitted light intensity. The slope of the transmittance per refractive index unit (RIU) reached to about 7600%/RIU, and its broad range of the detection index

value with ns = 1~ 1.8 can be achieved without the oblique incidence geometry. These results mean that this detection device is suitable for the integration device, compared with that with oblique incidence.

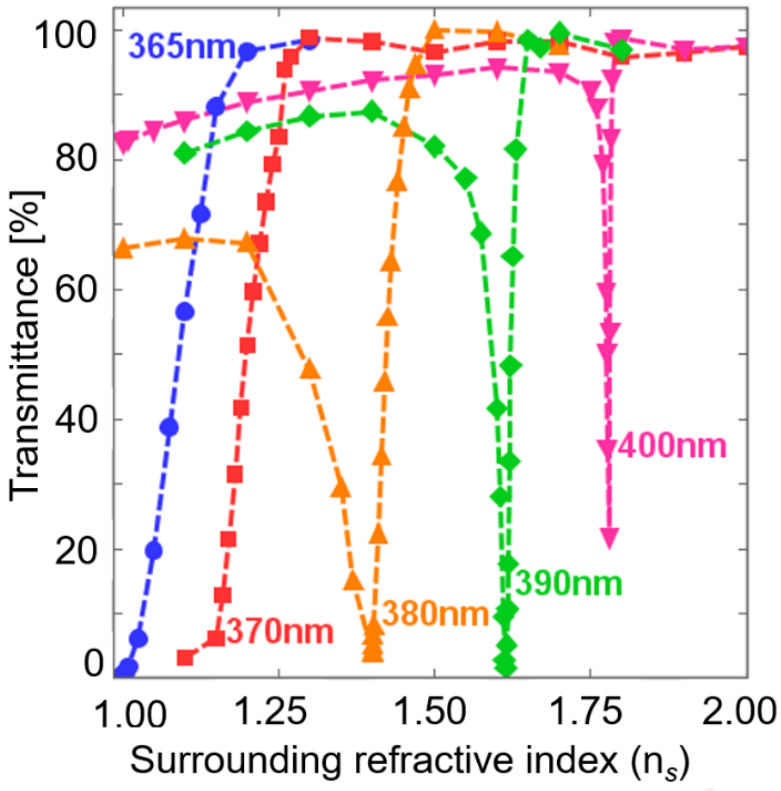

Figure 7.4 The FDTD calculated dependence of the transmittance on n_s

The magnetic field distribution of low and high transmittance condition at the wavelength 365 nm are also shown in Fig. 7.5. In low transmittance condition at n_s = 1, the field of the eigenmodes were canceled each other at the interface between the substrate and the SWG over grating period, and the transmitted field intensity was very low. In contrast, the cancelling of each modes phase in case of high transmittance condition (n_s = 1.25) is not enough, and the transmitted field intensity become larger than that in case of n_s = 1. The dependence of the SWG on the surrounding refractive index

can be explained by the varying the phase of the Bloch-eigenmodes at the interface. The light velocity in the high refractive index is slower than that in the low. The phase of Bloch-eigenmodes at the interface is varied with the increasing of n_s, and thus the transmittance is deviated from that in n_s =1.

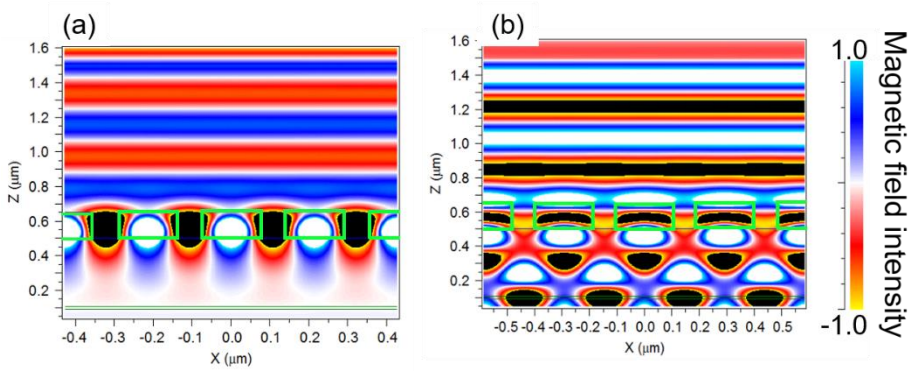

Figure 7.5 Magnetic field distribution at (a) low (b) high transmittance condition

7.3 Fabrication of refractive index detection device using Si_3N_4-SWG

In this section, the fabrication process of the Si_3N_4-SWG was described. The fabrication process is shown in Fig. 7.6.

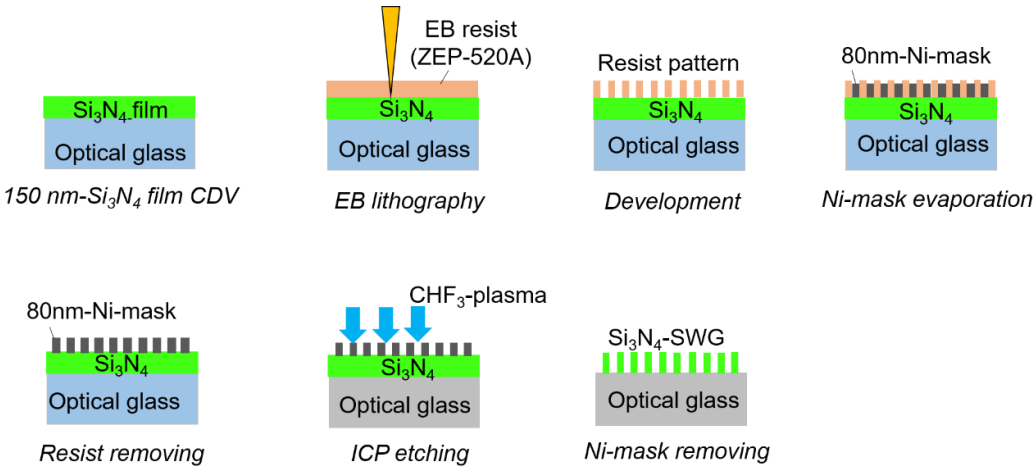

Figure 7.6 Fabrication processes of the Si_3N_4-SWG on the optical glass

The optical glass substrate was cleaned by the method described in the section

4.1 to the cleaning the surface of the glass. After that, a 150 nm Si_3N_4 film was deposited on the optical grass substrate by chemical vaper deposition method. The EB resist, which was diluted with anisole (resist: anisole 1: 3), was spin coated on the Si_3N_4 film. The first and second spin coat rotation number was 300 rpm for 3s and 3000 rpm for 90 s. The designed Si_3N_4-SWG pattern with Λ = 215 nm, and w = 65 nm was fabricated by EB lithography with acceleration voltage of 50 kV. And then, an 80 nm-thick Ni-film was evaporated onto the patterned resist, and resist pattern was removed. The Si_3N_4-SWG was fabricated on the sample surface by ICP etching. A CHF_3 gas was used for the Si_3N_4 etching. The etching conditions are summarized in table.7.1.

Gas	ICP power [W]	Bias [W]	Flow rate [SCCM]	Pressure [Pa]	Etching time [min]
CHF_3	100	100	10	1	24

Table 7.1 ICP etching condition of the fabrication of Si_3N_4-SWG

The Ni-mask pattern was removed by dilute nitric acid after ICP etching process. The top view of SEM image of the fabricated Si_3N_4-SWG in Fig. 7.7. The fabricated grating has the 230 nm period and 160 nm grating width. The grating area is 1 mm x 1 mm. An 80 nm-Cr-layer was evaporated on the region of 0.6 mm from the SWG area in order to observe only transmitted light through the SWG in the experiment described in next section.

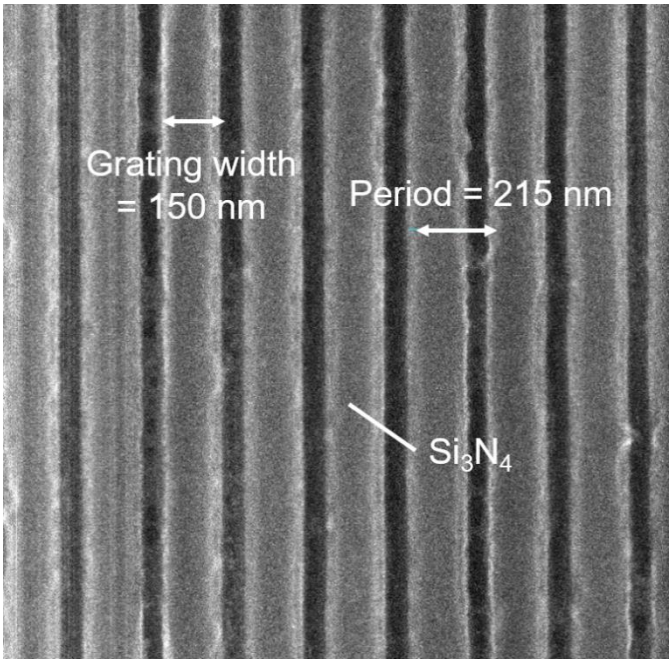

Figure 7.7 Top of image of the fabricated the Si_3N_4-SWG

7.4 Experimental demonstration of the highly sensitive refraction detection using Si_3N_4-SWG

The transmitted light intensity through the fabricated Si_3N_4-SWG was measured. The experimental setup is shown in Fig.7.8. The polarizer was placed in front of a halogen lamp to make the p-polarized the incident light. In this experiment, the methanol solution was used to investigate the dependence of the SWG optical characteristic on the surrounding refractive index. The sample was placed in the plastic cell, which was filled with the methanol solution. The light normally enter to the SWG, and the transmitted light intensity was measured with the increasing the mass concentration of methanol in the solution.

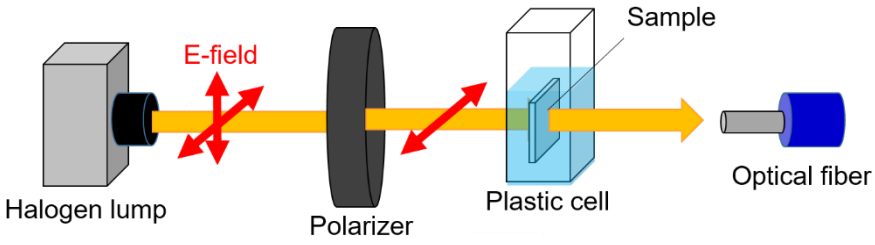

Figure 7.8 Experimental setup for the refractive index detection

Base on the calculation mentioned in the previous section, the transmitted light intensity at 380 nm decreases with the increasing the methanol concentration in the solution (around n_s =1.33 in Fig.7.4). The dependence of the transmitted light intensity of 380 nm wavelength on the value of n_s is shown in Fig. 7.9. The value of the n_s is derived from mass concertation of water (1.3406) and ethanol (1.3753), and the refractive index of water and ethanol were taken from the literatures [111,112]. The error bar shows standard deviation over 3 measurements. In Fig. 7.9, the maximum transmitted light intensity was observed at n_s = 1.3425 and decrease with the increasing n_s *value*. The variation of the transmitted light intensity for the change of n_s reached to -2.52 x 10^4 counts per refractive index unite (RIU) of n_s. These results show the small refractive index change can be detected by using Si_3N_4-SWG structure, and the 4^{th}-order decimal change of the surrounding refractive index detection was demonstrated without the oblique incident geometry.

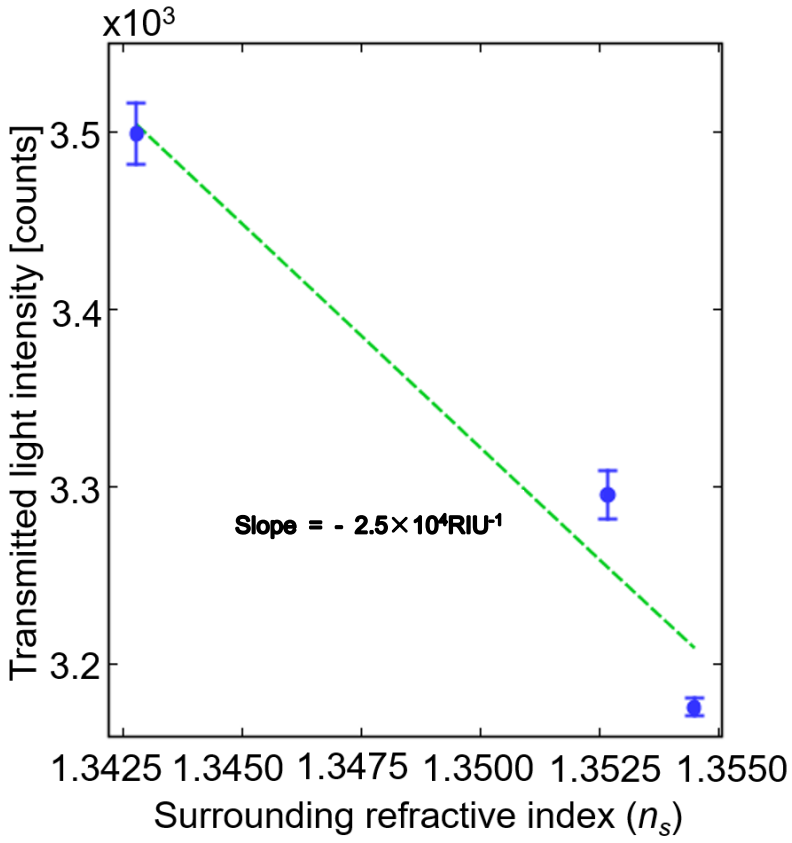

Figure 7.9 Experimental setup for the refractive index detection

The origin of very high selectively is considered to the destructive interface formed by usingtwo eigenmode. The transmitted light is described as a superposition of the propagation eigenmdes exited in the SWG, the destructive interface was formed when these modes canceled each other. When the surrounding refractive index around the SWG was changed, the phases of these eigemodes were varied. The transmittance was determined by not only the phase of one mode but also that of all modes, which were excited. As a result, the very highly sensitive refractive index detection can be realized without the oblique incident geometry. In addition, this detection was not restricted by the target of the detection, because the detection mechanism depends on only the refractive index of the surrounding material.

7.5 Conclusion

In this chapter, a highly sensitive refractive index detection device without the oblique incident geometry was experimentally demonstrated by using Si3N4-SWG. In section 7.2, the principle of operation of the refractive detection using the SWG was described, and the SWG structure was designed based on the dispersion relation and the electromagnetic field distribution by FDTD method for the highly sensitive with its wide range of refractive index. In section 7.3, the fabrication process of the designed SWG structure was presented. In section 7.4, the experimental performance of the SWG for the detection of the minuscule refractive index change was evaluated, and the origin of the highly detection sensitively was discussed

Chapter 8: Conclusion

In this study, the VIS ~ UV light control device utilizing the SWG structure was successfully developed. The light propagation mechanism in SWG was elucidate to provide a new design concept of the SWG at UV ~ VIS wavelength.

In chapter 3, the wavenumber dispersion relation of the eiegnmode within the SWG was derived to reveal the propagation property of the eigenmode in the UV wavelength region. The dispersion shows the wavenumber of the eigenmode broadened by the deceasing life time due to the photon absorption in the SWG. The electromagnetic field distribution is also investigated by FDTD method. The distributions suggested the transmittance through the SWG can be maintained, regardless of the large photon absorption. This approach provides new insight into the SWG design for UV light control and broadens the feasibility of development UV photonic device without the significantly decreasing of the light intensity.

In chapter 4, a polarized emission from GaN-based UV-LED was experimentally demonstrated by using the AlGaN-SWG. The polarization ratio of the EL emission from the LED, reached as 4 at the UV wavelength of 360 nm. Then, the EL spectra was discussed by the wavenumber dispersion relation and the FDTD calculated electromagnetic field distribution. The discussion indicated the diffraction phenomena occurred at the interface between the SWG and the LED surface due to the destruction of subwavelength condition, and the inserting low refractive index layer between SWG and LED substrate significantly improve the polarization characteristic of the emission.

In chapter 5, a highly polarized emission from a GaN-based UV-LED without decreasing the EL emission intensity was experimentally demonstrated suppressing the diffraction phenomena by inserting low refractive index underlayer between the UV-LED

and SWG. The electromagnetic field distribution calculated by FDTD method revealed that the low refractive index underlayer suppresses the diffraction at LED surface and is very useful for avoiding a decrease in transmittance. Using this structure, a highly polarized UV emission without the decay of the EL intensity was experimentally demonstrated. The polarization ratio reached to 17 at the wavelength 0f 370 nm, and the EL intensity is 1.2 times larger than that without the structure.

In chapter 6, the influence of the deviation of grating shape on the emission characteristics from a GaN-based LED with a SiO_2-SWG was theoretically and experimentally estimated for the effective design for the device with the SWG. The electromagnetic field distributions within the various shape of SiO_2-SWG were calculated by FDTD method to investigate the effect of deviation of the grating shape from the rectangle on the LED emission characteristics. The emission from the LED with trapezoid SiO_2-SWG was discussed to experimentally estimate the influence of SWG shape on the device performance, and the design considering the grating shape was useful to fully demonstrate the performance of the device with SWG.

In chapter 7, a highly sensitive refractive index detection devices with normal incident geometry was developed by using Si_4N_3-SWG. The SWG was designed for the highly sensitive detection of refraction index by using the wavenumber dispersion relation, and the dependence of the transmittance on the surrounding refractive index was calculated. The calculation results suggest that the highly sensitive detection for its value with wide range utilizing the SWG. The designed SWG experimentally and successfully demonstrated 4^{th}-order decimal change of surrounding refractive index with normal incident geometry.

In this study, the UV and VIS wavelength photonic devices without the

significantly decreasing of the light intensity can be demonstrated. These devices can play important role in the shorter wavelength to overcome the restriction of the design by the physical property of the materials in shorter wavelength region.

References

[1] 田崎三郎, 通信工学. 朝倉書店, 2006.

[2] B. Ferguson and X. C. Zhang, “Materials for terahertz science and technology,” *Nature Materials*, vol.1, no. 1, p. 26–33, Sep. 2002.

[3] K. Kawase, Y. Ogawa, and Y. Watanabe, “Non-destructive terahertz imaging of illicit drugs using spectral fingerprints,” *Opt. Express*, vol. 11, no. 20, p.2549–2554, Oct. 2003.

[4] Y. Zhou, M. C. Y. Huang, and C. J. Chang-Hasnain,, “Tunable VCSEL with ultra-thin high contrast grating for high-speed tuning,” *Opt. Express*, vol. 16, no.18, p. 14221–14226, Spt. 2008.

[5] M. C.Y. Huang, Y. Zhou, and C. J. Chang-Hasnain, “Nano electro-mechanical optoelectronic tunable VCSEL,” *Opt. Express*, vol. 15, no. 3, p. 1222–1227, Jan. 2007.

[6] C. H. Tsuei, W. S. Sun, and C. C. Kuo, “Hybrid sunlight/LED illumination and renewable solar energy saving concepts for indoor lighting,” *Opt. Express*, vol. 18, no. 54, p. A640-A653,Nov. 2010.

[7] X. Xiao, B. Javidi, M. Martinez-Corral, and A. Stern, “Advances in three-dimensional integral imaging: sensing, display, and applications [Invited],” *Appl. Opt.*, vol. 52, no. 4, p. 546-560, Jan. 2013.

[8] Y. Muramoto, M. Kimura, and S. Nouda, “Development and future of ultraviolet light-emitting diodes: UV-LED will replace the UV lamp,” *Semicond. Sci. Technol.*, vol. 29, no. 8, p. 84004, Jun. 2014.

[9] 応用物理学会, 応用物理分野のアカデミック・ロードマップの作成報告書, 2008.

[10] H. J. B. Jagt, H. J. Cornelissen, D. J. Broer, and C. W. M. Bastiaansen, “Linearly polarized light-emitting backlight,” *J. Soc. Inf. Disp.*, vol. 10, no. 1, p. 107, 2002.

[11] H. Watanabe, N. Miyagawa, S. Takahara, and T. Yamaoka, “Photo-alignment material with azobenzene-functionalized polymer linked in film,” *Polym. Adv. Technol.*, vol. 13, no. 7, pp. 558–565, Jul. 2002.

[12] S. A. Inada, H. Amano, I. Akasaki, A. Morita, and K. Kobayashi, “Effect of UV irradiation on the apoptosis and necrosis of Jurkat cells using UV LEDs,” 2009, p. 72310J.

[13] D. H. Choi and Y. K. Cha, “Photo-alignment of low-molecular mass nematic liquid crystals on photoreactive polyimide and polymethacrylate film by irradiation of a linearly polarized UV light,” *Polym. Bull.*, vol. 48, no. 4–5, pp. 373–380, Jun. 2002.

[14] H. Hertz, “Ueber Strahlen electrischer Kraft,” *Ann. Phys.*, vol. 272, no. 4, p. 769–783, Dec. 1889.

[15] D. Y. Kim, S. K. TripathyLian Li and J. Kumar, “Laser-induced holographic surface relief gratings on nonlinear optical polymer films,” *Appl. Phys. Lett.*, vol. 66, no. 10, p. 1166–

1168, Mar. 1995.

[16] 小館香椎子，神谷武志，回折光学素子の数値解析とその応用，丸善出版, 2011.

[17] 大津元一，小林潔，ナノフォトニクスの基礎．オーム社, 2006.

[18] 堀裕和，井上哲也，ナノスケールの光学．オーム社, 2006.

[19] R. C. Enger and S. K. Case, “Optical elements with ultrahigh spatial-frequency surface corrugations,” *Appl. Opt.*, vol. 22, no. 20, p. 3220–3228, Oct. 1983.

[20] Y. Ono, Y. Kimura, Y. Ohta, and N. Nishida, “Antireflection effect in ultrahigh spatial-frequency holographic relief gratings,” *Appl. Opt.* vol. 26, no. 6, p. 1142–1146, Mar. 1987.

[21] T. Weber, T. Käsebier, M. Helgert, E.-B. Kley, and A. Tünnermann, “Tungsten wire grid polarizer for applications in the DUV spectral range,” *Appl. Opt.*, vol. 51, no. 16, p. 3224, Jun. 2012.

[22] T. Weber, T. Käsebier, A. Szeghalmi, M. Knez, E.-B. Kley, and A. Tünnermann, “High aspect ratio deep UV wire grid polarizer fabricated by double patterning,” *Microelectron. Eng.*, vol. 98, pp. 433–435, Oct. 2012.

[23] K. Asano, S. Yokoyama, A. Kemmochi, and T. Yatagai, “Fabrication and characterization of a deep ultraviolet wire grid polarizer with a chromium-oxide subwavelength grating,” *Appl. Opt.*, vol. 53, no. 13, p. 2942, May 2014.

[24] T. Weber, S. Kroker, T. Käsebier, E.-B. Kley, and A. Tünnermann, “Silicon wire grid polarizer for ultraviolet applications,” *Appl. Opt.*, vol. 53, no. 34, p. 8140, Dec. 2014.

[25] G. P. Nordin, J. T. Meier, P. C. Deguzman, and M. W. Jones, “Micropolarizer array for infrared imaging polarimetry,” *J. Opt. Soc. Am. A*, vol. 16, no. 5, p. 1168, May 1999.

[26] L. H. Cescato, E. Gluch, and N. Streibl, “Holographic quarterwave plates,” *Appl. Opt.*, vol. 29, no. 22, p. 3286, Aug. 1990.

[27] Y. Kanamori, H. Kikuta, and K. Hane, “Broadband Antireflection Gratings for Glass Substrates Fabricated by Fast Atom Beam Etching,” *Jpn. J. Appl. Phys.*, vol. 39, no. Part 2, No. 7B, pp. L735–L737, Jul. 2000.

[28] Y. Kanamori, M. Sasaki, and K. Hane, “Broadband antireflection gratings fabricated upon silicon substrates,” *Opt. Lett.*, vol. 24, no. 20, p. 1422, Oct. 1999.

[29] C. J. Chang-Hasnain and W. Yang, “High-contrast gratings for integrated optoelectronics,” *Adv. Opt. Photonics*, vol. 4, no. 3, p. 379, Sep. 2012.

[30] C. F. R. Mateus, M. C. Y. Huang, Y. Deng, A. R. Neureuther, and C. J. Chang-Hasnain, “Ultrabroadband Mirror Using Low-Index Cladded Subwavelength Grating,” *IEEE Photonics Technol. Lett.*, vol. 16, no. 2, pp. 518–520, Feb. 2004.

[31] C. J. Chang-Hasnain, “High-contrast gratings as a new platform for integrated optoelectronics,” *Semicond. Sci. Technol.*, vol. 26, no. 1, p. 14043, Jan. 2011.

[32] Ye Zhou, M. C. Y. Huang, C. Chase, V. Karagodsky, M. Moewe, B. Pesala, F. G. Sedgwick, and C. J. Chang-Hasnain, “High-Index-Contrast Grating (HCG) and Its Applications in Optoelectronic Devices,” *IEEE J. Sel. Top. Quantum Electron.*, vol. 15, no. 5, pp. 1485–1499, 2009.

[33] S. Inoue, J. Kashino, A. Matsutani, H. Ohtsuki, T. Miyashita, and F. Koyama, “Highly angular dependent high-contrast grating mirror and its application for transverse-mode control of VCSELs,” *Jpn. J. Appl. Phys.*, vol. 53, no. 9, p. 90306, Sep. 2014.

[34] Y. Laaroussi, C. Chevallier, F. Genty, N. Fressengeas, L. Cerutti, T. Taliercio, O. Gauthier-Lafaye, P.-F. Calmon, B. Reig, J. Jacquet, and G. Almuneau, “Oxide confinement and high contrast grating mirrors for Mid-infrared VCSELs,” *Opt. Mater. Express*, vol. 3, no. 10, p. 1576, Oct. 2013.

[35] T. T. Wu, Y. C. Syu, S. H. Wu, W. T. Chen, T. C. Lu, S. C. Wang, H. P. Chiang, and D. P. Tsai, “Sub-wavelength GaN-based membrane high contrast grating reflectors,” *Opt. Express*, vol. 20, no. 18, p. 20551, Aug. 2012.

[36] W. Hofmann, C. Chase, M. Müller, Yi Rao, C. Grasse, G. Böhm, M.-C. Amann, and C. J. Chang-Hasnain, “Long-Wavelength High-Contrast Grating Vertical-Cavity Surface-Emitting Laser,” *IEEE Photonics J.*, vol. 2, no. 3, pp. 415–422, Jun. 2010.

[37] C. Chase, Y. Rao, W. Hofmann, and C. J. Chang-Hasnain, “1550 nm high contrast grating VCSEL,” *Opt. Express*, vol. 18, no. 15, p. 15461, Jul. 2010.

[38] M. Gebski, M. Dems, J. Chen, Q. J. Wang, D. H. Zhang, and T. Czyszanowski, “The Influence of Imperfections and Absorption on the Performance of a GaAs/AlOx High-Contrast Grating for Monolithic Integration With 980 nm GaAs-Based VCSELs,” *J. Light. Technol.*, vol. 31, no. 23, pp. 3853–3858, Dec. 2013.

[39] S. M. Rytov, “Electromagnetic Properties of a Finely Stratified Medium,” *Sov. Phys. LETP*, vol. 2, no. 3, pp. 466–475, 1956.

[40] H. Kikuta, H. Toyota, and W. Yu, “Optical Elements with Subwavelength Structured Surfaces,” *Opt. Rev.*, vol. 10, no. 2, pp. 63–73, Mar. 2003.

[41] X. J. Yu and H. S. Kwok, “Optical wire-grid polarizers at oblique angles of incidence,” *J. Appl. Phys.*, vol. 93, no. 8, pp. 4407–4412, Apr. 2003.

[42] L. Zhang, J. H. Teng, S. J. Chua, and E. A. Fitzgerald, “Linearly polarized light emission from InGaN light emitting diode with subwavelength metallic nanograting,” *Appl. Phys. Lett.*, vol. 95, no. 26, p. 261110, Dec. 2009.

[43] P. Lalanne, J. P. Hugonin, and P. Chavel, “Optical properties of deep lamellar Gratings: A coupled Bloch-mode insight,” *J. Light. Technol.*, vol. 24, no. 6, pp. 2442–2449, Jun. 2006.

[44] S. Y. Chou and W. Deng, “Subwavelength amorphous silicon transmission gratings and

applications in polarizers and waveplates," *Appl. Phys. Lett.*, vol. 67, no. 6, pp. 742–744, Aug. 1995.

[45] L. Zhuang, "Fabrication and performance of thin amorphous Si subwavelength transmission grating for controlling vertical cavity surface emitting laser polarization," *J. Vac. Sci. Technol. B Microelectron. Nanom. Struct.*, vol. 14, no. 6, p. 4055, Nov. 1996.

[46] I. C. Botten, M. S. Craig, R. C. McPhedran, J. L. Adams, and J. R. Andrewartha, "The Dielectric Lamellar Diffraction Grating," *Opt. Acta Int. J. Opt.*, vol. 28, no. 3, pp. 413–428, Mar. 1981.

[47] V. Karagodsky, F. G. Sedgwick, and C. J. Chang-Hasnain, "Theoretical analysis of subwavelength high contrast grating reflectors," *Opt. Express*, vol. 18, no. 16, p. 16973, Aug. 2010.

[48] V. Karagodsky, C. Chase, and C. J. Chang-Hasnain, "Matrix Fabry–Perot resonance mechanism in high-contrast gratings," *Opt. Lett.*, vol. 36, no. 9, p. 1704, May 2011.

[49] V. Karagodsky and C. J. Chang-Hasnain, "Physics of near-wavelength high contrast gratings," *Opt. Express*, vol. 20, no. 10, p. 10888, May 2012.

[50] D. T. Pierce and W. E. Spicer, "Electronic Structure of Amorphous Si from Photoemission and Optical Studies," *Phys. Rev. B*, vol. 5, no. 8, pp. 3017–3029, Apr. 1972.

[51] D. E. Aspnes and A. A. Studna, "Dielectric functions and optical parameters of Si, Ge, GaP, GaAs, GaSb, InP, InAs, and InSb from 1.5 to 6.0 eV," *Phys. Rev. B*, vol. 27, no. 2, pp. 985–1009, Jan. 1983.

[52] Y. Zhao, S. Tanaka, C.-C. Pan, K. Fujito, D. Feezell, J. S. Speck, S. P. DenBaars, and S. Nakamura, "High-Power Blue-Violet Semipolar (2021) InGaN/GaN Light-Emitting Diodes with Low Efficiency Droop at 200 A/cm^2," *Appl. Phys. Express*, vol. 4, no. 8, p. 82104, Jul. 2011.

[53] R. Dylewicz, R. A. Hogg, R. Airey, R. Paszkiewicz, P. Bientsman, and S. Patela, "Simulations of nanograting-assisted light coupling in GaN planar waveguide," *Opt. Quantum Electron.*, vol. 42, no. 9–10, pp. 619–629, Sep. 2011.

[54] S. Fujita, "Wide-bandgap semiconductor materials: For their full bloom," *Jpn. J. Appl. Phys.*, vol. 54, no. 3, p. 30101, Mar. 2015.

[55] M. Baeumler, M. Kunzer, R. Schmidt, S. Liu, W. Pletschen, P. Schlotter, K. Köhler, U. Kaufmann, and J. Wagner, "Thermal and non-thermal saturation effects in the output characteristic of UV-to-violet emitting (AlGaIn)N LEDs," *Phys. status solidi*, vol. 204, no. 4, pp. 1018–1024, Apr. 2007.

[56] D. Morita, M. Sano, M. Yamamoto, M. Nonaka, K. Yasutomo, K. Akaishi, S. Nagahama, and T. Mukai, "Over 200 mW on 365 nm ultraviolet light emitting diode of GaN-free

structure," *Phys. status solidi*, vol. 200, no. 1, pp. 114–117, Nov. 2003.

[57] S. You, T. Detchprohm, M. Zhu, W. Hou, E. A. Preble, D. Hanser, T. Paskova, and C. Wetzel, "Highly Polarized Green Light Emitting Diode in m -Axis GaInN/GaN," *Appl. Phys. Express*, vol. 3, no. 10, p. 102103, Oct. 2010.

[58] E. Matioli, S. Brinkley, K. M. Kelchner, Y.-L. Hu, S. Nakamura, S. DenBaars, J. Speck, and C. Weisbuch, "High-brightness polarized light-emitting diodes," *Light Sci. Appl.*, vol. 1, no. 8, p. e22, Aug. 2012.

[59] T. Koyama, T. Onuma, H. Masui, A. Chakraborty, B. A. Haskell, S. Keller, U. K. Mishra, J. S. Speck, S. Nakamura, S. P. DenBaars, T. Sota, and S. F. Chichibu, "Prospective emission efficiency and in-plane light polarization of nonpolar m-plane InxGa1−xN/GaN blue light emitting diodes fabricated on freestanding GaN substrates," *Appl. Phys. Lett.*, vol. 89, no. 9, p. 91906, Aug. 2006.

[60] C.-F. Lai, J.-Y. Chi, H.-H. Yen, H.-C. Kuo, C.-H. Chao, H.-T. Hsueh, J.-F. T. Wang, C.-Y. Huang, and W.-Y. Yeh, "Polarized light emission from photonic crystal light-emitting diodes," *Appl. Phys. Lett.*, vol. 92, no. 24, p. 243118, Jun. 2008.

[61] M. Ma, D. S. Meyaard, Q. Shan, J. Cho, E. F. Schubert, G. B. Kim, M.-H. Kim, and C. Sone, "Polarized light emission from GaInN light-emitting diodes embedded with subwavelength aluminum wire-grid polarizers," *Appl. Phys. Lett.*, vol. 101, no. 6, p. 61103, Aug. 2012.

[62] M. Wang, B. Cao, C. Wang, F. Xu, Y. Lou, J. Wang, and K. Xu, "High linearly polarized light emission from InGaN light-emitting diode with multilayer dielectric/metal wire-grid structure," *Appl. Phys. Lett.*, vol. 105, no. 15, p. 151113, Oct. 2014.

[63] T. Kolbe, A. Knauer, C. Chua, Z. Yang, V. Kueller, S. Einfeldt, P. Vogt, N. M. Johnson, M. Weyers, and M. Kneissl, "Effect of temperature and strain on the optical polarization of (In)(Al)GaN ultraviolet light emitting diodes," *Appl. Phys. Lett.*, vol. 99, no. 26, p. 261105, Dec. 2011.

[64] M. V. Durnev and S. Y. Karpov, "Polarization phenomena in light emission from C -plane Al(In)GaN heterostructures," *Phys. status solidi*, vol. 250, no. 1, pp. 180–186, Jan. 2013.

[65] L. Schade, U. T. Schwarz, T. Wernicke, J. Rass, S. Ploch, M. Weyers, and M. Kneissl, "On the optical polarization properties of semipolar InGaN quantum wells," *Appl. Phys. Lett.*, vol. 99, no. 5, p. 51103, Aug. 2011.

[66] K. H. Li, Q. Wang, H. P. T. Nguyen, S. Zhao, and Z. Mi, "Polarization-resolved electroluminescence study of InGaN/GaN dot-in-a-wire light-emitting diodes grown by molecular beam epitaxy," *Phys. status solidi*, vol. 212, no. 5, pp. 941–946, May 2015.

[67] K. M. Mayer and J. H. Hafner, "Localized Surface Plasmon Resonance Sensors," *Chem. Rev.*, vol. 111, no. 6, pp. 3828–3857, Jun. 2011.

[68] C. F. R. Mateus, M. C. Y. Huang, P. Li, B. T. Cunningham, and C. J. Chang-Hasnain, “Compact Label-Free Biosensor Using VCSEL-Based Measurement System,” *IEEE Photonics Technol. Lett.*, vol. 16, no. 7, pp. 1712–1714, Jul. 2004.

[69] G. Li, Y. Shen, G. Xiao, and C. Jin, “Double-layered metal grating for high-performance refractive index sensing,” *Opt. Express*, vol. 23, no. 7, p. 8995, Apr. 2015.

[70] A. A. Rifat, G. A. Mahdiraji, Y. M. Sua, R. Ahmed, Y. G. Shee, and F. R. M. Adikan, “Highly sensitive multi-core flat fiber surface plasmon resonance refractive index sensor,” *Opt. Express*, vol. 24, no. 3, p. 2485, Feb. 2016.

[71] E. M. Larsson, J. Alegret, M. Käll, and D. S. Sutherland, “Sensing Characteristics of NIR Localized Surface Plasmon Resonances in Gold Nanorings for Application as Ultrasensitive Biosensors,” *Nano Lett.*, vol. 7, no. 5, pp. 1256–1263, May 2007.

[72] M. R. Saleem, R. Ali, S. Honkanen, and J. Turunen, “Bio-molecular sensors based on guided mode resonance filters,” *IOP Conf. Ser. Mater. Sci. Eng.*, vol. 146, p. 12030, Aug. 2016.

[73] P. K. Sahoo, J. Joseph, R. Yukino, and A. Sandhu, “High sensitivity refractive index sensor based on simple diffraction from phase grating,” *Opt. Lett.*, vol. 41, no. 9, p. 2101, May 2016.

[74] D. V. Nesterenko, S. Hayashi, and Z. Sekkat, “Evanescent-field-coupled guided-mode sensor based on a waveguide grating,” *Appl. Opt.*, vol. 54, no. 15, p. 4889, May 2015.

[75] Y. Liu and H. W. M. Salemink, “Photonic crystal-based all-optical on-chip sensor,” *Opt. Express*, vol. 20, no. 18, p. 19912, Aug. 2012.

[76] X.-J. Tan and X.-S. Zhu, “Optical fiber sensor based on Bloch surface wave in photonic crystals,” *Opt. Express*, vol. 24, no. 14, p. 16016, Jul. 2016.

[77] T. Sun, S. Kan, G. Marriott, and C. Chang-Hasnain, “High-contrast grating resonators for label-free detection of disease biomarkers,” *Sci. Rep.*, vol. 6, p. 27482, Jun. 2016.

[78] 小塚洋司, 電気磁気学 その物理像と詳論. 森北出版, 2012.

[79] 江馬一弘, 光物理学の基礎. 朝倉書店, 2010.

[80] 岡本隆之, 梶川浩太郎, プラズモニクス－基礎と応用. 講談社, 2010.

[81] L. Mashev and E. Popov, “Zero order anomaly of dielectric coated gratings,” *Opt. Commun.*, vol. 55, no. 6, pp. 377–380, Oct. 1985.

[82] 河田聡, ナノオプティクス・ナノフォトニクスのすべて. フロンティア出版, 2006.

[83] P. Vincent and M. Nevière, “Corrugated dielectric waveguides: A numerical study of the second-order stop bands,” *Appl. Phys.*, vol. 20, no. 4, pp. 345–351, Dec. 1979.

[84] Y. Ding and R. Magnusson, “Band gaps and leaky-wave effects in resonant photonic-crystal waveguides,” *Opt. Express*, vol. 15, no. 2, p. 680, Jan. 2007.

[85] R. Magnusson and M. Shokooh-Saremi, “Physical basis for wideband resonant

reflectors," *Opt. Express*, vol. 16, no. 5, p. 3456, 2008.

[86] Z. S. Liu, S. Tibuleac, D. Shin, P. P. Young, and R. Magnusson, "High-efficiency guided-mode resonance filter," *Opt. Lett.*, vol. 23, no. 19, p. 1556, Oct. 1998.

[87] Y.-T. Yoon, C.-H. Park, and S.-S. Lee, "Highly Efficient Color Filter Incorporating a Thin Metal–Dielectric Resonant Structure," *Appl. Phys. Express*, vol. 5, no. 2, p. 22501, Feb. 2012.

[88] K. J. Lee, J. Giese, L. Ajayi, R. Magnusson, and E. Johnson, "Resonant grating polarizers made with silicon nitride, titanium dioxide, and silicon: Design, fabrication, and characterization," *Opt. Express*, vol. 22, no. 8, p. 9271, Apr. 2014.

[89] S. He, Z. Shi, X. Li, X. Gao, Z. Wang, Q. Liu, G. Zhu, M. Zhang, H. Zhu, and Y. Wang, "Membrane guided-mode resonant color filters exhibiting adjustable spectral response," *Opt. Commun.*, vol. 342, pp. 129–135, May 2015.

[90] K. Yamada, K. Asai, Y. H. Ko, K. Kintaka, K. J. Lee, J. Inoue, S. Ura, and R. Magnusson, "High reflectance with steep reflection phase spectrum by guided-mode resonance," *Appl. Phys. Express*, vol. 9, no. 12, p. 122501, Dec. 2016.

[91] 迫田和彰，フォトニック結晶入門．森北出版, 2004.

[92] E. L. Lomon, "Classical Electrodynamics. John David Jackson. Wiley, New York, 1962. *Science (80-.).*, vol. 136, no. 3521, pp. 1046–1047, Jun. 1962.

[93] M. Xu, H. P. Urbach, D. K. G. de Boer, and H. J. Cornelissen, "Wire-grid diffraction gratings used as polarizing beam splitter for visible light and applied in liquid crystal on silicon," *Opt. Express*, vol. 13, no. 7, p. 2303, 2005.

[94] M. G. Moharam and T. K. Gaylord, "Rigorous coupled-wave analysis of planar-grating diffraction," *J. Opt. Soc. Am.*, vol. 71, no. 7, p. 811, Jul. 1981.

[95] M. G. Moharam and T. K. Gaylord, "Diffraction analysis of dielectric surface-relief gratings," *J. Opt. Soc. Am.*, vol. 72, no. 10, p. 1385, Oct. 1982.

[96] M. G. Moharam and T. K. Gaylord, "Rigorous coupled-wave analysis of grating diffraction— E-mode polarization and losses," *J. Opt. Soc. Am.*, vol. 73, no. 4, p. 451, Apr. 1983.

[97] M. G. Moharam and T. K. Gaylord, "Rigorous coupled-wave analysis of metallic surface-relief gratings," *J. Opt. Soc. Am. A*, vol. 3, no. 11, p. 1780, Nov. 1986.

[98] 日本光学会光設計研究グループ，光学技術者のための電磁場解析入門．オプトロニクス社, 2010.

[99] 橋本修，実践 FDTD時間領域差分法．森北出版, 2006.

[100] J.-P. Berenger, "A perfectly matched layer for the absorption of electromagnetic waves," *J. Comput. Phys.*, vol. 114, no. 2, pp. 185–200, Oct. 1994.

[101] G. G. Kang, I. Vartiainen, B. F. Bai, H. Tuovinen, and J. Turunen, "Inverse polarizing

effect of subwavelength metallic gratings in deep ultraviolet band," *Appl. Phys. Lett.*, vol. 99, no. 7, p. 71103, Aug. 2011.

[102] A. D. Rakić, A. B. Djurišić, J. M. Elazar, and M. L. Majewski, "Optical properties of metallic films for vertical-cavity optoelectronic devices," *Appl. Opt.*, vol. 37, no. 22, p. 5271, Aug. 1998.

[103] P. Johnson and R. Christy, "Optical constants of transition metals: Ti, V, Cr, Mn, Fe, Co, Ni, and Pd," *Phys. Rev. B*, vol. 9, no. 12, pp. 5056–5070, Jun. 1974.

[104] D. Brunner, H. Angerer, E. Bustarret, F. Freudenberg, R. Höpler, R. Dimitrov, O. Ambacher, and M. Stutzmann, "Optical constants of epitaxial AlGaN films and their temperature dependence," *J. Appl. Phys.*, vol. 82, no. 10, pp. 5090–5096, Nov. 1997.

[105] T. Iwanaga, T. Suzuki, S. Yagi, and T. Motooka, "Optical absorption properties of Mg-doped GaN nanocolumns," *J. Appl. Phys.*, vol. 98, no. 10, p. 104303, Nov. 2005.

[106] L. Gao, F. Lemarchand, and M. Lequime, "Exploitation of multiple incidences spectrometric measurements for thin film reverse engineering," *Opt. Express*, vol. 20, no. 14, p. 15734, Jul. 2012.

[107] L. B. Mashev, E. Popov, and E. G. Loewen, "Brewster effects for deep metallic gratings," *Appl. Opt.*, vol. 28, no. 13, p. 2538, Jul. 1989.

[108] S. Heikman, S. Keller, S. P. DenBaars, U. K. Mishra, F. Bertram, and J. Christen, "Non-planar Selective Area Growth and Characterization of GaN and AlGaN," *Jpn. J. Appl. Phys.*, vol. 42, no. Part 1, No. 10, pp. 6276–6283, Oct. 2003.

[109] M. Jerman, Z. Qiao, and D. Mergel, "Refractive index of thin films of SiO2, ZrO2, and HfO2 as a function of the films' mass density," *Appl. Opt.*, vol. 44, no. 15, p. 3006, May 2005.

[110] K. Luke, Y. Okawachi, M. R. E. Lamont, A. L. Gaeta, and M. Lipson, "Broadband mid-infrared frequency comb generation in a Si3N4 microresonator," *Opt. Lett.*, vol. 40, no. 21, p. 4823, Nov. 2015.

[111] G. M. Hale and M. R. Querry, "Optical Constants of Water in the 200-nm to 200-μm Wavelength Region," *Appl. Opt.*, vol. 12, no. 3, p. 555, Mar. 1973.

[112] E. Sani and A. Dell'Oro, "Spectral optical constants of ethanol and isopropanol from ultraviolet to far infrared," *Opt. Mater. (Amst).*, vol. 60, pp. 137–141, Oct. 2016.